VERLAG DER TECHNISCHEN UNIVERSITÄT GRAZ

Silvio Prskalo

Coupled thermo-hygral and mechanical behavior in fresh concrete: a multiphase material model approach

CES 49

MONOGRAPHIC SERIES TU GRAZ
COMPUTATION IN ENGINEERING AND SCIENCE

Silvio Prskalo

Coupled thermo-hygral and mechanical behavior in fresh concrete: a multiphase material model approach

Monographic Series TU Graz
Computation in Engineering and Science

Series Editors

Monographic Series TU Graz
Computation in Engineering and Science Volume 49

Silvio Prskalo

Coupled thermo-hygral and mechanical behavior in fresh concrete: a multiphase material model approach

This work is based on the dissertation “Coupled thermo-hygral and mechanical behavior in fresh concrete: a multiphase material model approach“, presented at Graz University of Technology, Institute of Applied Mechanics in 2025.

Supervision / Assessment:

Martin Schanz (Graz University of Technology)
Vít Šmilauer (Czech Technical University in Prague)

Cover	Verlag der Technischen Universität Graz
Cover photo	Vier-Spezies-Rechenmaschine
	by courtesy of the Gottfried Wilhelm Leibniz Bibliothek
	Niedersächsische Landesbibliothek Hannover
Printed by	Buchschmiede (DATAFORM Media GmbH)

2026 Verlag der Technischen Universität Graz

www.tugraz-verlag.at

Print
ISBN 978-3-99161-067-0

E-Book
ISBN 978-3-99161-068-7
DOI 10.3217/978-3-99161-067-0

Abstract

The early-age behavior of concrete is strongly governed by the interaction between moisture transport and the evolution of mechanical properties. This thesis introduces a novel multiphase continuum-mechanical model that accounts for the coupled progression of temperature, moisture and mechanical behavior during hydration. A central innovation of the model is the incorporation of an evaporation exchange formulation directly into the mass balances, enabling explicit coupling between evaporation and hydration, an interaction often neglected in traditional porous media formulations. Calibration of the evaporation process is performed using Dynamic Vapor Sorption (DVS) experiments. Another key contribution is the critical assessment of the commonly assumed linear relationship between porosity and the degree of hydration. While a linear trend is observed for the studied concrete mixes and conditions, this assumption may not hold across all material compositions or environmental settings. The proposed model overcomes this limitation by allowing for nonlinear dependencies, thus capturing more complex interactions shaped by varying microstructural and boundary influences. Based on the triphasic framework of Gawin et al. (2006), the model is extended with a multiscale formulation that links hydration degree to time-dependent changes in stiffness and strength. This leads to a predictive tool capable of realistically simulating the complex coupled processes that characterize the early-age behavior of concrete.

The implementation is realized in a fully coupled finite element environment, accounting for the nonlinear interactions between heat conduction, moisture transport (including evaporation) and mechanical response. To verify its accuracy and practical applicability, the model undergoes a two-step numerical validation: (i) simulation of coupled moisture and temperature evolution and (ii) prediction of strength and stiffness development. Validated across different concrete mixes and boundary conditions, the model demonstrates broad applicability. Simulation results align closely with experimental data, confirming its reliability and efficiency for predicting early-age concrete behavior under varied curing conditions.

Zusammenfassung

Das Verhalten von Frischbeton wird durch den Feuchtetransport und die Entwicklung mechanischer Eigenschaften beeinflusst. In dieser Dissertation wird ein mehrphasiges kontinuumsmechanisches Modell zur Simulation des Betonalerhärtungssverhaltens im frühen Stadium vorgestellt, das insbesondere die gekoppelte Entwicklung von Temperatur, Feuchte und mechanischen Kennwerten berücksichtigt. Eine zentrale Neuerung ist die explizite Berücksichtigung des Evaporationsaustauschs in den Massenbilanzgleichungen, wodurch eine direkte Kopplung zwischen Evaporation und Hydratation ermöglicht wird. Dieser Aspekt wird in den meisten porenmechanischen Modellen vernachlässigt. Die Kalibrierung des Evaporationsprozesses erfolgt auf Basis von Dynamic Vapor Sorption (DVS) Experimenten. Ein weiterer wesentlicher Beitrag ist die kritische Untersuchung der häufigen Annahme einer linearen Beziehung zwischen Porosität und Hydratationsgrad. Obwohl für die untersuchten Betonzusammensetzungen und Randbedingungen diese Tendenz beobachtet wird, ist diese Annahme nicht uneingeschränkt auf alle Materialzusammensetzungen oder Umgebungsbedingungen übertragbar. Das vorgeschlagene Modell überwindet diese Einschränkung, indem es nichtlineare Abhängigkeiten zulässt und damit komplexe Wechselwirkungen infolge variierender Mikrostruktur und Randbedingungen abbilden kann. Aufbauend auf der Arbeit von Gawin et al. (2006) wird das Modell um eine multiskalige Formulierung erweitert, welche den Hydratationsgrad mit der zeitabhängigen Entwicklung von Steifigkeit und Festigkeit verknüpft. Das resultierende Modell ist in der Lage, die komplexen gekoppelten Prozesse des Verhaltens von Beton im frühen Stadium realitätsnah zu simulieren.

Die Implementierung erfolgt in einer vollständig gekoppelten Finite-Elemente-Umgebung, welche die nichtlinearen Wechselwirkungen zwischen Wärmeleitung, Feuchtetransport (einschließlich Evaporation) und mechanischem Verhalten berücksichtigt. Zur Beurteilung der Genauigkeit und praktischen Anwendbarkeit wird das Modell in zwei Schritten numerisch validiert: (i) Simulation der gekoppelten Feuchte- und Temperaturentwicklung und (ii) Prognose der Festigkeits- und Steifigkeitsentwicklung. Die Validierung für verschiedene Betonzusammensetzungen und Randbedingungen zeigt eine breite Anwendbarkeit des Modells. Die Simulationsergebnisse stimmen sehr gut mit experimentellen Daten überein und bestätigen die Zuverlässigkeit und Effizienz des Modells zur Prognose des Frühverhaltens von Beton unter unterschiedlichen Erhärtungsbedingungen.

Acknowledgements

With this dissertation, I am bringing to a close an amazing six years at the Applied Mechanics Institute and a total of thirteen years of studying at Graz University of Technology. First and foremost, I would like to express my sincere gratitude to my mentor, Prof. Martin Schanz, for the valuable opportunity to learn and develop under his guidance. His steady support, composed demeanor and insightful advice were instrumental in helping me navigate the challenges throughout my dissertation research.

I would also like to thank all my colleagues at the institute for their friendship and collaboration. Special thanks to my office mates, Andreas Grendas and Thomas Kramer, for the countless good times we shared, both during work and through problem-solving sessions. A heartfelt thank you to Evelyn Feyertag for always bringing warmth and positivity to the institute with her caring nature. I am particularly grateful to Ishan Gupta, who has been by my side from start to finish, as we both embarked on our dissertation journeys. The many discussions, debates and shared moments have been essential in shaping my work.

A sincere thank you to Dr. Joachim Juhart for allowing me to conduct my experiments at the Institute of Technology and Testing of Building Materials. I am also deeply grateful to my colleagues, Ognjen Rudic, for his help in setting up the experiments, and Michael Autischer, who was always available to answer my many questions and assist me during the experimental phase. A special mention to Prof. Dirk Schlicke, who already supported me during my master's thesis and continued to offer his expertise and help throughout my dissertation journey.

I must also extend my gratitude to all my friends and roommates who have been there for me through both the good times and, fortunately, the rare bad moments. Our shared adventures, travels, and the memories we've created, we will look back on with laughter for many years to come.

Above all, I am deeply grateful to my family for their unwavering support. Thank you, Mum, Dad, my brother, and my sister, for always being by my side. I would also like to sincerely thank Austria for giving me the opportunity to pursue my education here, and Graz for becoming the place where this journey could unfold.

CONTENTS

NOMENCLATURE

In this monograph, the notation adheres to the conventions typically employed in modern continuum mechanics, as referenced in Ehlers [43] and Bonet & Wood [15]. Furthermore, the symbols used align with the standard nomenclature provided by Ehlers [47] and De Boer [35].

General conventions

$(\cdot)$	placeholder for arbitrary physical quantities
a, b or ϕ, ψ	scalars (0-th order tensors)
$\mathbf{a}, \mathbf{b}$ or $\boldsymbol{\phi}, \boldsymbol{\psi}$	vectors (1-st order tensors)
$\mathbf{A}, \mathbf{B}$ or $\boldsymbol{\Phi}, \boldsymbol{\Psi}$	2-nd order tensors

Index and suffix conventions

$(\cdot)_0$	quantity at initial time ($t = 0$)
$\tilde{(\cdot)}$	quantity in intermediate configuration (from polar decomposition)
$(\cdot)^\alpha$	superscripts indicate non-kinematic quantities of a constituent within porous media
$(\cdot)_\alpha$	subscripts indicate kinematic quantities of a constituent within porous media
$(\cdot)_0^\alpha$	initial values of non-kinematic quantities with respect to the reference configuration of a constituent ($t = 0$)
$\dot{(\cdot)} = \mathrm{d}(\cdot)/\mathrm{d}t$	total time derivative with respect to the aggregate φ
$(\cdot)'_\alpha = \mathrm{d}_\alpha(\cdot)/\mathrm{d}t$	material time derivative following the motion of φ^α
$\mathbf{a} \cdot \mathbf{b} = a_i b_i = c$	single contraction of vectors $\mathbf{a}$ and $\mathbf{b}$
$\mathbf{A} : \mathbf{B} = A_{ij} B_{ij} = c$	double contraction of 2-nd order tensors $\mathbf{A}$ and $\mathbf{B}$
$\mathbf{A}\mathbf{b} = A_{ij} b_j = c_i = \mathbf{c}$	matrix-vector multiplication of 2-nd order tensor $\mathbf{A}$ and vector $\mathbf{b}$
$\mathbf{A}\mathbf{B} = A_{ij} B_{jk} = C_{ik} = \mathbf{C}$	matrix-matrix multiplication of 2-nd order tensors $\mathbf{A}$ and $\mathbf{B}$
$\mathbf{a} \otimes \mathbf{b} = a_i b_j = C_{ij} = \mathbf{C}$	tensor product of vectors $\mathbf{a}$ and $\mathbf{b}$

Symbol	Unit	Description
α		identifier for constituents, specifically $\alpha = \{S, L, G\}$
$\beta_1, \beta_2, \beta_3, \beta_4$		parameters related to materials
$\mathbf{b}$	$[\mathrm{m/s^2}]$	vector of mass-specific volume force, first order
$\mathbf{B}_S$		left Cauchy-Green deformation tensor for solids
$\mathcal{B}, \mathcal{B}^\alpha$		aggregate body and the body of constituent α
$\mathcal{C}$	$[\mathrm{kg/m^3 s}]$	maximum rate of mass exchange
$\mathbf{C}_S$		right Cauchy-Green deformation tensor for solids
$\mathrm{d}a$	$[\mathrm{m^2}]$	area differential of φ in the current configuration
$\mathrm{d}A$	$[\mathrm{m^2}]$	area differential of φ in the reference configuration
$\mathbf{D}_S$	$[1/\mathrm{s}]$	symmetric component of the velocity gradient for solids
$\mathrm{d}v$	$[\mathrm{m^3}]$	bulk volume differential of φ in the current configuration
$\mathrm{d}V$	$[\mathrm{m^3}]$	volume differential of φ in the reference configuration
$\mathrm{d}\mathbf{x}$	$[\mathrm{m}]$	line differential of φ in the current configuration
$\mathrm{d}\mathbf{X}$	$[\mathrm{m}]$	line differential of φ in the reference configuration
$\varepsilon, \varepsilon^\alpha$	$[\mathrm{J/kg}]$	internal energy per unit mass for φ and φ^α
$\hat{\varepsilon}^\alpha$	$[\mathrm{J/m^3 s}]$	direct energy production per unit volume for φ^α
$\hat{e}^\alpha$	$[\mathrm{J/m^3 s}]$	total energy production per unit volume for φ^α
$\mathbf{A}_S$		Euler-Almansi strain tensor for solids
$\mathbf{E}_S$		Green-Lagrange strain tensor for solids
φ, φ^α		complete aggregate and the constituent α
$\mathbf{F}$		deformation gradient of the material for φ
η, η^α	$[\mathrm{J/Kkg}]$	mass-specific entropy for φ and φ^α
$\hat{\eta}, \hat{\eta}^\alpha$	$[\mathrm{J/Km^3 s}]$	total entropy production per unit volume for φ and φ^α
Θ	$[\mathrm{K}]$	temperature associated with the aggregate φ
I_S, II_S, III_S		principal invariants corresponding to $\mathbf{C}_S$
J		Jacobian determinant linked to φ
$\mathbf{J}_n$		Jacobian tangent matrix evaluated at time t_n
$k^{r\alpha}$		relative permeability of specific phase α
K^S	$[\mathrm{m^2}]$	intrinsic permeability of solid
λ^S	$[\mathrm{N/m^2}]$	Lamé's constant
$\mathbf{L}_S$	$[1/\mathrm{s}]$	spatial gradient of velocity for solids
μ^S	$[\mathrm{N/m^2}]$	Lamé constant

Symbol	Unit	Description
m^α	[kg]	mass associated with the constituent φ^α
n^α		volume fraction associated with φ^α
N_e		total count of elements in the system
N_n		number of nodes per element
N_N		overall total of nodes present
$\hat{\mathbf{N}}_S^i$		eigenvectors of $\mathbf{C}_S$ in the reference state
$\mathbf{n}$		outward-facing unit normal vector on the surface
χ_α		function representing motion of φ^α
$\mathbf{P}$	$[\mathrm{N/m^2}]$	first Piola-Kirchhoff stress tensor for φ
$\hat{\mathbf{p}}^\alpha, \hat{\mathbf{p}}_E^\alpha$	$[\mathrm{N/m^3}]$	volume-specific momentum production (extra- $(\cdot)_E$) for φ^α
$\mathbf{q}, \mathbf{q}^\alpha$	$[\mathrm{J/m^2 s}]$	heat flux vector for φ and φ^α
ρ	$[\mathrm{kg/m^3}]$	density of the overall aggregate φ
$\rho^\alpha, \rho^{\alpha R}$	$[\mathrm{kg/m^3}]$	partial and reference density for φ^α
$\hat{\rho}^\alpha$	$[\mathrm{kg/m^3 s}]$	mass production per unit volume for φ^α
r, r^α	$[\mathrm{J/kgs}]$	mass-specific external heat input
$\sigma_\eta, \sigma_\eta^\alpha$		external entropy supply per unit volume for φ and φ^α
σ, σ^α		scalar quantities representing supply terms for mechanical inputs
$\mathbf{S}$	$[\mathrm{N/m^2}]$	second Piola-Kirchhoff stress tensor for φ
t	[s]	time variable
$\mathbf{t}$	$[\mathrm{N/m^2}]$	surface traction vector associated with φ
$\mathbf{T}, \mathbf{T}^\alpha, \mathbf{T}_E^\alpha$	$[\mathrm{N/m^2}]$	Cauchy stress tensors in current configuration, (including extra- $(\cdot)_E$) for φ and φ^α
$\mathbf{u}_S$	[m]	solid displacement vector
$\mathbf{U}_S$		right stretch tensor for solids
V, V^α	$[\mathrm{m^3}]$	total volume of $\mathcal{B}$ and partial volume associated with $\mathcal{B}^\alpha$
$\mathbf{V}_S$		left stretch tensor corresponding to solids
$\mathbf{w}_{FS}$	$[\mathrm{m/s}]$	seepage velocity vector
$\phi_\eta, \phi_\eta^\alpha$	$[\mathrm{J/Km^2 s}]$	entropy outflux vector for φ and φ^α
$\mathbf{x}$	[m]	position vector in the current state
$\mathbf{x}'_\alpha = \mathbf{v}_\alpha$	$[\mathrm{m/s}]$	velocity vector for φ^α
$\mathbf{x}''_\alpha$	$[\mathrm{m/s^2}]$	acceleration vector for φ^α
$\mathbf{x}'$	$[\mathrm{m/s}]$	velocity of the overall aggregate φ

Symbol	Unit	Description
$\mathbf{x}''$	$[\mathrm{m/s^2}]$	acceleration of the overall aggregate φ
$\mathbf{X}$	$[\mathrm{m}]$	reference position vector for φ
ψ^α	$[\mathrm{J/kg}]$	mass-specific Helmholtz free energy associated with φ^α
$\overline{\Psi}^\alpha$		chemical potential for φ^α
$\hat{\zeta}^\alpha$	$[\mathrm{J/Km^3s}]$	volume-specific direct production of entropy for φ^α

1 INTRODUCTION AND OVERVIEW

Concrete is far more than just a building material, it is a cornerstone of modern infrastructur. From high-rise buildings to transport networks, concrete forms the structural backbone of our cities and communities. Its strength, durability, and adaptability make it indispensable across a wide range of construction applications, from housing to complex engineering projects.

Thanks to advances in material science, concrete can now be tailored to meet specific performance demands, helping structures withstand growing urban pressures, environmental impacts, and the effects of climate change. Its ability to support ambitious architectural designs, while maintaining long-term resilience, makes it central to modern construction.

As urban populations grow and sustainability becomes increasingly critical, concrete's role continues to evolve. With the potential for recycling and the integration of industrial by-products, it offers promising opportunities for more sustainable construction. Understanding the behavior of concrete during both its early and later stages of hardening plays a crucial role in ensuring structural safety, durability, and performance throughout the entire service life of a structure. Through research and innovation, we can further optimize its properties, reduce its environmental impact, and support the development of smarter, more resilient infrastructure. A deeper understanding of concrete is not only essential for engineering progress, but it is also vital for shaping the future of sustainable urban development.

1.1 Motivation

To maximize the potential of concrete and address the evolving challenges in construction, it is crucial to thoroughly model its properties and behaviors. This process entails developing mathematical and computational frameworks that accurately capture the characteristics of concrete, ranging from its initial mixing state to its fully cured, hardened form. Effective modeling deepens our understanding of the intricate interactions within the concrete matrix, enabling us to make predictive evaluations of its performance across diverse loading conditions and environmental factors.

The significant role of concrete in construction is extensively documented in existing literature, including notable studies by Mehta and Monteiro [103] and Kosmatka et al. [89]. However, as we strive to innovate and enhance the performance of concrete, the necessity for rigorous modeling and research has become increasingly critical. Gaining a deeper insight into the fundamental properties and behaviors of concrete allows us to more accurately predict its performance across various applications, ultimately contributing to the

Figure 1.1: Visual representation of chaotic urban landscapes illustrating the consequences of unplanned construction and urban sprawl.

development of safer and more sustainable structures. Figure 1.1 offers a visual portrayal of chaotic urban development, underscoring the adverse effects of unplanned construction. In contrast, Figure 1.2 presents an illustration of contemporary urban landscapes that showcase the integration of deliberate, well-planned construction within modern concrete environments. Together, these images highlight the critical role of strategic planning in the built environment.

Furthermore, advanced modeling techniques enable researchers to simulate the behavior of concrete in a wide array of scenarios, assisting engineers in refining mix designs and structural configurations prior to implementation. These models act as essential tools that reduce risks and improve the reliability of concrete structures. Investigating concrete as a material yields critical insights into its composition, durability, and structural integrity. These insights are particularly vital during the initial stages of concrete hardening, where numerical experimental studies are essential for comprehending the material's behavior as it hardens. During this pivotal phase, analyzing the properties of fresh concrete allows researchers to simulate various scenarios and environmental conditions, facilitating the identification of potential vulnerabilities and the optimization of concrete mixtures prior to their implementation in real-world applications.

Such investigations in the early stages are crucial for not only enhancing the material's longevity and resilience but also for ensuring that structures can endure the challenges posed by moisture, chemical exposure, and temperature fluctuations over time. By gaining a deeper understanding of how concrete behaves during its early hardening phase, engineers are equipped to make informed decisions that significantly influence the overall performance and safety of the completed structure. Furthermore, the durability of concrete

Figure 1.2: Illustration of contemporary urban landscapes highlighting the integration of planned construction within modern concrete environments.

structures is extensively documented, with notable contributions from research by Mays [102] and Dhir and Dyer [37]. Concrete's durability is especially critical in an era increasingly centered on sustainability and resource efficiency. Long-lasting concrete structures not only reduce lifecycle costs but also minimize environmental impacts, aligning with contemporary priorities for sustainable construction. This is supported by responsible practices such as curing techniques on site, as illustrated in Figure 1.3. Accurate modeling of concrete enables engineers to forecast how concrete will behave under different loads and conditions, facilitating the creation of efficient and resilient structures. By leveraging advancements in material science, we can improve the properties of concrete and develop specialized formulations tailored to meet specific requirements, thus broadening its applications in construction.

In conclusion, the significance of concrete extends far beyond its role as a basic building material. As we enhance our understanding of concrete through ongoing research and numerical experimental studies, we unlock new possibilities for innovative applications and solutions that address the evolving challenges of modern construction. Emphasizing the importance of modeling and experimentation during the early stages of concrete development is crucial for maximizing its potential for future generations.

1.2 Objectives and state of the art

Predicting the behavior of concrete is a vital goal that has attracted considerable research interest over the years. Numerical models of concrete are crucial for forecasting its mechanical behavior under a variety of loading and environmental conditions. These models vary in complexity, from one-phase representations to more sophisticated two-phase or multi-phase models, each providing unique insights into the nuances of concrete behavior.

Figure 1.3: Early-age concrete behavior in the first 24 hours and typical curing techniques used on construction sites.

Among the simplest are one-phase models, such as elastic models by Eringen [53], which operate under the assumption of linear behavior for small deformations, as articulated by Hooke's law. Although these models are relatively straightforward and computationally efficient, they frequently oversimplify the true behavior of concrete. In particular, elastic models do not adequately account for non-linear phenomena, including cracking and irreversible deformations.

To overcome these limitations, researchers have developed plasticity models that integrate yield criteria to predict plastic deformation and simulate non-linear behavior, including cracking. Notable references for these models include foundational works of Bazant and Oh [7], Bazant and Prat [11], Malvar et al. [99] and Shah et al. [131]. These models offer a more accurate depiction of concrete's response under stress by accounting for the material's ability to undergo permanent deformation once it surpasses its yield point. In recent years, damage mechanics models have gained prominence, especially those that incorporate damage parameters from fracture mechanics, due to their effectiveness in accurately representing the behavior of concrete during the later stages of hydration. These models emphasize the progressive deterioration of material properties caused by microcracking, which can eventually lead to fractures. Significant advancements in concrete modeling have been realized through the plastic-damage framework proposed by Lubliner et al. [97], as well as the damage-plasticity model developed by Grassl and Jirásek [70]. These approaches incorporate damage variables that evolve with the material's loading history, enabling accurate representation of progressive deterioration and potential failure mechanisms.

Transitioning to two-phase models, these approaches view concrete as a composite material composed of both a matrix and aggregates, facilitating a more effective depiction of

fracture and damage behavior, as demonstrated in the work of Hillerborg et al. [80]. These models effectively balance accuracy with computational efficiency. However, they may require detailed material characterization to achieve reliable predictions. In parallel, lattice models conceptualize concrete as a network of discrete elements, allowing for a nuanced understanding of the complex interactions that occur among these elements. Although lattice models, such as those presented by Bazant and Planàs [10], are highly adaptable and capable of representing intricate behaviors, they require substantial computational resources for successful implementation.

Furthermore, the characterization of concrete as a porous material introduces an added level of complexity to its modeling. This portrayal, as examined in research such as [2] and [47], involves materials with internal structures comprising solid phases and interconnected pores. These pores can contain various fluid phases, which play a significant role in determining the unique properties of concrete. Key characteristics of porous materials, highlighted in Ehlers [44], include permeability, which dictates fluid flow within the material, and porosity, representing the fraction of void volume. These properties significantly affect concrete's behavior, especially under external stimuli. Multiscale models integrate different length scales, allowing predictions of concrete behavior from the microstructural to structural levels. While offering valuable insights, these models require significant computational resources and detailed input data. They also account for interactions among all phases within the porous material and consider environmental effects, though their implementation can be complex. Foundational works by Alexander and Mindess [3] and Coussy [26] provide extensive insights into the numerical modeling of concrete.

Research on the behavior of concrete under elevated temperatures, such as those encountered during fire exposure, has led to the development of advanced multiphase-coupled models [66, 110, 112]. These models have shown strong consistency with experimental findings in works of Davie et al. [34], Fey et al. [56] and Dauti et al. [33]. However, they are predominantly designed for mature, fully hardened concrete and typically rely on simplified assumptions, such as uniform initial conditions that overlook the complex characteristics present at early ages. In fire scenarios, dehydration emerges as a critical process at temperatures above 105°C, where it substantially affects both the thermal conductivity and mechanical integrity of concrete, as demonstrated in the work of Pohl et al. [113]. To overcome these limitations, recent research has started to incorporate early-age effects and their coupled hygro-thermo-mechanical interactions into concrete models. For example, You et al. [147, 148] proposed a two-stage modeling framework specifically aimed at capturing early-age shrinkage driven by moisture and temperature gradients. Liang et al. [94] further extended this approach by developing a thermo-chemo-mechanical model enhanced with active ensemble learning to simulate stress development during early hydration. Nevertheless, this model remains restricted to moderate temperature ranges, limiting its ability to represent dehydration processes accurately. In parallel, stoichiometric modeling approaches based on the foundational work of Powers and Brownyard [114, 115] allow direct incorporation of hydration chemistry into the simulation. These chemically

informed models provide a more detailed and physically grounded representation of early-age concrete behavior, especially under variable thermal and moisture conditions.

(a) (b)

Figure 1.4: Stages of concrete hardening: (a) Fresh concrete in the initial setting phase and (b) Hardened concrete in the final stage of hardening.

It is crucial to distinguish between modeling concrete in its fresh, early stages and its later stages of hydration, both of which are illustrated in Figure 1.4. During the late stages of hydration, concrete undergoes considerable chemical and mechanical changes, including the formation of cementitious products. In contrast, modeling fresh concrete in its early hydration phase centers on understanding the evolution of material properties as hydration progresses, leading to mass and heat generation. The main difference between these stages lies in their microstructural complexity and their time-dependent mechanical behavior. In the initial hydration phase of concrete, intricate non-uniform deformations occur due to highly exothermic and thermally activated reactions within the cement particles. These reactions result in substantial heat generation, especially in large structures, which subsequently affects the material properties and alters the kinetics of the hydration process [8, 64]. Many existing models that focus on the early stages of concrete typically emphasize thermo-mechanical phenomena while often neglecting the impact of hygral processes. This oversight usually arises from the assumption, as noted in Cervera et al. [22], Ulm and Coussy [139, 140], that the saturation of fresh concrete with liquid water diminishes the significance of hygral effects. However, this assumption is not universally applicable, particularly for High-Performance Concrete (HPC) and Ultra-High-Performance Concrete (UHPC), where notable reductions in relative humidity can occur [9, 23, 139]. By considering hygral phenomena, we can introduce the concept of capillary pressure, which is defined as the pressure difference between the gas and water phases within concrete. Employing capillary pressure as a state variable has demonstrated effectiveness in various hygro-thermal modeling scenarios for concrete [59, 60, 61, 63, 113]. This method is particularly advantageous for analyzing stress states in concrete because of its direct

correlation with pressure [71, 72, 126]. Although some earlier concrete models, as noted in [8, 139], have refrained from integrating capillary pressure as a state variable due to theoretical challenges at the macroscale, recent advancements in thermodynamics [71, 72] have successfully addressed these concerns. By incorporating capillary pressure into our models, we can evaluate the full spectrum of moisture content in concrete—ranging from nearly dry conditions, which are common in later maturation stages, to full pore saturation, typical during early hydration. This integration enables the modeling of water under pressures that exceed atmospheric levels, which is essential for accurately capturing moisture transport in cementitious materials [59]. In fire scenarios, where external temperatures drastically exceed normal ambient conditions, the relationship between degree of saturation and capillary pressure becomes highly unstable. This instability arises from rapid thermal gradients, phase changes, and pressure-driven moisture redistribution. Such nonlinear and temperature-dependent coupling poses a significant challenge for predictive modeling. Foundational studies such as those by Dal Pont and Ehrlacher [30], Pohl et al. [113] have addressed and resolved many of the complexities in this coupling, laying the groundwork for robust hygro-thermo-mechanical simulations of concrete exposed to high temperatures. Consequently, capillary pressure, as advocated by researchers focused on soil and building materials [59, 63, 67], will be integrated into the current model.

By applying the principles of the Theory of Porous Media (TPM), as outlined in [44], concrete is classified as a porous material in works of Bazant and Najjar [9], Cervera et al. [23], Ulm and Coussy [139]. The TPM is based on the Hybrid Mixture Theory, which uses a continuum-mechanical framework to derive balance equations through the averaging theory developed by Hassanizadeh and Gray [76]. This approach effectively captures the complex microstructure of porous materials at the macroscopic level without detailed knowledge of their precise structure. TPM-based methods characterize the various components of a porous medium, treating individual aggregates within this multiphase framework and incorporating production terms. These production terms reflect the thermomechanical interactions among the material's constituents. This methodology effectively connects the macroscopic behavior of concrete to its underlying micro-level phenomena [44, 125]. Gawin et al. [64] introduced a model that encompasses the full coupling of thermal, chemical, and hygral phenomena by considering changes in the properties of concrete during its early hydration stages.

Building upon and extending the models proposed by Gawin et al. [64] and Sciumè et al. [130], the actual work introduces several key advancements to the modeling of early-age concrete behavior. Most notably, a novel formulation for the evaporation rate is proposed and rigorously calibrated using Dynamic Vapor Sorption (DVS) experiments, allowing for a more accurate representation of moisture loss during the critical early curing phase. The evaporation, often oversimplified or neglected in conventional models, is shown to significantly impact the hydration kinetics and the development of material properties in early-age hydration. The proposed model is validated through two independent test cases involving different concrete mixes. As part of this work, the model was further extended

to critically investigate the widely adopted assumption of a linear relationship between porosity and hydration degree—originally introduced by Powers and Brownyard [114] and commonly used in models such as [64, 130]. This analysis was carried out under varying environmental and material conditions, enabling a more thorough evaluation of the assumption's validity and limitations. A further significant advancement lies in the integration of a multiscale modeling approach for predicting the evolution of mechanical properties. In particular, the progression of Young's modulus is directly linked to hydration-driven strength gain through a thermodynamically consistent formulation. This coupling is embedded in a multiscale framework inspired by Pichler et al. [111], in which macroscopic stress states are projected onto the hydrate phase using the Drucker–Prager yield criterion. The model is validated using a benchmark problem and further applied to a practical case study from Jędrzejewska et al. [85], Königsberger et al. [88]. Calibration is conducted on a representative concrete mix and simulation results are assessed against both numerical and experimental reference data. The model effectively captures both material and geometrical nonlinearities, enabling a more realistic representation of the evolving mechanical behavior during hydration.

The model developed in this work is implemented using the open-source platform FEniCSx, which offers a modern, efficient framework for flexible prototyping, testing, and extension of finite element models through automated PDE-solving capabilities.

1.3 Outline of the thesis

Following the introduction, chapter 2 lays the theoretical foundation for modeling fresh concrete within the framework of the Theory of Porous Media. In this approach, concrete is treated as a multiphase system consisting of solid, liquid, and gas phases. The chapter also introduces the essential kinematic relations required for a nonlinear continuum formulation.

Chapter 3 defines the underlying model assumptions and establishes the thermodynamic framework. Core concepts from material theory are introduced and the entropy inequality is evaluated to derive thermodynamically consistent constitutive equations. The formulation of the Helmholtz free energy and a nonlinear isotropic elastic law tailored to fresh concrete conclude the chapter.

Chapter 4 presents the experimental setup, with a particular focus on the Dynamic Vapor Sorption technique used to investigate moisture exchange during the early curing period. While developing the model, the potential of incorporating this experimental method to calibrate the evaporation process within fresh concrete became evident. This chapter details the testing methodology, sample preparation and preliminary experiments, all of which provide reliable data for model calibration.

Chapter 5 describes the numerical implementation of the proposed model. The weak form of the governing equations is derived using the Galerkin method, with spatial discretization based on mixed finite elements and time integration performed using the implicit Euler scheme. An optimization procedure is introduced to support the calibration of the newly developed evaporation formulation.

Chapter 6 presents the calibration and validation of the model, including a novel evaporation formulation calibrated with DVS experiments. The model is extended to investigate the porosity–hydration relationship and predict the evolution of Young's modulus through a multiscale approach. Results are validated against experimental data and benchmark problems, demonstrating the model's ability to capture material and geometric nonlinearities.

Finally, chapter 7 summarizes the main findings of this work and provides an outlook on possible future directions in modeling the early-age behavior of concrete.

2 CONTINUUM-MECHANICAL FUNDAMENTALS OF THE THEORY OF POROUS MEDIA

The Theory of Porous Media (TPM) builds upon the Theory of Mixtures, incorporating the Concept of Volume Fractions. This foundational theory was first explored by Truesdell [138] and Bowen [16]. The introduction of volume fractions originated primarily from geotechnical studies by Biot [14] and Heinrich and Desoyer [78]. Bowen further advanced the Theory of Porous Media in his publications [17, 18], alongside contributions from de Boer and Ehlers [36, 39, 42, 43].

This section provides a brief overview of the continuum-mechanical principles necessary for understanding modeling within the framework of the Theory of Porous Media. Key concepts introduced include kinematic relations, polar and spectral decomposition, as well as measures of strain and stress.

2.1 Theoretical basis

The material model, composed of three individual constituents φ^α, can be comprehensively described through a macroscopic model. It consists of an immiscible solid phase ($\alpha = S$) that represents the solid skeleton and various fluid phases ($\alpha = F$) that occupy the material's void. The fluid phase consists of a liquid water ($\alpha = L$) and a gas ($\alpha = G$) phase filling the pores of the material. Within the framework of the macroscopic TPM such multiphase materials are accordingly characterized. This involves an averaging process over a representative elementary volume (REV), where the individual aggregates within the multiphase material are presumed to be in a state of ideal disorder, uniformly distributed across the domain. This results in a macroscopic representation of interconnected and superimposed continua

$$\varphi = \varphi^S + \varphi^L + \varphi^G, \tag{2.1}$$

of all three constituents of the multiphasic material. Following the homogenization process, all macroscopic quantities are considered as local averages of their microscopic counterparts, as illustrated in Figure 2.1 [47]. This means that every specific point in space, represented by $\mathbf{x}_\alpha$, contains material points $\mathbf{X}_\alpha$ from all the separate constituents [35]. Consequently, the mathematical functions characterizing the physical and geometrical attributes of this three-phase material are functions that span across the whole aggregate φ. Differing from the classical Theory of Mixtures, which deals with miscible constituents and lacks insight into the inner structure of the multiphase body, the Theory of Porous Media distinguishes between immiscible phases based on the partial volumes V^α within

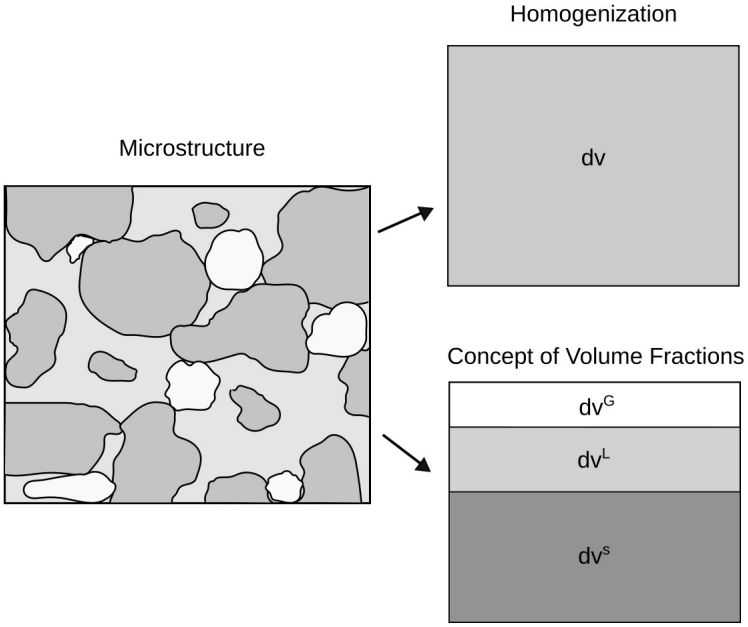

Figure 2.1: Representative elementary volume (REV) of a partially saturated porous microstructure (left) and the corresponding macroscale multiphase model based on the TPM (right) [47].

the overall medium. This distinction allows for the overall volume V of the multiphase body B to be expressed as the sum of partial volumes of its constituent parts

$$V = \int_V \mathrm{d}v = V^S + V^L + V^G \qquad \text{with} \qquad V^\alpha = \int_V \mathrm{d}v^\alpha = \int_V n^\alpha \mathrm{d}v. \tag{2.2}$$

Herein, the symbol n^α denotes the volume fraction of the individual constituents at a specific material point, where $\alpha \in \{S, L, G\}$ indicates all three constituents. These symbols are introduced to represent the local averages of the partial volume element $\mathrm{d}v^\alpha$ corresponding to φ^α, relative to the entire bulk volume element $\mathrm{d}v$ of φ. The summation of all volume fractions establishes the saturation state of the overall aggregate φ

$$n^\alpha(\mathbf{x},t) = \frac{\mathrm{d}v^\alpha}{\mathrm{d}v}, \qquad \sum_\alpha n^\alpha(\mathbf{x},t) = 1\,. \tag{2.3}$$

When we consider multiple fluid constituents φ^β, where $\beta \in \{L, G\}$, the volume fraction n^F for the complete fluid phase represents all the individual fluid phases φ^β

$$n^F = n^L + n^G = 1 - n^S. \tag{2.4}$$

By comparing the volume fractions n^β of the fluid components to the fluid volume fraction n^F, we determine the saturation s^β of these fluid phases

$$s^\beta = \frac{n^\beta}{n^F} \qquad \text{where} \qquad s^L + s^G = 1. \tag{2.5}$$

Equation (2.5) represents the fluid saturation condition. There are two density functions for the each constituent φ^α introduced as

$$\rho^{\alpha R} = \frac{\mathrm{d}m^\alpha}{\mathrm{d}v^\alpha} \qquad \text{and} \qquad \rho^\alpha = \frac{\mathrm{d}m^\alpha}{\mathrm{d}v}. \tag{2.6}$$

In this context, the material density $\rho^{\alpha R}$ represents the actual or effective locally averaged density of the constituent φ^α. It establishes a relation between the partial mass element $\mathrm{d}m^\alpha$ and partial volume element $\mathrm{d}v^\alpha$. Moreover, the partial density ρ^α, also known as global or bulk density, associates the same mass element with the bulk volume element $\mathrm{d}v$. With the help of the equation (2.3), a relation between the material and partial density emerges as

$$\rho^\alpha = n^\alpha \rho^{\alpha R}. \tag{2.7}$$

Finally, the total density ρ of the entire aggregate φ is obtained by summing up all the partial densities ρ^α

$$\rho = \sum_\alpha \rho^\alpha = \sum_\alpha n^\alpha \rho^{\alpha R}. \tag{2.8}$$

2.2 Kinematic relations

2.2.1 Motion function of the constituents

In continuum mechanics of single-phase materials, a coherent set of material points P characterizes the body $\mathcal{B}$ and its boundary $\partial\mathcal{B}$. Within the frameworks of the Theory of Porous Media, the body under consideration comprises material points P^α for each constituent φ^α. Starting from the positions of the material points in the reference configuration $\mathbf{X}_\alpha$, the motion function $\boldsymbol{\chi}_\alpha$ for the constituent φ^α is defined

$$\mathbf{x} = \boldsymbol{\chi}_\alpha(\mathbf{X}_\alpha, t). \tag{2.9}$$

At this stage, it is important to note that kinematical quantities are designated with a subscript, while all other quantities are indicated with a superscript. Following the previously mentioned homogenization process and the fundamental principles of the Theory of Mixtures, where superimposed continua are assumed to have internal interactions and distinct motions, each spatial point $\mathbf{x}$ at any given time t is simultaneously occupied by material points P^α of all constituents φ^α, which generally originate from different positions in the

reference configuration, as shown in Figure 2.2. The condition for establishing a unique relationship between the positions of the material points in the reference configuration and the current configuration is satisfied by the presence of unique inverse motion functions

$$\mathbf{X}_\alpha = \boldsymbol{\chi}_\alpha^{-1}(\mathbf{x},t). \tag{2.10}$$

The inverse motion $\boldsymbol{\chi}_\alpha^{-1}$ of each constituent φ^α exists only under the assumption that the Jacobian determinants J_α are non-zero

$$J_\alpha := \det\frac{\partial \boldsymbol{\chi}_\alpha}{\partial \mathbf{X}_\alpha} \neq 0. \tag{2.11}$$

Subsequently, independent velocity and acceleration fields can be expressed either within the Lagrangian description, also known as material description

$$\mathbf{x}'_\alpha(\mathbf{X}_\alpha,t) = \frac{\mathrm{d}}{\mathrm{d}t}\boldsymbol{\chi}_\alpha(\mathbf{X}_\alpha,t) \qquad \text{and} \qquad \mathbf{x}''_\alpha(\mathbf{X}_\alpha,t) = \frac{\mathrm{d}^2}{\mathrm{d}t^2}\boldsymbol{\chi}_\alpha(\mathbf{X}_\alpha,t), \tag{2.12}$$

or, using the inverse motion function, within the Eulerian or spatial framework

$$\mathbf{x}'_\alpha(\mathbf{x},t) = \mathbf{x}'_\alpha[\boldsymbol{\chi}_\alpha^{-1}(\mathbf{x},t),t] \qquad \text{and} \qquad \mathbf{x}''_\alpha(\mathbf{x},t) = \mathbf{x}''_\alpha[\boldsymbol{\chi}_\alpha^{-1}(\mathbf{x},t),t]. \tag{2.13}$$

In Lagrangian representation, the constituent is described in relation to the reference configuration, whereas in an Eulerian representation, it is described in terms of the current configuration. All time derivatives $(\cdot)'$ and $(\cdot)'_\alpha$ are material time derivatives. In the case of the Lagrangian description, the material time derivative reduces to the partial time derivative due to the reference positions $\mathbf{X}_\alpha$ fixed in time. If f is an arbitrary, continuous, and sufficiently differentiable scalar function of $(\mathbf{x},t)$, the material time derivative of f following the motion of φ_α yields

$$(f)'_\alpha = \frac{\mathrm{d}_\alpha}{\mathrm{d}t}f(\mathbf{x},t) = \frac{\partial f}{\partial t} + \frac{\partial f}{\partial \mathbf{x}}(\frac{\partial \mathbf{x}}{\partial t})_\alpha = \frac{\partial f}{\partial t} + \mathrm{grad} f \cdot \mathbf{x}'_\alpha, \tag{2.14}$$

where the operator $\mathrm{grad}(\cdot)$ denotes the gradient of $(\cdot)$ with respect to the current position $\mathbf{x}$. The first term on the right-hand side of (2.14) is referred to as the local part, while the second term is known as the convective part. A velocity field is termed stationary if the local part, i.e., the partial time derivative, is zero. When considering a vector-valued function $\mathbf{f}(\mathbf{x},t)$, the material time derivative is expressed by

$$(\mathbf{f})'_\alpha = \frac{\mathrm{d}_\alpha}{\mathrm{d}t}\mathbf{f}(\mathbf{x},t) = \frac{\partial \mathbf{f}}{\partial t} + \mathrm{grad}\mathbf{f}\,\mathbf{x}'_\alpha. \tag{2.15}$$

In modeling coupled solid-fluid problems, it is advantageous to describe the solid phase using a Lagrangian approach, where the displacement vector $\mathbf{u}_S$ serves as the primary kinematic variable. The time derivatives of the displacement vector are given by

$$(\mathbf{u}_S)'_S = \mathbf{v}_S = \mathbf{x}'_S \qquad \text{with} \qquad (\mathbf{u}_S)''_S = (\mathbf{v}_S)'_S = \mathbf{x}''_S. \tag{2.16}$$

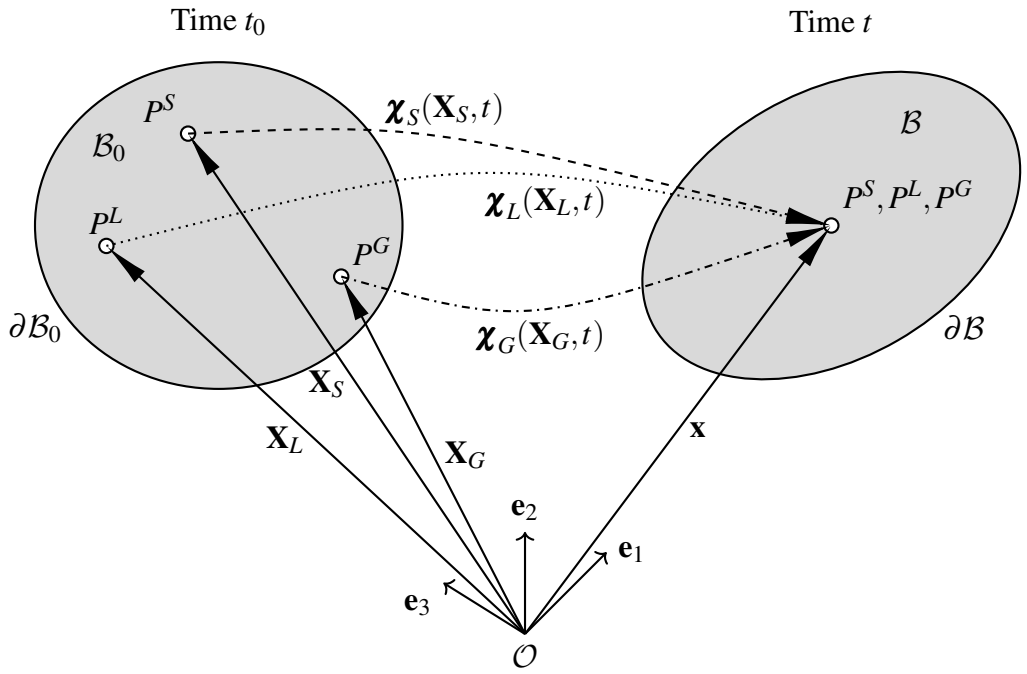

Figure 2.2: Motion of a triphasic porous material model.

In contrast, the fluid phases are more effectively represented using a modified Eulerian description relative to the deformable solid skeleton. Here, the motion of the pore-fluid constituent φ^β is analyzed in relation to the solid motion. In this context, and similar to the definition of the material time derivative, the fluid-particle acceleration incorporates a convective contribution defined with respect to the deforming solid skeleton

$$(\mathbf{v}_\beta)'_S = (\mathbf{v}_\beta)'_\beta - (\mathrm{grad}\mathbf{v}_\beta)\mathbf{w}_{\beta S}, \qquad \text{with} \qquad \mathbf{w}_\beta = \mathbf{v}_\beta - \mathbf{v}_S. \tag{2.17}$$

$\mathbf{v}_\beta$ denotes the velocity of a pore-fluid particle of φ^β, while $\mathbf{w}_{\beta S}$ represents the corresponding seepage velocity. The diffusion velocity for a particle of φ^α, defined as its relative velocity concerning the barycentric velocity of the overall aggregate, is given by

$$\mathbf{d}_\alpha = \mathbf{x}'_\alpha - \mathbf{x}' \qquad \text{with} \qquad \rho^\alpha \mathbf{d}_\alpha = \rho^\alpha \mathbf{x}'_\alpha - \rho^\alpha \mathbf{x}'. \tag{2.18}$$

The term $\rho^\alpha \mathbf{d}_\alpha$ signifies the diffusive mass flow, while $\rho^\alpha \mathbf{x}'$ corresponds to the mass flow associated with the barycentric velocity. This formulation provides a comprehensive understanding of the interactions between the solid and fluid phases within the framework of coupled solid-fluid mechanics. Based on the velocity fields of the individual constituents, the velocity of the overall medium can be also expressed as

$$\mathbf{x}' = \frac{1}{\rho} \sum_\alpha \rho^\alpha \mathbf{x}'_\alpha, \tag{2.19}$$

which defines the barycentric velocity of the entire aggregate. By substituting the first equation into the second of (2.18) and further incorporating equations (2.19) and (2.8), we can conclude that the sum of the diffusive mass flows vanishes

$$\sum_{\alpha} \rho^{\alpha} \mathbf{v}_{\alpha} = 0. \tag{2.20}$$

2.2.2 Deformation gradient

Deformation and strain measures can be defined by comparing the squared line elements between two adjacent material points in both the reference and current configurations. Generally, all deformation measures are derived from the material deformation gradient $\mathbf{F}_{\alpha}$ and its inverse $\mathbf{F}_{\alpha}^{-1}$

$$\mathbf{F}_{\alpha} = \mathrm{Grad}_{\alpha}\mathbf{x} =: \frac{\partial \chi_{\alpha}(\mathbf{X}_{\alpha}, t)}{\partial \mathbf{X}_{\alpha}} \qquad \text{and} \qquad \mathbf{F}_{\alpha}^{-1} = \mathrm{grad}_{\alpha}\mathbf{X}_{\alpha} =: \frac{\partial \chi_{\alpha}^{-1}(\mathbf{x}, t)}{\partial \mathbf{x}}. \tag{2.21}$$

The Jacobian determinant now can be given as

$$J_{\alpha} = \det \mathbf{F}_{\alpha}, \tag{2.22}$$

where in its initial state for the time $t = 0$ holds $\det \mathbf{F}_{\alpha} = 1$. The Jacobian determinant is constrained to positive values only. From equation (2.17), the solid displacement vector serves as the primary kinematic quantity, while the fluid motion is represented in relation to the deforming solid. As a result, the deformation gradient for the fluids, denoted as $\mathbf{F}_F$, is not required. Instead, the solid deformation gradient $\mathbf{F}_S$ is the primary kinematic quantity. Furthermore, $\mathbf{F}_S$ and its inverse $\mathbf{F}_S^{-1}$ can be expressed in terms of the solid displacement using equations (2.17) and (2.21)

$$\mathbf{F}_S = \mathbf{I} + \mathrm{Grad}_S \mathbf{u}_S \qquad \text{and} \qquad \mathbf{F}_S^{-1} = \mathbf{I} - \mathrm{grad}\, \mathbf{u}_S. \tag{2.23}$$

Consequently, utilizing these so-called two-field tensors, the line element $\mathrm{d}\mathbf{X}_{\alpha}$ of the reference configuration can be transformed to the line element $\mathrm{d}\mathbf{x}$ of the current configuration (also known as push-forward operation)

$$\mathrm{d}\mathbf{x} = \mathbf{F}_{\alpha}\, \mathrm{d}\mathbf{X}_{\alpha} \qquad \text{and} \qquad \mathrm{d}\mathbf{X}_{\alpha} = \mathbf{F}_{\alpha}^{-1}\, \mathrm{d}\mathbf{x} \tag{2.24}$$

or alternatively with pull-back operation. Further geometric transport mechanisms include the contravariant push-forward transport of the reference quantities of the oriented area elements $\mathrm{d}\mathbf{A}_{\alpha}$ and the transport of the volume elements $\mathrm{d}V_{\alpha}$ to their corresponding current quantities $\mathrm{d}\mathbf{a}$ and $\mathrm{d}v$ respectively

$$\mathrm{d}\mathbf{a} = (\det \mathbf{F}_{\alpha})(\mathbf{F}_{\alpha}^{T})^{-1}\, \mathrm{d}\mathbf{A}_{\alpha}, \tag{2.25}$$

$$\mathrm{d}v = (\det \mathbf{F}_{\alpha})\, \mathrm{d}V_{\alpha}. \tag{2.26}$$

For a more in-depth exploration of this topic, the interested reader is referred to [35, 39].

2.2.3 Deformation and strain measures

After introducing the deformation gradient, the deformation and strain measures are defined. The deformation measure describes how a body changes shape during motion, whereas the strain measure assesses the changes relative to the original, undeformed state. To define these deformation measures, we utilize the polar decomposition of the deformation gradient $\mathbf{F}_S$. This decomposition uniquely separates the deformation gradient into two parts, the symmetric and positive definite stretch tensors $\mathbf{U}_S$, $\mathbf{V}_S$ and the proper orthogonal rotation tensor $\mathbf{R}_S$

$$\mathbf{F}_S = \mathbf{V}_S\mathbf{R}_S = \mathbf{R}_S\mathbf{U}_S. \tag{2.27}$$

The expression $\mathbf{V}_S\mathbf{R}_S$ denotes the left decomposition of deformation gradient, with $\mathbf{V}_S$ referred to as the left stretch tensor, while $\mathbf{R}_S\mathbf{U}_S$ represents the right decomposition, where $\mathbf{U}_S$ is known as the right stretch tensor. Using these two stretch tensors, we can define the mapping of a line element $\mathrm{d}\mathbf{X}_S$ in the reference configuration to the line element $\mathrm{d}\mathbf{x}$ in the current configuration in two ways

$$\mathrm{d}\mathbf{x} = \mathbf{V}_S(\mathbf{R}_S\,\mathrm{d}\mathbf{X}_S) = \mathbf{R}_S(\mathbf{U}_S\,\mathrm{d}\mathbf{X}_S). \tag{2.28}$$

Using the definition of the material deformation gradient, the length of the current line element $\mathrm{d}\mathbf{x}$ can be expressed in terms of the reference configuration

$$\begin{aligned} \|\,\mathrm{d}\mathbf{x}\|^2 = \mathrm{d}\mathbf{x}\cdot\mathrm{d}\mathbf{x} &= (\mathbf{F}_S\,\mathrm{d}\mathbf{X}_S)\cdot(\mathbf{F}_S\,\mathrm{d}\mathbf{X}_S) \\ &= \mathrm{d}\mathbf{X}_S\cdot(\mathbf{F}_S^T\mathbf{F}_S)\,\mathrm{d}\mathbf{X}_S = \mathrm{d}\mathbf{X}_S\cdot\mathbf{C}_S\,\mathrm{d}\mathbf{X}_S, \end{aligned} \tag{2.29}$$

which helps us to obtain the right Cauchy-Green deformation tensor $\mathbf{C}_S = \mathbf{F}_S^T\mathbf{F}_S$. Furthermore, with the examination of the variation in the length of the line elements in the current configuration

$$\begin{aligned} \|\,\mathrm{d}\mathbf{X}_S\|^2 = \mathrm{d}\mathbf{X}_S\cdot\mathrm{d}\mathbf{X}_S &= (\mathbf{F}_S^{-1}\,\mathrm{d}\mathbf{x})\cdot(\mathbf{F}_S^{-1}\,\mathrm{d}\mathbf{x}) \\ &= \mathrm{d}\mathbf{x}\cdot(\mathbf{F}_S^{-T}\mathbf{F}_S^{-1})\,\mathrm{d}\mathbf{x} = \mathrm{d}\mathbf{x}\cdot\mathbf{B}_S^{-1}\,\mathrm{d}\mathbf{x}, \end{aligned} \tag{2.30}$$

the left Cauchy-Green deformation tensor, $\mathbf{B}_S = \mathbf{F}_S\mathbf{F}_S^T$, is obtained. The right and left Cauchy-Green tensors can be expressed also with help of stretch tensors

$$\begin{aligned} \mathbf{C}_S &= \mathbf{F}_S^T\mathbf{F}_S = (\mathbf{R}_S\mathbf{U}_S)^T(\mathbf{R}_S\mathbf{U}_S) = \mathbf{U}_S\mathbf{U}_S^T, \\ \mathbf{B}_S &= \mathbf{F}_S\mathbf{F}_S^T = (\mathbf{V}_S\mathbf{R}_S)(\mathbf{V}_S\mathbf{R}_S)^T = \mathbf{V}_S\mathbf{V}_S^T, \end{aligned} \tag{2.31}$$

and can be related through the forward and backward rotations

$$\mathbf{C}_S = \mathbf{R}_S^T\mathbf{B}_S\mathbf{R}_S \qquad \text{and} \qquad \mathbf{B}_S = \mathbf{R}_S\mathbf{C}_S\mathbf{R}_S^T. \tag{2.32}$$

We now introduce the strain tensors, which describe the material's state in the current configuration to that in the reference configuration. They effectively capture the body's

deformation at any given time t. The focus is on two nonlinear strain tensors, the Green-Lagrangian tensor $\mathbf{E}_S$ and the Euler-Almansi tensor $\mathbf{A}_S$. The Green-Lagrangian strain $\mathbf{E}_S$ is derived from equation (2.29)

$$\mathrm{d}\mathbf{x}\cdot\mathrm{d}\mathbf{x}-\mathrm{d}\mathbf{X}_S\cdot\mathrm{d}\mathbf{X}_S=\mathrm{d}\mathbf{X}_S\cdot(\mathbf{C}_S-\mathbf{I})\,\mathrm{d}\mathbf{X}_S=\mathrm{d}\mathbf{X}_S\cdot(2\mathbf{E}_S)\,\mathrm{d}\mathbf{X}_S, \tag{2.33}$$

which results in $\mathbf{E}_S=\frac{1}{2}(\mathbf{C}_S-\mathbf{I})$. Using the same equation (2.30), the Euler-Almansi strain $\mathbf{A}_S$ is similarly derived

$$\mathrm{d}\mathbf{x}\cdot\mathrm{d}\mathbf{x}-\mathrm{d}\mathbf{X}_S\cdot\mathrm{d}\mathbf{X}_S=\mathrm{d}\mathbf{x}\cdot(\mathbf{I}-\mathbf{B}_S^{-1})\,\mathrm{d}\mathbf{x}=\mathrm{d}\mathbf{x}\cdot(2\mathbf{A}_S)\,\mathrm{d}\mathbf{x}, \tag{2.34}$$

to give the relation $\mathbf{A}_S=\frac{1}{2}(\mathbf{I}-\mathbf{B}_S^{-1})$. The Euler-Almansi strain tensor represents the push-forward of the Green-Lagrangian strain tensor and is defined in the current configuration. Conversely, the Green-Lagrangian strain is the pull-back of the Euler-Almansi strain and is defined in the reference configuration, as given by

$$\mathbf{E}_S=\frac{1}{2}(\mathbf{C}_S-\mathbf{I})=\mathbf{F}_S^T(\mathbf{A}_S)\mathbf{F}_S \qquad \text{and} \qquad \mathbf{A}_S=\frac{1}{2}(\mathbf{I}-\mathbf{B}_S^{-1})=\mathbf{F}_S^{-T}(\mathbf{E}_S)\mathbf{F}_S^{-1}. \tag{2.35}$$

There are additional methods to define strain measures. For more detailed information on the strain tensors, the reader is referred to Bonet & Wood [15] and Ehlers & Bluhm [47].

2.2.4 Spectral decomposition

In constitutive modeling, it is often useful to represent deformation tensors in spectral form. We introduce the orthogonal and normalized eigenvectors $\hat{\mathbf{N}}_S^i\neq\mathbf{0}$ in the reference configuration, along with the corresponding eigenvalues λ_S^i for the right stretch tensor $\mathbf{U}_S$

$$\begin{aligned}&\mathbf{U}_S\hat{\mathbf{N}}_S^i=\lambda_S^i\hat{\mathbf{N}}_S^i, \quad \text{with} \quad i=1,2,3,\\ &\mathbf{C}_S\hat{\mathbf{N}}_S^i=\mathbf{U}_S^2\hat{\mathbf{N}}_S^i=(\lambda_S^i)^2\hat{\mathbf{N}}_S^i.\end{aligned} \tag{2.36}$$

Equations (2.36) show that both $\mathbf{U}_S$ and $\mathbf{C}_S$ have the same eigenvectors $\hat{\mathbf{N}}_S^i$, but their eigenvalues differ. The eigenvalues λ_S^i of $\mathbf{U}_S$ are referred to as principal stretches, while the eigenvalues of $\mathbf{C}_S$ are the squares of these principal stretches, denoted as $(\lambda_S^i)^2$. With the relation $\mathbf{V}_S=\mathbf{R}_S\mathbf{U}_S\mathbf{R}_S^T$ and the fact that $\mathbf{R}_S^T\mathbf{R}_S=\mathbf{I}$, we can derive the eigenvalue problem for $\mathbf{V}_S$ and $\mathbf{B}_S$

$$\begin{aligned}&\mathbf{V}_S(\mathbf{R}_S\hat{\mathbf{N}}_S^i)=\mathbf{R}_S\mathbf{U}_S\hat{\mathbf{N}}_S^i=\lambda_S^i(\mathbf{R}_S\hat{\mathbf{N}}_S^i),\\ &\mathbf{B}_S(\mathbf{R}_S\hat{\mathbf{N}}_S^i)=\mathbf{V}_S^2(\mathbf{R}_S\hat{\mathbf{N}}_S^i)=(\lambda_S^i)^2(\mathbf{R}_S\hat{\mathbf{N}}_S^i).\end{aligned} \tag{2.37}$$

We introduce the eigenvalue problem for (2.37) showing that both $\mathbf{V}_S$ and $\mathbf{B}_S$ share the same eigenvectors $\mathbf{R}_S\hat{\mathbf{N}}_S^i$, but their eigenvalues differ, being λ_S^i and $(\lambda_S^i)^2$, respectively.

The eigenvectors $\hat{\mathbf{N}}_S^i$ in the reference configuration are rotated to yield the orthogonal and normalized eigenvectors $\hat{\mathbf{n}}_S^i \neq \mathbf{0}$ in the current configuration $\hat{\mathbf{n}}_S^i = \mathbf{R}_S \hat{\mathbf{N}}_S^i$ and help with the spectral decomposition of the deformation gradient $\mathbf{F}_S$

$$\mathbf{F}_S = \mathbf{R}_S \mathbf{U}_S = \mathbf{R}_S \sum_{i=1}^{3} \lambda_S^i \hat{\mathbf{N}}_S^i \otimes \hat{\mathbf{N}}_S^i = \sum_{i=1}^{3} \lambda_S^i \hat{\mathbf{n}}_S^i \otimes \hat{\mathbf{N}}_S^i. \tag{2.38}$$

Furthermore, we introduce the principal invariants I_S, II_S, and III_S as

$$\begin{aligned} I_S &= I_{\mathbf{C}_S} = \operatorname{tr} \mathbf{C}_S = \mathbf{C}_S : \mathbf{I} = \mathbf{F}_S : \mathbf{F}_S, \\ II_S &= II_{\mathbf{C}_S} = \operatorname{cof} \mathbf{C}_S : \mathbf{I} = \frac{1}{2} \left[(\operatorname{tr} \mathbf{C}_S)^2 - \operatorname{tr}(\mathbf{C}_S \cdot \mathbf{C}_S) \right], \\ III_S &= III_{\mathbf{C}_S} = \det \mathbf{C}_S = (\det \mathbf{F}_S)^2. \end{aligned} \tag{2.39}$$

In case that the eigenvalues λ_S^i are known, the principal invariants can be calculated

$$\begin{aligned} I_S &= \sum_{i=1}^{3} \lambda_S^i = \lambda_S^1 + \lambda_S^2 + \lambda_S^3, \\ II_S &= \frac{1}{2} \sum_{\substack{i,j=1 \\ i \neq j}}^{3} \lambda_S^i \lambda_S^j = \lambda_S^1 \lambda_S^2 + \lambda_S^2 \lambda_S^3 + \lambda_S^3 \lambda_S^1, \\ III_S &= \prod_{i=1}^{3} \lambda_S^i = \lambda_S^1 \lambda_S^2 \lambda_S^3. \end{aligned} \tag{2.40}$$

2.2.5 Deformation and strain rates

Starting from the Lagrangian description of the constituent φ_α, the material velocity gradient is expressed as the total time derivative of the material deformation gradient (2.14) with respect to the constituent φ_α, as stated in (2.21)

$$(\mathbf{F}_\alpha)'_\alpha = \frac{\mathrm{d}_\alpha}{\mathrm{d}t} \mathbf{F}_\alpha = \frac{\mathrm{d}}{\mathrm{d}t} \left(\frac{\partial \mathbf{x}(\mathbf{X}_\alpha, t)}{\partial \mathbf{X}_\alpha} \right) = \frac{\partial \mathbf{x}'_\alpha(\mathbf{X}_\alpha, t)}{\partial \mathbf{X}_\alpha} = \operatorname{Grad}_\alpha \mathbf{x}'_\alpha. \tag{2.41}$$

Conversely, when adopting an Eulerian description of the constituent φ_α, the total time derivative of the material deformation gradient can be calculated

$$(\mathbf{F}_\alpha)'_\alpha = \frac{\partial \mathbf{x}'_\alpha(\mathbf{x}, t)}{\partial \mathbf{x}} \frac{\partial \mathbf{x}}{\partial \mathbf{X}_\alpha} = \mathbf{L}_\alpha \mathbf{F}_\alpha, \tag{2.42}$$

with $\mathbf{L}_\alpha$ representing the spatial velocity gradient of the constituent φ_α. Furthermore, we can define the spatial velocity gradient as

$$\mathbf{L}_\alpha = (\mathbf{F}_\alpha)'_\alpha \mathbf{F}_\alpha^{-1} = \operatorname{grad} \mathbf{x}'_\alpha \qquad \text{and} \qquad \mathbf{L}_\alpha : \mathbf{I} = \operatorname{div} \mathbf{x}'_\alpha. \tag{2.43}$$

For further applications, it is useful to decompose $\mathbf{L}_\alpha$ into a symmetric deformation velocity $\mathbf{D}_\alpha = \mathbf{D}_\alpha^T$ and a skew-symmetric spin tensor $\mathbf{W}_\alpha = -\mathbf{W}_\alpha^T$ leading to

$$\mathbf{L}_\alpha = \mathbf{D}_\alpha + \mathbf{W}_\alpha \qquad \text{with} \qquad \mathbf{D}_\alpha = \frac{1}{2}(\mathbf{L}_\alpha + \mathbf{L}_\alpha^T) \quad \text{and} \quad \mathbf{W}_\alpha = \frac{1}{2}(\mathbf{L}_\alpha - \mathbf{L}_\alpha^T). \tag{2.44}$$

Subsequently, the material time derivative of the right Cauchy-Green deformation tensor is utilized to

$$(\mathbf{C}_\alpha)'_\alpha = (\mathbf{F}_\alpha^T \mathbf{F}_\alpha)'_\alpha = 2\mathbf{F}_\alpha^T \mathbf{D}_\alpha \mathbf{F}_\alpha, \tag{2.45}$$

and the rate of the Green-Lagrangian strain tensor expressed as

$$(\mathbf{E}_\alpha)'_\alpha = \frac{1}{2}(\mathbf{C}_\alpha)'_\alpha = \mathbf{F}_\alpha^T \mathbf{D}_\alpha \mathbf{F}_\alpha. \tag{2.46}$$

2.2.6 Stress measures

Stress represents the internal force response of a material per unit area. Depending on whether the area is measured in the deformed or reference configuration, different stress measures such as Cauchy and Piola-Kirchhoff are introduced to describe the material behavior in a consistent and frame-invariant manner. The surface traction vector $\mathbf{t}^\alpha(\mathbf{x},t;\mathbf{n})$ describes the effects of contact forces acting on the material points at the surface ∂B, characterized by the outward-oriented unit surface normal $\mathbf{n}$ of the current configuration. According to Cauchy's theorem

$$\mathbf{t}^\alpha(\mathbf{x},t;\mathbf{n}) = \mathbf{T}^\alpha(\mathbf{x},t)\mathbf{n}, \tag{2.47}$$

$\mathbf{T}^\alpha$ represents the partial Cauchy stress tensor of a constituent φ^α in the current configuration. Therefore, the field function $\mathbf{T}^\alpha$ serves as a stress measure that is independent of the specific surface characterized by $\mathbf{n}$. The quantity $\mathbf{T}^\alpha$ relates the contact force $\mathrm{d}\mathbf{k}^\alpha$ acting on the constituent φ^α to the oriented area element da of the current configuration as

$$\mathrm{d}\mathbf{k}^\alpha = \mathbf{t}^\alpha \,\mathrm{da} = (\mathbf{T}^\alpha \mathbf{n})\,\mathrm{da} = \mathbf{T}^\alpha(\mathbf{n}\,\mathrm{da}) = \mathbf{T}^\alpha\,\mathrm{d}\mathbf{a}. \tag{2.48}$$

Here, $\mathbf{T}^\alpha$ is commonly referred to as the true stress tensor. Furthermore, by expressing the contact force in terms of an area element $\mathrm{d}\mathbf{A}_\alpha$ in the reference configuration, as described by the surface element transformation in (2.25), one arrives at the definition of the partial first Piola–Kirchhoff stress tensor $\mathbf{P}^\alpha$. Similar to the material deformation gradient $\mathbf{F}_\alpha$, this tensor is a two-field tensor, as only the second basis is pulled back to the reference configuration. Consequently, the contact force $\mathrm{d}\mathbf{k}^\alpha$ can be expressed as

$$\begin{aligned} \mathrm{d}\mathbf{k}^\alpha &= (\det\mathbf{F}_\alpha)\mathbf{T}^\alpha\,\mathrm{d}\bar{\mathbf{a}}_\alpha =: \tau^\alpha\,\mathrm{d}\bar{\mathbf{a}}_\alpha \\ &= (\det\mathbf{F}_\alpha)\mathbf{T}^\alpha(\mathbf{F}_\alpha^T)^{-1}\,\mathrm{d}\mathbf{A}_\alpha =: \mathbf{P}^\alpha\,\mathrm{d}\mathbf{A}_\alpha. \end{aligned} \tag{2.49}$$

The first Piola-Kirchhoff stress is particularly important from an experimental perspective, as it relates forces to the undeformed surfaces. Given that we have stress measures in the current configuration ($\mathbf{T}^\alpha$) as well as a two-field stress measure ($\mathbf{P}^\alpha$), we will now introduce the second Piola-Kirchhoff stress $\mathbf{S}^\alpha$ in the reference configuration. This stress is defined as the pull-back of the Kirchhoff stress

$$\mathbf{S}^\alpha := \mathbf{F}_\alpha^{-1} \tau^\alpha \mathbf{F}^{-T}. \tag{2.50}$$

2.3 Balance relations

The deformation and thermal processes of a continuum body B are described by fundamental balance relations. The axiomatic introduction of conservation equations in continuum mechanics of single-phasic materials is grounded in the observation that certain physical quantities are neither created nor destroyed within a closed system. These involve mass, linear momentum, angular momentum, energy (1-st law of thermodynamics) and entropy (2-nd law of thermodynamics) balances, which are established through direct observations. For a constituent φ^α within a whole mixture φ, we must account for its inherent physical

Description of the single-phase balance relations

mass	In a closed system, the mass of a body remains constant.
momentum	The rate of change of the body's momentum is equal to the sum of the forces acting on it, both locally and from a distance.
angular momentum	The rate of change of the body's angular momentum equals the total moment from all forces acting on the body, calculated with respect to a common reference point.
energy	The total rate of change of a body's internal and kinetic energy equals the total external mechanical and non-mechanical power, in accordance with the first law of thermodynamics.
entropy	(1) The rate of change of entropy within a body is the sum of the external change in entropy and the internal entropy production. (2) The entropy production is always non-negative, as stated by the second law of thermodynamics.

attributes as well as the effects stemming from interactions with other constituents. These interconnections dictate the inclusion of additional terms for mass, momentum, energy, etc., specific to each constituent. When mathematically describing multiphasic materials, Truesdell [138] introduced the fundamental notions of mixtures known as "metaphysical principles" By summing the balance equations for all constituents φ^α, we obtain the balance equation for the overall porous medium φ. Furthermore, a specific constituent φ^α

***Truesdell's* metaphysical principles taken from [138]**

1. *All properties of the mixture must be mathematical consequences of properties of the constituents.*
2. *So as to describe the motion of a constituent, we may in imagination isolate it from the rest of the mixture, provided we allow properly for the actions of the other constituents upon it.*
3. *The motion of the mixture is governed by the same equations as is a single body.*

can be described using the balance relations typical of a single-phasic material, as long as these relations are enhanced with terms that account for interactions with other phases within the multiphasic body. Consequently, the balance equations for the entire aggregate follow the principles of classical continuum mechanics.

Upon examining the individual balance relations, we can identify a general structure. This general structure will be presented through the so-called master balance for both the entire porous material and its individual constituents. Following that, we will specify the introduced mechanical quantities in relation to the particular mechanical and thermodynamic quantities applicable to each balance relation. This presentation follows the methodology established by Ehlers [43], de Boer [35], Truesdell [138] and Holzapfel [81].

2.3.1 General structure of the balance relations

All fundamental balance relations can be generally described through a comprehensive form, often referred to as the "master balance" [77]. Using this global formulation, a general structure for a volume-specific scalar quantity Ψ and a vector-valued mechanical quantity $\boldsymbol{\Psi}$, representing the behavior of the entire body $\mathcal{B}$, is introduced. The global balance relations for these quantities are

$$\begin{aligned} \frac{\mathrm{d}}{\mathrm{d}t}\int_{\mathcal{B}} \Psi \,\mathrm{d}v &= \int_{\partial\mathcal{B}} (\boldsymbol{\phi}\cdot\mathbf{n})\,\mathrm{d}a + \int_{\mathcal{B}} \sigma \,\mathrm{d}v + \int_{\mathcal{B}} \hat{\Psi}\,\mathrm{d}v, \\ \frac{\mathrm{d}}{\mathrm{d}t}\int_{\mathcal{B}} \boldsymbol{\Psi} \,\mathrm{d}v &= \int_{\partial\mathcal{B}} (\boldsymbol{\Phi}\mathbf{n})\,\mathrm{d}a + \int_{\mathcal{B}} \boldsymbol{\sigma} \,\mathrm{d}v + \int_{\mathcal{B}} \hat{\boldsymbol{\Psi}}\,\mathrm{d}v. \end{aligned} \tag{2.51}$$

These balance equations encompass a variety of fundamental physical quantities, including mass, linear momentum, angular momentum, total energy (which includes both internal and kinetic energy), and entropy. The terms $\boldsymbol{\phi}\cdot\mathbf{n}$ and $\boldsymbol{\Phi}\,\mathbf{n}$ represent the fluxes of mechanical quantities per unit area of the current configuration, contributing directly to the body $\mathcal{B}$

through its surface $\partial\mathcal{B}$, where $\mathbf{n}$ is the outward-oriented normal vector at the surface point $\mathbf{x} \in \partial\mathcal{B}$.

The symbols σ and $\boldsymbol{\sigma}$ denote the supply of external mechanical quantities per unit volume, while $\hat{\Psi}$ and $\hat{\boldsymbol{\Psi}}$ account for production terms that may result from internal interactions or coupling effects within the body and its environment. Applying the material time derivative to these mechanical quantities and utilizing divergence theorem to convert surface integrals over $\partial\mathcal{B}$ into volume integrals over $\mathcal{B}$, the local representation of the master balance equations can be expressed

$$\begin{aligned} \dot{\Psi} + \Psi \operatorname{div}(\dot{\mathbf{x}}) &= \operatorname{div}(\boldsymbol{\phi}) + \sigma + \hat{\Psi}, \\ \dot{\boldsymbol{\Psi}} + \boldsymbol{\Psi} \operatorname{div}(\dot{\mathbf{x}}) &= \operatorname{div}(\boldsymbol{\Phi}) + \boldsymbol{\sigma} + \hat{\boldsymbol{\Psi}}. \end{aligned} \tag{2.52}$$

These balance principles are universally applicable to any deformable body $\mathcal{B}$ and must be satisfied at all times. They serve as the foundation for modeling the conservation of mass, linear and angular momentum, energy, and entropy within the context of continuum mechanics. The following table outlines the specific forms of the quantities Ψ, $\boldsymbol{\Psi}$, $\boldsymbol{\phi}$, $\boldsymbol{\Phi}$, σ, $\boldsymbol{\sigma}$, $\hat{\Psi}$, and $\hat{\boldsymbol{\Psi}}$ for each of the fundamental balance laws

	$\Psi, \boldsymbol{\Psi}$	$\boldsymbol{\phi}, \boldsymbol{\Phi}$	$\sigma, \boldsymbol{\sigma}$	$\hat{\Psi}, \hat{\boldsymbol{\Psi}}$
mass	ρ	$\mathbf{0}$	0	0
momentum	$\rho\dot{\mathbf{x}}$	$\mathbf{T}$	$\rho\mathbf{b}$	0
ang. momentum	$\mathbf{x} \times (\rho\dot{\mathbf{x}})$	$\mathbf{x} \times \mathbf{T}$	$\mathbf{x} \times (\rho\mathbf{b})$	0
energy	$\rho\varepsilon + \frac{1}{2}\dot{\mathbf{x}} \cdot (\rho\dot{\mathbf{x}})$	$\mathbf{T}^T\dot{\mathbf{x}} - \mathbf{q}$	$\dot{\mathbf{x}} \cdot (\rho\mathbf{b}) + \rho r$	0
entropy	$\rho\eta$	$\boldsymbol{\phi}_\eta$	σ_η	$\hat{\eta} \geq 0$

(2.53)

Here, $\rho\dot{\mathbf{x}}$ represents the momentum of the aggregate, $\mathbf{T}$ is the Cauchy stress tensor, and $\mathbf{b}$ is the external volume force per unit mass. The expression $\mathbf{x} \times (\rho\dot{\mathbf{x}})$ yields the angular momentum (written as ang. momentum), while ε denotes the internal energy of the whole aggregate. Moreover, $\mathbf{q}$ is the heat influx vector, and r is the external heat supply. The quantity η represents the entropy, while $\boldsymbol{\phi}_\eta$ and σ_η denote the entropy efflux and external entropy supply, respectively. Importantly, $\hat{\eta}$ is the entropy production, which must always be non-negative ($\hat{\eta} \geq 0$) in accordance with the second law of thermodynamics.

Furthermore, by substituting the specific balance relations from (2.53) into the local master balances given in (2.52), we derive the standard local balance equations for single-phase

materials and the aggregate φ

$$\begin{aligned}
\text{mass}: &\quad \dot{\rho} + \rho \operatorname{div} \dot{\mathbf{x}} = 0, \\
\text{momentum}: &\quad \rho \ddot{\mathbf{x}} = \operatorname{div} \mathbf{T} + \rho \mathbf{b}, \\
\text{ang. momentum}: &\quad \mathbf{0} = \mathbf{I} \times \mathbf{T} \quad \rightarrow \quad \mathbf{T} = \mathbf{T}^{\mathrm{T}}, \\
\text{energy}: &\quad \rho \dot{\varepsilon} = \mathbf{T} : \mathbf{L} - \operatorname{div} \mathbf{q} + \rho r, \\
\text{entropy}: &\quad \rho \dot{\eta} \geq \operatorname{div} \boldsymbol{\phi}_{\eta} + \sigma_{\eta},
\end{aligned} \tag{2.54}$$

which are consistent with Truesdell's third metaphysical principle. It is important to note that as a consequence of the angular momentum balance, we obtain a symmetric Cauchy stress tensor $\mathbf{T}$.

2.3.2 Constituent balance relations

In accordance with Truesdell's second metaphysical principle, the master balance relations for the constituents φ^{α} can be derived analogously to the general master balance equations. Specifically, these balance relations are expressed as

$$\begin{aligned}
\frac{\mathrm{d}_{\alpha}}{\mathrm{d}t} \int_{\mathcal{B}} \Psi^{\alpha} \, \mathrm{d}v &= \int_{\mathcal{S}} (\boldsymbol{\phi}^{\alpha} \cdot \mathbf{n}) \, \mathrm{d}a + \int_{\mathcal{B}} \sigma^{\alpha} \, \mathrm{d}v + \int_{\mathcal{B}} \hat{\Psi}^{\alpha} \, \mathrm{d}v, \\
\frac{\mathrm{d}_{\alpha}}{\mathrm{d}t} \int_{\mathcal{B}} \boldsymbol{\Psi}^{\alpha} \, \mathrm{d}v &= \int_{\mathcal{S}} (\boldsymbol{\Phi}^{\alpha} \mathbf{n}) \, \mathrm{d}a + \int_{\mathcal{B}} \boldsymbol{\sigma}^{\alpha} \, \mathrm{d}v + \int_{\mathcal{B}} \hat{\boldsymbol{\Psi}}^{\alpha} \, \mathrm{d}v.
\end{aligned} \tag{2.55}$$

Here, the partial quantities $(\cdot)^{\alpha}$ retain the same physical significance as introduced in the generalized balance equations for single-phase systems. Following this, the local master balance relations for the individual constituents take a similar form

$$\begin{aligned}
(\Psi^{\alpha})'_{\alpha} + \Psi^{\alpha} \operatorname{div} \mathbf{x}'_{\alpha} &= \operatorname{div} \boldsymbol{\phi}^{\alpha} + \sigma^{\alpha} + \hat{\Psi}^{\alpha}, \\
(\boldsymbol{\Psi}^{\alpha})'_{\alpha} + \boldsymbol{\Psi}^{\alpha} \operatorname{div} \mathbf{x}'_{\alpha} &= \operatorname{div} \boldsymbol{\Phi}^{\alpha} + \boldsymbol{\sigma}^{\alpha} + \hat{\boldsymbol{\Psi}}^{\alpha}.
\end{aligned} \tag{2.56}$$

When summing these relations over all constituents φ^{α}, in line with Truesdell's first principle [44, 125], the aggregate system's master balance can be deduced. This aggregation leads to the following constraints for scalar and vector-valued quantities, such as Ψ and $\boldsymbol{\Psi}$

	Scalar-value	Vector-value
physical quantity	$\Psi = \sum_\alpha \Psi^\alpha$	$\boldsymbol{\Psi} = \sum_\alpha \boldsymbol{\Psi}^\alpha$
efflux	$\boldsymbol{\phi} \cdot \mathbf{n} = \sum_\alpha (\boldsymbol{\phi}^\alpha - \Psi^\alpha \mathbf{v}_\alpha) \cdot \mathbf{n}$	$\boldsymbol{\Phi}\mathbf{n} = \sum_\alpha (\boldsymbol{\Phi}^\alpha - \boldsymbol{\Psi}^\alpha \otimes \mathbf{v}_\alpha)\mathbf{n}$
supply	$\sigma = \sum_\alpha \sigma^\alpha$	$\boldsymbol{\sigma} = \sum_\alpha \boldsymbol{\sigma}^\alpha$
production	$\hat{\Psi} = \sum_\alpha \hat{\Psi}^\alpha$	$\hat{\boldsymbol{\Psi}} = \sum_\alpha \hat{\boldsymbol{\Psi}}^\alpha$

(2.57)

Upon analyzing the divergence terms in these relations, an additional diffusion velocity term arises, as indicated in the second summation constraint [15, 101]. The specific balance equations for each constituent, analogous to single-phase materials are

	$\Psi^\alpha, \boldsymbol{\Psi}^\alpha$	$\boldsymbol{\phi}^\alpha, \boldsymbol{\Phi}^\alpha$	$\sigma^\alpha, \boldsymbol{\sigma}^\alpha$	$\hat{\Psi}^\alpha, \hat{\boldsymbol{\Psi}}^\alpha$
mass	ρ^α	$\mathbf{0}$	0	$\hat{\rho}^\alpha$
momentum	$\rho^\alpha \mathbf{x}'_\alpha$	$\mathbf{T}^\alpha$	$\rho^\alpha \mathbf{b}^\alpha$	$\hat{\mathbf{s}}^\alpha$
ang. momentum	$\mathbf{x} \times (\rho^\alpha \mathbf{x}'_\alpha)$	$\mathbf{x} \times \mathbf{T}^\alpha$	$\mathbf{x} \times (\rho^\alpha \mathbf{b}^\alpha)$	$\hat{\mathbf{h}}^\alpha$
energy	$\rho^\alpha \varepsilon^\alpha + \frac{1}{2}\mathbf{x}'_\alpha \cdot (\rho^\alpha \mathbf{x}'_\alpha)$	$(\mathbf{T}^\alpha)^T \mathbf{x}'_\alpha - \mathbf{q}^\alpha$	$\mathbf{x}'_\alpha \cdot (\rho^\alpha \mathbf{b}^\alpha) + \rho^\alpha r^\alpha$	$\hat{e}^\alpha$
entropy	$\rho^\alpha \eta^\alpha$	$\boldsymbol{\phi}^\alpha_\eta$	σ^α_η	$\hat{\eta}^\alpha$

The total production terms split into direct and additional terms are shown in Table 2.1 [69, 73]. Summing the constituent-specific balance relations and incorporating the summation

total production	=	direct production	+	additional terms
$\hat{\mathbf{s}}^\alpha$	=	$\hat{\mathbf{p}}^\alpha$	+	$\hat{\rho}^\alpha \mathbf{x}'_\alpha$
$\hat{\mathbf{h}}^\alpha$	=	$\hat{\mathbf{m}}^\alpha$	+	$\mathbf{x} \times (\hat{\mathbf{p}}^\alpha + \hat{\rho}^\alpha \mathbf{x}'_\alpha)$
$\hat{e}^\alpha$	=	$\hat{\epsilon}^\alpha$	+	$\hat{\mathbf{p}}^\alpha \cdot \mathbf{x}'_\alpha + \hat{\rho}^\alpha (\epsilon + \frac{1}{2}\mathbf{x}'_\alpha \cdot \mathbf{x}'_\alpha)$
$\hat{\eta}^\alpha$	=	$\hat{\zeta}^\alpha$	+	$\hat{\rho}^\alpha \eta^\alpha$

Table 2.1: Production terms in balance relations.

constraints results in the following zero-sum conditions for mass, momentum, energy, and entropy production

$$\sum_{\alpha} \hat{\rho}^{\alpha} = 0, \quad \sum_{\alpha} \hat{\mathbf{s}}^{\alpha} = \mathbf{0}, \quad \sum_{\alpha} \hat{\mathbf{h}}^{\alpha} = \mathbf{0}, \quad \sum_{\alpha} \hat{e}^{\alpha} = 0, \quad \sum_{\alpha} \hat{\eta}^{\alpha} \geq 0. \tag{2.58}$$

The efflux and supply of entropy for each constituent φ^{α} are related to the thermal flux and internal energy source terms

$$\boldsymbol{\phi}_{\eta}^{\alpha} = \frac{1}{\Theta^{\alpha}} \mathbf{q}^{\alpha}, \quad \sigma_{\eta}^{\alpha} = \frac{1}{\Theta^{\alpha}} \rho^{\alpha} r^{\alpha}, \tag{2.59}$$

where Θ^{α} is the temperature specific to each constituent. By utilizing these relations in the master constituent balance equations and applying hierarchical balance derivations, the following specific forms for non-polar constituents are obtained

$$\begin{aligned}
\text{mass}: &\quad (\rho^{\alpha})'_{\alpha} + \rho^{\alpha} \operatorname{div} \mathbf{x}'_{\alpha} = \hat{\rho}^{\alpha}, \\
\text{momentum}: &\quad \rho^{\alpha} \mathbf{x}''_{\alpha} = \operatorname{div} \mathbf{T}^{\alpha} + \rho^{\alpha} \mathbf{b}^{\alpha} + \hat{\mathbf{p}}^{\alpha}, \\
\text{ang. momentum}: &\quad \mathbf{0} = \mathbf{I} \times \mathbf{T}^{\alpha}, \\
\text{energy}: &\quad \rho^{\alpha} (\varepsilon^{\alpha})'_{\alpha} = \mathbf{T}^{\alpha} : \mathbf{L}_{\alpha} - \operatorname{div} \mathbf{q}^{\alpha} + \rho^{\alpha} r^{\alpha} + \hat{\varepsilon}^{\alpha}, \\
\text{entropy}: &\quad \rho^{\alpha} (\eta^{\alpha})'_{\alpha} = \operatorname{div} \left(-\frac{1}{\Theta^{\alpha}} \mathbf{q}^{\alpha} \right) + \frac{1}{\Theta^{\alpha}} \rho^{\alpha} r^{\alpha} + \hat{\zeta}^{\alpha}.
\end{aligned} \tag{2.60}$$

2.3.3 Entropy principle

In thermodynamic processes, the first law of thermodynamics governs energy conservation, defining how energy is transferred within a system. However, this law does not provide information regarding the direction of energy transfer. The second law of thermodynamics, together with the entropy balance, addresses this by governing the direction of energy transfer, forming the basis for the *entropy principle*. This principle imposes crucial restrictions that play a significant role in the constitutive modeling of materials.

The entropy principle can be formulated by constraining the total entropy production, as outlined in (2.58) and in relation to Table 2.1. By applying the specific entropy balance for each individual constituent, as expressed in (2.60), we derive the following inequality for the total entropy production

$$\hat{\eta} = \sum_{\alpha} \hat{\eta}^{\alpha} = \sum_{\alpha} \left[\rho^{\alpha} (\eta^{\alpha})'_{\alpha} + \hat{\rho}^{\alpha} \eta^{\alpha} + \operatorname{div} \left(\frac{1}{\Theta^{\alpha}} \mathbf{q}^{\alpha} \right) - \frac{1}{\Theta^{\alpha}} \rho^{\alpha} r^{\alpha} \right] \geq 0. \tag{2.61}$$

In this context, we assume that each constituent within the medium is in a state of local thermodynamic equilibrium. For materials like concrete, it is reasonable to neglect all internal heat sources $\rho^{\alpha} r^{\alpha}$ that are unrelated to the primary mass exchange processes,

specifically evaporation and hydration [63, 125]. To advance our formulation, we utilize a Legendre transformation to shift from entropy to its conjugate variable, temperature, thereby introducing the Helmholtz free energy function

$$\psi^\alpha := \varepsilon^\alpha - \Theta^\alpha \eta^\alpha. \tag{2.62}$$

This transformation allows us to reframe the energy potential, facilitating the derivation of thermodynamically consistent constitutive equations for each constituent by combining this definition with the lower balance relations for the constituents from (2.60). We derive the Clausius-Duhem form of the entropy inequality, a fundamental equation for ensuring thermodynamic consistency in the modeling framework

$$\begin{aligned} \mathcal{D} = \sum_\alpha \frac{1}{\Theta^\alpha} \Big\{ \mathbf{T}^\alpha : \mathbf{L}_\alpha - \rho^\alpha \left[(\psi^\alpha)'_\alpha + (\Theta^\alpha)'_\alpha \eta^\alpha \right] - \hat{\mathbf{p}}^\alpha \cdot \mathbf{x}'_\alpha \\ - \hat{\rho}^\alpha \left(\psi^\alpha + \frac{1}{2} \mathbf{x}'_\alpha \cdot \mathbf{x}'_\alpha \right) - \frac{1}{\Theta^\alpha} \mathbf{q}^\alpha \cdot \operatorname{grad} \Theta^\alpha + \hat{e}^\alpha \Big\} \geq 0. \end{aligned} \tag{2.63}$$

3 MODELL ASSUMPTIONS

In constitutive modeling within continuum mechanics, developing an adequate set of constitutive equations is essential for accurately describing the material behavior and closing the system of equations set forth by kinematic and balance relations. In Chapter 2, we introduced the fundamentals of kinematics and the balance equations, which provide the necessary framework for modeling motion and forces in a continuum. However, these equations alone are insufficient to fully characterize the behavior of the material, as they lack the necessary specificity to determine all unknown quantities uniquely. Consequently, additional constitutive equations must be formulated, grounded in the physical characteristics of the material and any relevant assumptions that simplify the problem while preserving essential thermodynamic and mechanical consistency.

To achieve a thermodynamically consistent constitutive model, we explore the entropy inequality to impose necessary constraints on the form of these equations. In this chapter, we also examine the specific properties and assumptions relevant to our study of fresh concrete, aiming to adapt the general framework of continuum mechanics to a multiphase porous media context. This includes simplifications to the balance equations tailored to the distinct interactions within a concrete environment, particularly in modeling the behavior of multiple interacting constituents, such as solids and fluids. By adhering to thermodynamic restrictions, as demonstrated in works on multiphase systems by Schrefler [125] and Ehlers [44], we ensure that our developed constitutive relations align with physical principles and provide a reliable foundation for simulating fresh concrete maturing.

3.1 Triphasic model for fresh concrete

The solid skeleton is the primary component of partially saturated concrete, denoted as the solid phase $\alpha = S$, with the solid particles assumed to be materially incompressible. The pore spaces within this solid structure are occupied by two distinct fluid phases: compressible pore air, represented as $\alpha = G$, and incompressible pore water, described as $\alpha = L$. This model effectively captures fresh concrete's essential characteristics by distinguishing each constituent's material compressibility and addressing their respective roles within the overall aggregate.

3.1.1 Preliminaries and assumptions

To align the model with the underlying theoretical framework, we establish a set of fundamental assumptions. These assumptions serve to streamline the complex interactions

within the triphasic aggregate φ and its constituents φ^α, thereby enhancing both the tractability and robustness of the model.

- **Saturation condition** The aggregate is assumed to be fully saturated, preventing any void spaces within the overall structure

$$n^S + n^L + n^G = 1. \tag{3.1}$$

- **Material incompressibility** In this model, all material densities are assumed to be temperature dependent. The solid particles are treated as materially incompressible, whereas the solid skeleton is considered materially compressible. The pore water is likewise assumed to be materially incompressible. In contrast, the gas constituent is materially compressible, with its density dependent on both temperature and pressure

$$\rho^{SR} = \rho^{SR}(\Theta), \qquad \rho^{LR} = \rho^{LR}(\Theta), \qquad \rho^{GR} = \rho^{GR}(\Theta, p^G). \tag{3.2}$$

- **Quasi-static conditions:** The model assumes slow deformations, rendering acceleration effects negligible

$$\mathbf{x}''_\alpha \equiv \mathbf{0}, \quad \ddot{\mathbf{x}} \equiv \mathbf{0}. \tag{3.3}$$

- **Thermal conditions:** The temperature of all constituents is assumed to be the same

$$\Theta^\alpha \equiv \Theta. \tag{3.4}$$

- **Uniform body force:** A consistent body force acts on all constituents φ^α, simplifying the influence of external forces

$$\mathbf{b}^S = \mathbf{b}^L = \mathbf{b}^G = \mathbf{b}. \tag{3.5}$$

- **Stress symmetry:** Each constituent is assumed non-polar, resulting in a symmetric stress tensor

$$\mathbf{T}^\alpha = (\mathbf{T}^\alpha)^T. \tag{3.6}$$

3.1.2 Balance of mass

The mass balance for each constituent is established by starting from the local mass balance relation given in equation (2.60), applied to all three phases

$$(\rho^S)'_S + \rho^S \operatorname{div} \mathbf{x}'_S = \hat{\rho}^S, \tag{3.7a}$$

$$(\rho^L)'_L + \rho^L \operatorname{div} \mathbf{x}'_L = \hat{\rho}^L, \tag{3.7b}$$

$$(\rho^G)'_G + \rho^G \operatorname{div} \mathbf{x}'_G = \hat{\rho}^G. \tag{3.7c}$$

Furthermore, we formulate these expressions using material time derivatives taken with respect to the solid skeleton. To relate the changes observed in the fluid phases to the motion of the solid, we employ the following identities for the material time derivative of a scalar field γ, which incorporate the relative (seepage) velocities between the phases

$$\left.\begin{aligned} {\gamma_S}' &= \frac{\partial \gamma}{\partial t} + \operatorname{grad}\gamma \cdot \mathbf{x}'_S, \\ {\gamma_L}' &= \frac{\partial \gamma}{\partial t} + \operatorname{grad}\gamma \cdot \mathbf{x}'_L, \\ {\gamma_G}' &= \frac{\partial \gamma}{\partial t} + \operatorname{grad}\gamma \cdot \mathbf{x}'_G, \end{aligned}\right\} \Rightarrow \quad \begin{aligned} {\gamma_L}' &= {\gamma_S}' + \operatorname{grad}\gamma \cdot (\mathbf{x}'_L - \mathbf{x}'_S) = {\gamma_S}' + \operatorname{grad}\gamma \cdot \mathbf{w}_{LS}, \\ {\gamma_G}' &= {\gamma_S}' + \operatorname{grad}\gamma \cdot (\mathbf{x}'_G - \mathbf{x}'_S) = {\gamma_S}' + \operatorname{grad}\gamma \cdot \mathbf{w}_{GS}. \end{aligned} \tag{3.8}$$

By applying the incompressibility assumption from subsection 3.1.1, together with the density expression in (2.7) and the production relations from subsection 2.3.2, the strong form of the mass balance equations for the solid, liquid, and gas constituents, formulated in the reference frame of the solid skeleton, can be expressed as

$$n^S \left(\rho^{SR}\right)'_S + \rho^{SR} \left(n^S\right)'_S + n^S \rho^{SR} \operatorname{div}\left(\mathbf{x}'_S\right) = \hat{\rho}^S, \tag{3.9a}$$

$$n^L \left(\rho^{LR}\right)'_S + \rho^{LR} \left(n^L\right)'_S + n^L \rho^{LR} \operatorname{div}\left(\mathbf{x}'_S\right) + \operatorname{div}\left(n^L \rho^{LR} \mathbf{w}_{LS}\right) = \hat{\rho}^L, \tag{3.9b}$$

$$n^G \left(\rho^{GR}\right)'_S + \rho^{GR} \left(n^G\right)'_S + n^G \rho^{GR} \operatorname{div}\left(\mathbf{x}'_S\right) + \operatorname{div}\left(n^G \rho^{GR} \mathbf{w}_{GS}\right) = \hat{\rho}^G. \tag{3.9c}$$

3.1.3 Balance of linear momentum

Under the assumption of quasi-static conditions, which permit neglecting acceleration terms, the linear momentum balance for each constituent φ^α, as given in equation (2.60), simplifies to

$$\operatorname{div} \mathbf{T}^S + \rho^S \mathbf{b} + \hat{\mathbf{p}}^S = \mathbf{0}, \tag{3.10a}$$

$$\operatorname{div} \mathbf{T}^L + \rho^L \mathbf{b} + \hat{\mathbf{p}}^L = \mathbf{0}, \tag{3.10b}$$

$$\operatorname{div} \mathbf{T}^G + \rho^G \mathbf{b} + \hat{\mathbf{p}}^G = \mathbf{0}. \tag{3.10c}$$

with corresponding Cauchy stress tensors $\mathbf{T}^\alpha$. Applying the summation constraint for the total momentum production of the mixture, along with the mass production constraint and constituent interactions specified in Table 2.1, we obtain

$$\sum_\alpha \hat{\mathbf{p}}^\alpha = \sum_\alpha \left(\hat{\mathbf{s}}^\alpha - \hat{\rho}^\alpha \mathbf{x}'_\alpha\right) = 0, \tag{3.11}$$

where $\hat{\mathbf{s}}^{\alpha}$ represents interaction forces between the constituents. Due to the slow processes associated with constituent interactions, the term $\hat{\rho}^{\alpha}\mathbf{x}'_{\alpha}$ can be considered negligible, allowing us to simplify the momentum production summation to zero. By summing the individual momentum balance equations for all constituents in (3.10), we get the overall momentum balance for the mixture

$$\operatorname{div}(\mathbf{T}^{S}+\mathbf{T}^{L}+\mathbf{T}^{G})+(\rho^{S}+\rho^{L}+\rho^{G})\mathbf{b}=\mathbf{0}. \tag{3.12}$$

This equation describes the combined momentum balance for the entire mixture, where the total stress tensor is the sum of the stresses from each phase, and the total body force is the cumulative body force acting on all constituents.

3.1.4 Balance of energy

In thermodynamic systems, energy conservation can be expressed through two primary potentials: internal energy and enthalpy. To begin with, we formulate the energy conservation equation in terms of the internal energy of each constituent, as this form directly aligns with fundamental thermodynamic principles. However, in practical applications, particularly when analyzing experimental data, it is often more convenient to work with enthalpy, another thermodynamic potential incorporating pressure-volume work.

The general form of the energy balance for each constituent φ^{α} is provided in equation (2.60). Assuming that mass exchange within the multiphasic medium occurs slowly and that additional heat sources unrelated to the primary mass exchange processes are negligible, the energy balance can be simplified

$$\rho^{\alpha}(\epsilon^{\alpha})' = \mathbf{T}^{\alpha}:\mathbf{L}_{\alpha}-\operatorname{div}\mathbf{q}^{\alpha}+\hat{e}^{\alpha}-\hat{\rho}^{\alpha}\epsilon^{\alpha}. \tag{3.13}$$

To relate this to enthalpy, we apply a Legendre transformation

$$\epsilon^{\alpha}=h^{\alpha}-\frac{p^{\alpha}}{\rho^{\alpha}}, \tag{3.14}$$

where h^{α} is the enthalpy and p^{α} is the pressure of constituent φ^{α}. Substituting this expression for internal energy, we derive the enthalpy balance for the mixture

$$\sum_{\alpha}\left(\rho^{\alpha}(h^{\alpha})'-(p^{\alpha})'+\frac{p^{\alpha}}{\rho^{\alpha}}(\rho^{\alpha})'\right)=\sum_{\alpha}\mathbf{T}^{\alpha}:\mathbf{L}_{\alpha}-\sum_{\alpha}\operatorname{div}\mathbf{q}^{\alpha}-\sum_{\alpha}\hat{\rho}^{\alpha}h^{\alpha}+\sum_{\alpha}\frac{p^{\alpha}}{\rho^{\alpha}}\hat{\rho}^{\alpha}. \tag{3.15}$$

Using the mass balance relation in (2.60), the enthalpy equation simplifies further to

$$\sum_{\alpha}\left(\rho^{\alpha}(h^{\alpha})'-(p^{\alpha})'\right)=\sum_{\alpha}\mathbf{T}^{\alpha}:\mathbf{L}_{\alpha}-\sum_{\alpha}\operatorname{div}\mathbf{q}^{\alpha}-\sum_{\alpha}\hat{\rho}^{\alpha}h^{\alpha}+\sum_{\alpha}p^{\alpha}\operatorname{div}\mathbf{x}'_{\alpha}. \tag{3.16}$$

In the following sections, we provide clear definitions of pressure, stress, and other essential thermomechanical relations. These definitions enable a systematic simplification of the enthalpy equation for the mixture, ultimately leading to its final form. The detailed steps of these simplifications are presented in section A.1.

3.1.5 Entropy inequality

The Clausius-Duhem inequality, as formulated in equation (2.63) and incorporating the symmetry of partial stresses from (3.6), provides the foundational expression for entropy production in a multiphasic system

$$\begin{aligned}\mathcal{D} = \sum_{\alpha} \frac{1}{\Theta^{\alpha}} \Big\{ \mathbf{T}^{\alpha} : \mathbf{L}_{\alpha} - \rho^{\alpha} \left[(\psi^{\alpha})'_{\alpha} + (\Theta^{\alpha})'_{\alpha} \eta^{\alpha} \right] - \hat{\mathbf{p}}^{\alpha} \cdot \mathbf{x}'_{\alpha} - \\ - \hat{\rho}^{\alpha} \left(\psi^{\alpha} + \frac{1}{2} \mathbf{x}'_{\alpha} \cdot \mathbf{x}'_{\alpha} \right) - \frac{1}{\Theta^{\alpha}} \mathbf{q}^{\alpha} \cdot \operatorname{grad} \Theta^{\alpha} + \hat{e}^{\alpha} \Big\} \geq 0.\end{aligned} \tag{3.17}$$

Assuming a slow process and zero total energy production (as indicated by (2.58)), the Clausius-Duhem inequality simplifies to a localized dissipation condition. This reduction results in the Clausius-Planck inequality in its localized form

$$\mathcal{D} = \sum_{\alpha} \frac{1}{\Theta^{\alpha}} \Big\{ \mathbf{T}^{\alpha} : \mathbf{L}_{\alpha} - \rho^{\alpha} \left[(\psi^{\alpha})'_{\alpha} + (\Theta^{\alpha})'_{\alpha} \eta^{\alpha} \right] - \hat{\rho}^{\alpha} \psi^{\alpha} - \frac{1}{\Theta^{\alpha}} \mathbf{q}^{\alpha} \cdot \operatorname{grad} \Theta^{\alpha} \Big\} \geq 0. \tag{3.18}$$

This localized form of the entropy inequality establishes necessary constraints on the constitutive behavior of each constituent in the mixture, ensuring compliance with the second law of thermodynamics and guaranteeing non-negative entropy production across the system.

3.2 Thermodynamic principles

With the adapted balance relations established, we proceed to define the constitutive relations of the material behavior. To ensure a thermodynamically consistent model, these constitutive relations must adhere strictly to fundamental principles. Therefore, we briefly review the foundational principles of determinism, local action, equipresence, material frame indifference, and universal dissipation, as outlined in the works of Coleman & Noll [25], Noll [108, 109], Truesdell [137] and Ehlers [47].

3.2.1 Determinism, equipresence, and local action

Building upon the governing equations, the initial state of each constituent must be defined through the following conditions

$$\mathbf{x} = \chi_\alpha(p^\alpha, t_0), \quad \rho^{\alpha R}(t_0) \quad \text{and} \quad n^\alpha(t_0), \tag{3.19}$$

along with the total state of motion and temperature

$$\begin{aligned} \mathbf{x} = \chi_\alpha(\mathbf{X}_\alpha, t) \longrightarrow \begin{cases} \mathbf{F}_\alpha & \longrightarrow \det \mathbf{F}_\alpha, \\ \mathbf{x}'_\alpha & \longrightarrow \begin{cases} \operatorname{div} \mathbf{x}'_\alpha \\ \mathbf{L}_\alpha \end{cases} \\ \mathbf{x}''_\alpha \end{cases} \\ \Theta^\alpha = \Theta^\alpha(\mathbf{x}, t) \longrightarrow \begin{cases} \operatorname{grad} \Theta^\alpha, \\ (\Theta^\alpha)'_\alpha, \end{cases} \end{aligned} \tag{3.20}$$

are assumed as given fields. Consequently, constitutive relations must be formulated for all quantities that cannot be directly computed from the balance relations, given the initial conditions and the total state of motion and temperature [69]. In the most general case, these constitutive relations can be expressed in terms of the complete set of fundamental variables, as defined by Ehlers [47]

$$\begin{aligned} \mathcal{V}(\mathbf{x}, t) := \big\{ \Theta^\alpha,\ \operatorname{grad} \Theta^\alpha,\ n^\alpha,\ \operatorname{grad} n^\alpha,\ \rho^{\alpha R},\ \operatorname{grad} \rho^{\alpha R},\ \mathbf{F}_\alpha,\ \operatorname{Grad}_\alpha \mathbf{F}_\alpha, \\ \mathbf{x}'_\alpha,\ \operatorname{Grad}_\alpha \mathbf{x}'_\alpha,\ \mathbf{X}_\alpha \big\}. \end{aligned} \tag{3.21}$$

In this context, the thermal state of the material is fully described by the temperature, which is assumed to be identical for all three constituents, along with its gradient, which drives heat transport within the system. Unlike single-phase, non-porous materials, where mass production is not a factor, mass production can occur in multiphasic porous media. Therefore, the partial density $\rho^\alpha = n^\alpha \rho^{\alpha R}$ cannot be determined solely by integrating the mass balance. As a result, the volume fraction n^α, the material density $\rho^{\alpha R}$ and their gradients must be considered independent fields to accurately describe the deformation of each constituent, whether solid or fluid [47].

Furthermore, since porous materials are classified as second-order materials [47], both the first (material) deformation gradient $\mathbf{F}_\alpha$ and the second deformation gradient $\operatorname{Grad}_\alpha \mathbf{F}_\alpha$ are included in (3.21). Viscosity effects are represented by $\mathbf{x}'_\alpha$ and $\operatorname{Grad}_\alpha \mathbf{x}'_\alpha$, while the

position in the reference configuration, $\mathbf{X}_\alpha$, accounts for inhomogeneities within individual constituents. For an in-depth exploration of this subject, readers are directed to the foundational work of Ehlers on elasto-plastic materials [39, 40, 41, 42]. Additionally, for insights into the modeling of viscoelastic materials, the contributions by Ehlers and Markert provide a comprehensive study [48, 49].

Based on this fundamental set of constitutive variables, constitutive relations are required for the following set of response functions

$$\{\psi^\alpha,\ \eta^\alpha,\ \mathbf{q}^\alpha,\ \hat{\epsilon}^\alpha,\ \mathbf{T}^\alpha,\ \hat{\mathbf{p}}^\alpha,\ \hat{\rho}^\alpha\} = \mathcal{R}\left[\mathcal{V}(x,t)\right], \tag{3.22}$$

where $\mathcal{R}$ denotes the response functions set. Here, both the solid and liquid particles are considered materially incompressible. However, this incompressibility applies exclusively to their mechanical behavior. Individual particles within the solid and liquid phases are allowed to undergo thermal expansion, depending on temperature Θ. In contrast, the gaseous phase, which is a materially compressible fluid constituent, is modeled as an ideal gas.

This general set $\mathcal{V}$ of constitutive variables can be reduced to a more specific set $\mathcal{S}$ by incorporating the characteristic material properties of the individual constituents. To begin, the constitutive variables associated with the solid skeleton are examined in greater detail, following the argumentation presented by Ghadiani [68]. For simplification, it is assumed that the solid skeleton exhibits purely elastic material behavior. Since the multiphasic material is analyzed under non-isothermal conditions, the deformation gradient $\mathbf{F}_S$ of the solid matrix is retained as a variable.

According to the principle of material frame indifference, the various velocities $\mathbf{x}'_\alpha$ of the constituents should be replaced by the seepage velocities $\mathbf{w}_{\beta S}$, where β denotes each fluid phase. Additionally, the term $\mathrm{Grad}_\alpha\, \mathbf{x}'_\alpha$, which captures viscous material properties, is substituted by the symmetric part of the rate-of-deformation tensor, $\mathbf{D}_\alpha$. For the solid skeleton, where fluid viscosity is not applicable, $\mathbf{D}_S$ can be omitted from the set of constitutive variables $\mathcal{V}$. The volume fraction n^S of the solid matrix, together with the saturation condition (2.5), allows the computation of the porosity n^F of the entire porous medium. Consequently, the volume fractions of the fluid phases can be directly determined by their respective saturation levels, denoted as s^β. Additionally, Cross [27] demonstrated that deformation variables are not influenced by mass production. This finding permits the substitution of $\det\mathbf{F}_\beta$ with $\rho^{\beta R}$ and n^β, thereby enabling the removal of $\mathbf{F}_\beta$ and $\mathrm{Grad}_\beta\, \mathbf{F}_\beta$ from the set of constitutive variables $\mathcal{V}$ [4, 69, 73].

For the pore liquid, as with the solid phase, it is assumed that the material densities ρ^{LR} and ρ^{SR} depend solely on their respective temperatures. Consequently, these densities and their gradients can also be excluded from the set of constitutive variables $\mathcal{V}$. Finally, assuming that all constituents are homogeneous materials, the position in the reference configuration $\mathbf{X}_\alpha$ can be removed from $\mathcal{V}$ as well. Bowen [17] asserts that the second-grade nature of the material model applies exclusively to the production terms, thereby allowing the removal

of $\mathrm{Grad}_S \mathbf{F}_S$ from the dependencies. Thus, the simplified set $\mathcal{S}$ of constitutive variables for the material model under consideration is defined

$$\mathcal{S} := \left\{\Theta,\ \mathrm{grad}\,\Theta,\ n^\alpha,\ \mathrm{grad}\,n^\alpha,\ \rho^{GR},\ \mathrm{grad}\,\rho^{GR},\ \mathbf{F}_S,\ \mathbf{w}_{\beta S},\ \mathbf{D}_\beta,\ J_\alpha\right\}. \tag{3.23}$$

According to the principle of equipresence, the response functions, grouped in $\mathcal{R}$, are considered to be functions of the constitutive variables included in the set $\mathcal{S}$, as discussed by Ehlers [47]. Thus, we have

$$\mathcal{R} := \mathcal{R}(\mathcal{S}). \tag{3.24}$$

Furthermore, the evaluation of the entropy inequality follows the approach outlined by Ehlers [47] and references therein, including de Boer & Ehlers [36], Bowen [16], and Coleman & Noll [25]. Ehlers introduced the principle of phase separation, which states that the free energy function ψ^α for a specific constituent φ^α should depend only on the non-dissipative process variables relevant to that constituent. This means that variables related to dissipation, such as velocities, are excluded from the free energy function. According to the principle of local action, the constitutive response at a given point can be described using first-grade, second-grade, or higher-order theories.

To keep the model at a reasonable level of complexity, we select the following dependencies for the Helmholtz free energy functions ψ^α

$$\psi^S = \psi^S(\Theta, \mathbf{F}_S, n^S), \qquad \psi^L = \psi^L(\Theta, s^L), \qquad \psi^G = \psi^G(\Theta, \rho^{GR}), \tag{3.25}$$

where ψ^S, ψ^L, and ψ^G correspond to the free energy functions of the solid, liquid, and gas phases, respectively. This selection simplifies the model while ensuring compliance with the principles of thermodynamic consistency for multiphase materials. For a comprehensive exploration of these concepts, see the foundational work of Bowen [18].

3.2.2 Material frame indifference

The principle of material frame indifference, or objectivity, is fundamental to nonlinear continuum mechanics, ensuring that material properties and constitutive equations are invariant under rigid body motions. This implies that material responses do not depend on the observer's position or any superimposed rigid body motion. We denote $\overset{+}{\chi}_\alpha$ as the rigid body motion function and $\overset{*}{\chi}_\alpha$ as the superimposed rigid body motion

$$\overset{+}{\mathbf{x}} = \overset{+}{\chi}_\alpha(\mathbf{x},t) = \mathbf{c}(t) + \mathbf{Q}(t)\mathbf{x}, \qquad \overset{*}{\chi}_\alpha = \overset{+}{\chi}_\alpha \circ \chi_\alpha, \tag{3.26}$$

with $\mathbf{c}$ as the rigid translation vector and $\mathbf{Q}$ as a proper orthogonal rotation tensor satisfying $\det\mathbf{Q} = +1$ and $\mathbf{Q}^{-1} = \mathbf{Q}^T$. The transformation of a spatial vector under rigid motion is

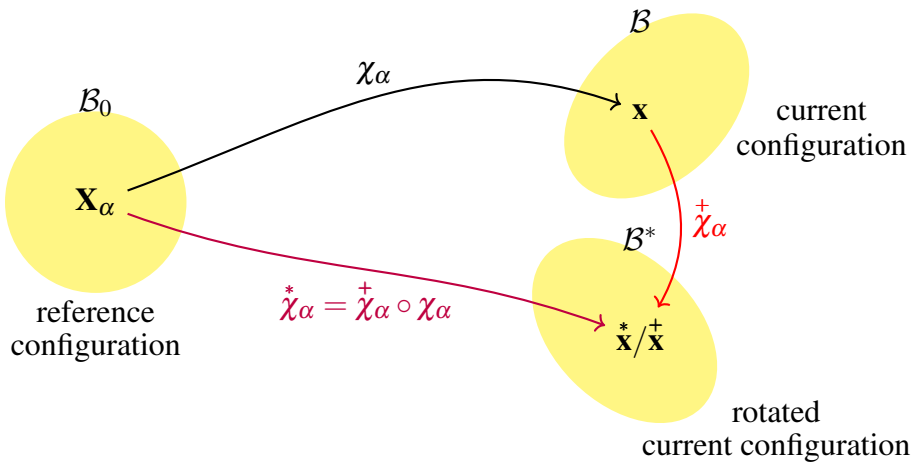

Figure 3.1: Principle of material frame indifference.

given by

$$\overset{+}{\mathbf{u}} = \mathbf{Q}(t)\mathbf{u}, \tag{3.27}$$

where $\mathbf{u}$ and $\overset{+}{\mathbf{u}}$ represent the displacement vectors in the current and rotated configurations, respectively. Differentiating equation (3.26) gives the relation for rotated line elements

$$\frac{\partial \overset{+}{\mathbf{x}}}{\partial \mathbf{x}} = \mathbf{Q}. \tag{3.28}$$

Using this, we establish that the deformation gradient transforms to

$$\overset{*}{\mathbf{F}}_\alpha = \mathbf{Q}\mathbf{F}_\alpha. \tag{3.29}$$

This relation extends to the volume element $\mathrm{d}v$ and volume fractions n^α, showing that they remain invariant under rigid body motion

$$\mathrm{d}\overset{*}{v} = \overset{*}{J}_\alpha \mathrm{d}V_\alpha = \det\overset{*}{\mathbf{F}}_\alpha \mathrm{d}V_\alpha = (\det\mathbf{Q})(\det\mathbf{F}_\alpha)\mathrm{d}V_\alpha = J_\alpha \mathrm{d}V_\alpha = \mathrm{d}v, \tag{3.30}$$

To ensure the solid Helmholtz free energy function ψ^S adheres to the principle of material frame indifference, we must confirm its objectivity. For scalar quantities, objectivity implies that $\overset{*}{\psi}(\overset{*}{\cdot}) = \psi(\cdot)$, meaning that ψ^S is unaffected by rigid body motions. This can be written as

$$\overset{*}{\psi}{}^S(\overset{*}{\Theta}, \overset{*}{\mathbf{F}}_S, \overset{*}{n}{}^S) = \psi^S(\Theta, \mathbf{F}_S, n^S), \quad \Rightarrow \quad \psi^S(\Theta, \mathbf{Q}\mathbf{F}_S, n^S) = \psi^S(\Theta, \mathbf{F}_S, n^S). \tag{3.31}$$

This expression indicates that ψ^S cannot be an arbitrary function of $\mathbf{F}_S$. By using the orthogonal rotation tensor's transpose, $\mathbf{R}_S^T = \mathbf{Q}$, and the right polar decomposition of $\mathbf{F}_S$ (cf. Section 2.2.3), we find

$$\psi^S(\Theta, \mathbf{F}_S, n^S) = \psi^S(\Theta, \mathbf{R}_S\mathbf{F}_S, n^S) = \psi^S(\Theta, \mathbf{R}^T\mathbf{R}\mathbf{U}_S, n^S) = \psi^S(\Theta, \mathbf{U}_S, n^S). \tag{3.32}$$

Thus, ψ^S depends only on the right stretch tensor $\mathbf{U}_S$ and the scalars n^S and Θ, ensuring compliance with objectivity for arbitrary $\mathbf{F}_S$. Since the right Cauchy-Green deformation tensor $\mathbf{C}_S$ is a function of $\mathbf{U}_S$ (see equation (2.31)), we can equivalently express the Helmholtz energy

$$\overset{*}{\psi}{}^S(\Theta, \mathbf{C}_S, n^S) = \psi^S(\Theta, \mathbf{C}_S, n^S). \tag{3.33}$$

Further, we verify that other quantities, such as the spatial gradient $\operatorname{grad} n^\alpha$ and the seepage velocity $\mathbf{w}_{\beta S}$, also satisfy objectivity. For $\operatorname{grad} n^\alpha$, we find

$$\overset{*}{\operatorname{grad}} n^\alpha = \frac{\partial n^\alpha}{\partial \overset{*}{\mathbf{x}}} \frac{\partial \mathbf{x}}{\partial \mathbf{x}} = \frac{\partial n^\alpha}{\partial \mathbf{x}} \mathbf{Q}^T = \operatorname{grad} n^\alpha \mathbf{Q}^T, \tag{3.34}$$

demonstrating that $\operatorname{grad} n^\alpha$ remains objective. Additionally, the rotation tensor $\mathbf{Q}$ is independent of constituent properties, making $\operatorname{grad} \mathbf{Q} = 0$. By applying the material time derivative, we establish the objectivity of the seepage velocity

$$\left.\begin{aligned} (\overset{*}{\mathbf{x}}{}'_S) &= (\mathbf{Q}\mathbf{x})'_S = \dot{\mathbf{Q}}\mathbf{x} + \mathbf{Q}\mathbf{x}'_S, \\ (\overset{*}{\mathbf{x}}{}'_F) &= (\mathbf{Q}\mathbf{x})'_F = \dot{\mathbf{Q}}\mathbf{x} + \mathbf{Q}\mathbf{x}'_F, \end{aligned}\right\} \quad \Rightarrow \quad \overset{*}{\mathbf{w}}_{FS} = (\overset{*}{\mathbf{x}}{}'_S) - \overset{*}{\mathbf{x}}{}'_F = \mathbf{Q}(\mathbf{x}'_S - \mathbf{x}'_F) = \mathbf{Q}\mathbf{w}_{FS}. \tag{3.35}$$

This analysis confirms that the objectivity condition is preserved for all relevant quantities in the model [73].

3.2.3 Universal dissipation

The evaluation of the entropy inequality in (3.18) imposes critical restrictions on the development of thermodynamically consistent constitutive relations. A key aspect in achieving such consistency is to properly define the dependency of the Helmholtz free energy, ψ^α, for each constituent.

To derive the entropy inequality in its final form, we evaluate the material time derivative $\rho^\alpha(\psi^\alpha)'_\alpha$ for each constituent φ^α. This is done by taking the specific definitions of the Helmholtz free energy functions provided in equation (3.34) as functions of relevant state variables. By taking the time derivatives of these expressions, while considering the material motion of each constituent, we derive the explicit terms required for the entropy inequality

$$\rho^S(\psi^S)'_S = 2n^S\rho^{SR}\mathbf{F}_S\frac{\partial \psi^S}{\partial \mathbf{C}_S}\mathbf{F}_S^T : \mathbf{D}_S + n^S\rho^{SR}\frac{\partial \psi^S}{\partial n^S}(n^S)'_S + n^S\rho^{SR}\frac{\partial \psi^S}{\partial \Theta^S}(\Theta^S)'_S, \tag{3.36a}$$

$$\rho^L(\psi^L)'_L = n^L\rho^{LR}\frac{\partial \psi^L}{\partial s^L}(s^L)'_L + n^L\rho^{LR}\frac{\partial \psi^L}{\partial \Theta^L}(\Theta^L)'_L, \tag{3.36b}$$

$$\rho^G(\psi^G)'_G = n^G\rho^{GR}\frac{\partial \psi^G}{\partial \rho^{GR}}(\rho^{GR})'_G + n^G\rho^{GR}\frac{\partial \psi^G}{\partial \Theta^G}(\Theta^G)'_G. \tag{3.36c}$$

In this formulation, the mass balance relations for each constituent are derived by expressing their respective volume fractions relative to the solid skeleton. This is achieved by integrating the relationships defined in equations (3.8) through (3.9)

$$(n^S)'_S = -\frac{n^S}{\rho^{SR}}\frac{\partial \rho^{SR}}{\partial \Theta^S}(\Theta^S)'_S - n^S(\mathbf{D}_S : \mathbf{I}) + \frac{\hat{\rho}^S}{\rho^{SR}}, \tag{3.37a}$$

$$(n^L)'_S = -\frac{n^L}{\rho^{LR}}\frac{\partial \rho^{LR}}{\partial \Theta^L}(\Theta^L)'_L - n^L(\mathbf{D}_L : \mathbf{I}) + \frac{\hat{\rho}^L}{\rho^{LR}} - \operatorname{grad} n^L \, \mathbf{w}_{LS}, \tag{3.37b}$$

$$(n^G)'_G = -\frac{n^G}{\rho^{GR}}(\rho^{GR})'_G - n^G(\mathbf{D}_G : \mathbf{I}) + \frac{\hat{\rho}^G}{\rho^{GR}} - \operatorname{grad} n^G \, \mathbf{w}_{GS}. \tag{3.37c}$$

Furthermore, the material time derivative $(s^L)'_L$ of the saturation functions can be computed as

$$(n^L)'_L = (s^L n^F)'_L = (s^L)'_L \, n^F + s^L (n^F)'_L \quad \longrightarrow \quad (s^L)'_L = \frac{1}{n^F}\left[(n^L)'_L - s^L (n^F)'_L\right]. \tag{3.38}$$

By incorporating the material time derivative of the saturation constraint along with relations (3.37) and (3.38), the following expression is obtained

$$\begin{aligned}(s^L)'_L = -\frac{1}{n^F}\, [\, & s^L \operatorname{grad} n^F \mathbf{w}_{LS} - s^L \frac{\hat{\rho}^S}{\rho^{SR}} + n^S s^L \frac{1}{\rho^{SR}}\frac{\partial \rho^{SR}}{\partial \Theta^S}(\Theta^S)'_S \\ & + n^S s^L (\mathbf{D}_S : \mathbf{I}) + \frac{n^L}{\rho^{LR}}\frac{\partial \rho^{LR}}{\partial \Theta^L}(\Theta^L)'_L + n^L(\mathbf{D}_L : \mathbf{I}) - \frac{\hat{\rho}^L}{\rho^{LR}}\,].\end{aligned} \tag{3.39}$$

This equation describes the evolution of the material time derivative $(s^L)'_L$ by accounting for phase interactions, including contributions from temperature derivatives, volumetric deformation rates and inter-phase mass exchange.

To ensure that the multiphase body remains fully saturated, we introduce the saturation condition in equation (2.5) by coupling it with a pore pressure p

$$-p \cdot [n^S + n^L + n^G]'_S = -p\,[(n^S)'_S + (n^L)'_S + (n^G)'_S] = 0, \tag{3.40}$$

which leads to the entropy inequality by imposing constraints based on Truesdell's thermodynamic framework [15, 47]. By incorporating equations (3.36), (3.39) and (3.40), we rigorously enforce energy conservation and phase-specific behavior under thermal and mechanical interactions

$$\left\{\mathbf{T}^S - 2\rho^S \mathbf{F}_S \frac{\partial \psi^S}{\partial \mathbf{C}_S}\mathbf{F}_S^T + n^S \rho^S \frac{\partial \psi^S}{\partial n^S}\mathbf{I} + n^S p \mathbf{I} + \frac{n^S}{n^F} s^L \rho^L \frac{\partial \psi^L}{\partial s^L}\mathbf{I}\right\} : \mathbf{D}_S$$

$$+ \left\{\mathbf{T}^L + n^L p \mathbf{I} + n^L \frac{\rho^L}{n^F}\frac{\partial \psi^L}{\partial s^L}\mathbf{I}\right\} : \mathbf{D}_L + \left\{\mathbf{T}^G + n^G p^G \mathbf{I}\right\} : \mathbf{D}_G$$

$$
\begin{aligned}
&+(\Theta^S)'_S\cdot\Big\{-\rho^S\frac{\partial\psi^S}{\partial\Theta^S}+p\frac{n^S}{\rho^{SR}}\frac{\partial\rho^{SR}}{\partial\Theta^S}-\rho^S\eta^S+(n^S)^2\frac{\partial\psi^S}{\partial n^S}\frac{\partial\rho^{SR}}{\partial\Theta^S}+(s^L)^2n^S\frac{\rho^{LR}}{\rho^{SR}}\frac{\partial\rho^{SR}}{\partial\Theta^S}\frac{\partial\psi^L}{\partial s^L}\Big\}\\
&+(\Theta^L)'_L\cdot\Big\{-\rho^L\frac{\partial\psi^L}{\partial\Theta^L}-\rho^L\eta^L+p\frac{n^L}{\rho^{LR}}\frac{\partial\rho^{LR}}{\partial\Theta^L}+s^Ln^L\frac{\partial\rho^{LR}}{\partial\Theta^L}\frac{\partial\psi^L}{\partial s^L}\Big\}\\
&+(\Theta^G)'_G\cdot\Big\{-\rho^G\frac{\partial\psi^G}{\partial\Theta^G}-\rho^G\eta^G\Big\}+(\rho^{GR})'_G\cdot\Big\{-\rho^G\frac{\partial\psi^G}{\partial\rho^{GR}}+p\frac{n^G}{\rho^{GR}}\Big\}\\
&+\hat\rho^S\cdot\Big\{\underbrace{[\psi^L+\frac{p}{\rho^{LR}}+s^L\frac{\partial\psi^L}{\partial s^L}]}_{=\bar\psi^{\mathrm{L}}}-\underbrace{[\psi^S+\frac{p}{\rho^{SR}}+(s^L)^2\frac{\rho^{LR}}{\rho^{SR}}\frac{\partial\psi^L}{\partial s^L}+n^S\frac{\partial\psi^S}{\partial n^S}]}_{=\bar\psi^{\mathrm{S}}}\Big\}\\
&+\hat\rho^G\cdot\Big\{\underbrace{[\psi^L+\frac{p}{\rho^{LR}}+s^L\frac{\partial\psi^L}{\partial s^L}]}_{=\bar\psi^{\mathrm{L}}}-\underbrace{[\psi^G+\frac{p}{\rho^{GR}}]}_{=\bar\psi^{\mathrm{G}}}\Big\}-\frac{1}{\Theta^S}\mathbf{q}^S\cdot\mathrm{grad}\Theta^S\\
&-\frac{1}{\Theta^L}\mathbf{q}^L\cdot\mathrm{grad}\Theta^L-\frac{1}{\Theta^G}\mathbf{q}^G\cdot\mathrm{grad}\Theta^G-\mathbf{w}_{LS}\cdot\underbrace{\Big\{\overbrace{\hat{\mathbf{p}}^L-p\,\mathrm{grad}n^L}^{=\hat{\mathbf{p}}^{\mathrm{L}}_{\mathrm{E}}}-(s^L)^2\rho^{LR}\frac{\partial\psi^L}{\partial s^L}\,\mathrm{grad}\,n^F\Big\}}_{=\hat{\mathbf{p}}^{\mathrm{L}}_{\mathrm{E,mech}}}\\
&-\mathbf{w}_{GS}\cdot\underbrace{\Big\{\hat{\mathbf{p}}^G-p\,\mathrm{grad}n^G\Big\}}_{=\hat{\mathbf{p}}^{\mathrm{G}}_{\mathrm{E}}}\geq 0.
\end{aligned}
\tag{3.41}
$$

The saturation constraint, $n^S+n^L+n^G=1$, ensures that the volume fractions of the solid, liquid and gas phases remain consistent. Additionally, the mass exchange condition, $\hat\rho^S+\hat\rho^G=-\hat\rho^L$, establishes a dynamic equilibrium among the phases by relating their interphase mass transfers, as discussed in Section 3.5. These constraints are crucial for deriving a thermodynamically consistent material response that satisfies the entropy inequality. The entropy inequality can be represented in the following structure

$$
\begin{aligned}
\underbrace{\{\dots\}}_{=\mathbf{0}}:\mathbf{D}_S+\underbrace{\{\dots\}}_{=\mathbf{0}}:\mathbf{D}_L+\underbrace{\{\dots\}}_{=\mathbf{0}}:\mathbf{D}_G+(\Theta^S)'_S\,\underbrace{\{\dots\}}_{=0}+(\Theta^L)'_L\,\underbrace{\{\dots\}}_{=0}\\
+(\Theta^G)'_G\,\underbrace{\{\dots\}}_{=0}+(\rho^{GR})'_G\,\underbrace{\{\dots\}}_{=0}+\underbrace{\mathrm{Dis}}_{\geq 0}\geq 0.
\end{aligned}
\tag{3.42}
$$

The dissipative term Dis satisfies the condition $\mathrm{Dis}\geq 0$, ensuring the thermodynamic requirement of non-negative entropy production. Therein, $\mathbf{L}_\alpha$ is substituted by its symmetric part $\mathbf{D}_\alpha$ due to the symmetry of the Cauchy stress tensors. The underbraced terms are constrained to zero according to thermodynamic principles.

The constraints imposed by the entropy inequality yield specific thermodynamic requirements for the constituent stresses and pressures, ensuring consistency across phases. The pressure for the compressible gas phase can thus be expressed as

$$p^G := p = (\rho^{GR})^2 \frac{\partial \psi^G}{\partial \rho^{GR}}. \tag{3.43}$$

Following the formulation proposed by Ehlers [47] the effective pore-liquid pressure, p^L, is expressed as functions of the partial derivatives of the respective Helmholtz free energy potential. These relationships are defined as

$$p^L := p + s^L \rho^{LR} \frac{\partial \psi^L}{\partial s^L}. \tag{3.44}$$

Building on this, Dalton's law can be articulated to express the effective pressure of the pore-fluid mixture, p^{FR}, as a weighted sum of the partial pressures

$$p^{FR} = s^L p^L + s^G p^G, \tag{3.45}$$

where s^L and s^G are the saturation levels of the liquid and gas phases, satisfying $s^L + s^G = 1$. The effective pressure p^{FR} is interpreted as a pore-space-averaged quantity, differentiating it from the constituent-specific effective pressures. Substituting the expressions for p^L and p^G, and applying the saturation constraint, Dalton's law can be reformulated as

$$p^{FR} = s^L \left(p + s^L \rho^{LR} \frac{\partial \psi^L}{\partial s^L} \right) + s^G p = p + (s^L)^2 \rho^{LR} \frac{\partial \psi^L}{\partial s^L}. \tag{3.46}$$

This formulation emphasizes the interdependence between the saturations, the Helmholtz free energy potentials, and the effective pressures within the pore space, offering a robust framework for analyzing fluid interactions in porous media [4, 69, 122]. The stress tensors for each phase are derived based on (3.41), ensuring thermodynamic consistency while accounting for mechanical and material contributions [50, 90]. Using equations (3.41) and (3.42), the stress tensors for the solid, liquid, and gaseous phases are expressed as

$$\mathbf{T}^S = \mathbf{T}^S_E - n^S \underbrace{\left(p + (s^L)^2 \rho^{LR} \frac{\partial \psi^L}{\partial s^L} \right)}_{:= p^{FR}} \mathbf{I}, \tag{3.47a}$$

$$\text{where} \qquad \mathbf{T}^S_E = 2\rho^{SR} \mathbf{F}_S \frac{\partial \psi^S}{\partial \mathbf{C}_S} \mathbf{F}_S^T - n^S \rho^{SR} \frac{\partial \psi^S}{\partial n^S} \mathbf{I},$$

$$\mathbf{T}^L = -n^L \underbrace{\left(p + s^L \rho^{LR} \frac{\partial \psi^L}{\partial s^L} \right)}_{:= p^L} \mathbf{I}, \tag{3.47b}$$

$$\mathbf{T}^G = -n^G \underbrace{(p)}_{:=p^G} \mathbf{I}. \tag{3.47c}$$

Using the saturation condition (2.5), the total stress is determined as the sum of the partial stresses from all constituents

$$\begin{aligned} \mathbf{T} = \mathbf{T}^S_E - n^S p^{FR}\mathbf{I} - n^L p^L \mathbf{I} - n^G p^G \mathbf{I} &= \mathbf{T}^S_E - p^{FR}\,\mathbf{I} \\ &= 2\rho^S \mathbf{F}_S \frac{\partial \psi^S}{\partial \mathbf{C}_S} \mathbf{F}_S^T - n^S \rho^S \frac{\partial \psi^S}{\partial n^S}\mathbf{I} - p^{FR}\,\mathbf{I}. \end{aligned} \tag{3.48}$$

The dissipation of the fluid component within this multiphasic material provides a basis for defining $\hat{\mathbf{p}}^L_E$, $\hat{\mathbf{p}}^G_E$, and $\hat{\mathbf{p}}^L_{E,\mathrm{mech}}$. Following this approach, the mechanical extra momentum production can be reformulated using the saturation condition and the product rule

$$\hat{\mathbf{p}}^L_E = \hat{\mathbf{p}}^L - p\ \operatorname{grad} n^L, \tag{3.49a}$$

$$\hat{\mathbf{p}}^G_E = \hat{\mathbf{p}}^G - p\ \operatorname{grad} n^G. \tag{3.49b}$$

and

$$\begin{aligned} \hat{\mathbf{p}}^L_{E,mech} &= \hat{\mathbf{p}}^L_E - (s^L)^2 \rho^{LR} \frac{\partial \psi^L}{\partial s^L} \operatorname{grad} n^F \\ &= \hat{\mathbf{p}}^L - p\ \operatorname{grad} n^L - s^L \rho^{LR} \frac{\partial \psi^L}{\partial s^L} \left(s^L \operatorname{grad} n^F \right) \\ &= \hat{\mathbf{p}}^L - p\ \operatorname{grad} n^L - s^L \rho^{LR} \frac{\partial \psi^L}{\partial s^L} \left(\operatorname{grad}(s^L n^F) - n^F \operatorname{grad} s^L \right) \\ &= \hat{\mathbf{p}}^L - \left(p + s^L \rho^{LR} \frac{\partial \psi^L}{\partial s^L} \right) \operatorname{grad} n^L + \rho^L \frac{\partial \psi^L}{\partial s^L} \operatorname{grad} s^L \end{aligned} \tag{3.50}$$

These quantities are typically assumed to be negative and directly proportional to the seepage velocities, $\mathbf{w}_{\beta S}$. Thus, we have

$$\hat{\mathbf{p}}^L_{E,\mathrm{mech}} \propto -\mathbf{w}_{LS} \qquad \text{and} \qquad \hat{\mathbf{p}}^G_E \propto -\mathbf{w}_{GS}. \tag{3.51}$$

Finally, by comparing this formulation with the reference expressions, $\hat{\mathbf{p}}^L_{E,\mathrm{mech}}$ and $\hat{\mathbf{p}}^G_E$ are identified as

$$\hat{\mathbf{p}}^L_{E,\mathrm{mech}} = \hat{\mathbf{p}}^L - p^L \operatorname{grad} n^L + \rho^L \frac{\partial \psi^L}{\partial s^L} \operatorname{grad} s^L, \tag{3.52a}$$

$$\hat{\mathbf{p}}^G_E = \hat{\mathbf{p}}^G - p^G \operatorname{grad} n^G. \tag{3.52b}$$

This reformulation leverages the saturation condition and highlights the coupling between seepage velocities, saturation, and thermodynamic potentials, offering deeper insights into multiphase mechanics.

Dissipation represents the irreversible energy loss in thermodynamic processes, ensuring compliance with the second law of thermodynamics. For the multiphase material under consideration, the total dissipation D is expressed as

$$\begin{aligned} \mathrm{D} = \hat{\rho}^S \cdot [\bar{\psi}^L - \bar{\psi}^S] + \hat{\rho}^G \cdot [\bar{\psi}^L - \bar{\psi}^G] - \frac{1}{\Theta^S}\mathbf{q}^S \cdot \operatorname{grad}\Theta^S \\ - \frac{1}{\Theta^L}\mathbf{q}^L \cdot \operatorname{grad}\Theta^L - \frac{1}{\Theta^G}\mathbf{q}^G \cdot \operatorname{grad}\Theta^G - \mathbf{w}_{LS} \cdot \hat{\mathbf{p}}^L_{E,\mathrm{mech}} - \mathbf{w}_{GS} \cdot \hat{\mathbf{p}}^G_E \geq 0. \end{aligned} \tag{3.53}$$

This formulation incorporates various sources of dissipation, such as heat fluxes due to temperature gradients, mechanical work from inter-phase relative motion, and chemical potential differences between phases. The chemical potentials $\bar{\psi}^\alpha$ govern the mass exchange constraints among the constituents and are defined as

$$\bar{\psi}^S = \psi^S + \frac{p}{\rho^{SR}} + (s^L)^2 \frac{\rho^{LR}}{\rho^{SR}} \frac{\partial \psi^L}{\partial s^L} + n^S \frac{\partial \psi^S}{\partial n^S}, \tag{3.54a}$$

$$\bar{\psi}^L = \psi^L + \frac{p}{\rho^{LR}} + s^L \frac{\partial \psi^L}{\partial s^L}, \tag{3.54b}$$

$$\bar{\psi}^G = \psi^G + \frac{p}{\rho^{GR}}. \tag{3.54c}$$

For a comprehensive discussion on the theoretical framework of chemical potentials, see Bowen [16]. Each term contributes to the overall dissipative behavior of the material, ensuring compliance with the non-negativity requirement, a fundamental aspect of thermodynamic consistency. The concept of extra momentum production, represented by $\hat{\mathbf{s}}^L_{E,\mathrm{mech}}$ and $\hat{\mathbf{s}}^G_E$, provides a basis for setting essential conditions on mass production rates and momentum production terms. Using (3.53), these principles establish constraints for the mass production terms, $\hat{\rho}^S$ and $\hat{\rho}^G$ detailed by Ricken and Bluhm [118]

$$\begin{aligned} \hat{\rho}^S &= \delta^{LS}(\overline{\Psi}^L - \overline{\Psi}^S), \qquad \text{where} \qquad \delta^{LS} \geq 0, \\ \hat{\rho}^G &= \delta^{LG}(\overline{\Psi}^L - \overline{\Psi}^G), \qquad \text{where} \qquad \delta^{LG} \geq 0, \end{aligned} \tag{3.55}$$

Here, δ^{LS} and δ^{LG} are non-negative terms representing the interaction coefficient, respectively. These conditions provide a framework for deriving further expressions for stresses, mass production, and interaction forces within multiphase systems, enabling a consistent treatment of phase coupling and exchange processes [73, 118].

3.3 Constitutive setting of the solid skeleton

3.3.1 Density of solid phase

In our model, the solid skeleton is assumed to be materially incompressible, while its realistic solid density ρ^{SR} depends on temperature, as supported by Cervera et al. [22], Ulm

and Coussy [139, 140]. The relationship is given by

$$\rho^{SR} = \rho_0^{SR} + A_s\Theta, \tag{3.56}$$

where ρ_0^{SR} represents the realistic solid density at the reference temperature, and A_s is a material constant [32]. This temperature dependence reflects concrete's sensitivity to thermal variations, which influence its overall density. Additionally, the apparent solid density $\rho^S = n^S\rho^{SR}$ evolves as concrete undergoes maturation. This change is driven by a reduction in porosity, which occurs due to the progressive hydration of cement. As the hydration process advances, the apparent solid density ρ^S gradually increases, reflecting the material's structural development during its curing phase.

3.3.2 Material law

Fresh concrete is assumed to be an isotropic material. For isotropic materials, the Helmholtz free energy ψ^S and the stress relations depend only on invariants of the deformation tensor $\mathbf{C}_S$, as established in (3.25) and (3.47). The invariance of the Helmholtz free energy under this transformation is expressed as

$$\psi^S(\mathbf{C}_S, n^S) = \psi^S\big(I_{\mathbf{C}_S}, II_{\mathbf{C}_S}, III_{\mathbf{C}_S}, n^S\big) \tag{3.57}$$

This formulation satisfies the invariance and polyconvexity conditions, ensuring the existence of minimizers in finite elasticity. For further details on convexity conditions, refer to Dacorogna [28]. Based on the dependency of the Helmholtz free energy function from (3.57), a Neo-Hookean law is adopted for the nearly incompressible material

$$\psi^S = \left(\frac{n^S}{n_{0S}^S}\right)^n \frac{1}{\rho_{0S}^S}\Big\{\frac{\mu^S}{2}(I_{\mathbf{C}_S} - 3) - \mu^S \ln J_S + \lambda^S \frac{1}{2}(\ln J_S)^2\Big\}, \tag{3.58}$$

with a dimensionless parameter n describing the change of porosity. The remaining terms correspond to the standard Neo-Hookean material model. Here, μ^S and λ^S are the macroscopic Lamé constants, and $III_S = J_S^2$ is the third invariant, as defined in $(2.39)_3$. Using equations (3.58) and (3.47), the effective solid Cauchy stress is derived as

$$\begin{aligned}\mathbf{T}_E^S = &\left(\frac{n^S}{n_{0S}^S}\right)^{(n+1)} \frac{\rho^{SR}}{\rho_0^{SR}}\Big\{\mu^S(\mathbf{B}_S - \mathbf{I}) + \lambda^S(\ln J_S)\mathbf{I}\Big\} \\ &- n\left(\frac{n^S}{n_{0S}^S}\right)^{n+1} \frac{\rho^{SR}}{\rho_0^{SR}}\Big\{\frac{\mu^S}{2}(I_{\mathbf{C}_S} - 3) - \mu^S \ln J_S + \lambda^S \frac{1}{2}(\ln J_S)^2\Big\}\mathbf{I}.\end{aligned} \tag{3.59}$$

Furthermore, combining (3.58), (3.47), and (3.59), the total solid Cauchy stress can be expressed as

$$\begin{aligned}\mathbf{T} = &- p^{FR}\mathbf{I} - n\left(\frac{n^S}{n^S_{0S}}\right)^{n+1}\frac{\rho^{SR}}{\rho^{SR}_0}\left\{\frac{\mu^S}{2}(I_{\mathbf{C}_S}-3) - \mu^S \ln J_S + \lambda^S \frac{1}{2}(\ln J_S)^2\right\}\mathbf{I} \\ &+ \left(\frac{n^S}{n^S_{0S}}\right)^{n+1}\frac{\rho^{SR}}{\rho^{SR}_0}\left\{\mu^S(\mathbf{B}_S - \mathbf{I}) + \lambda^S(\ln J_S)\mathbf{I}\right\},\end{aligned} \tag{3.60}$$

with the left Cauchy-Green tensor $\mathbf{B}_S = \mathbf{F}_S\mathbf{F}_S^T$.

3.4 Constitutive setting of the pore fluids

The behavior of fresh concrete is significantly influenced by its fluid phases, comprising liquid water and gas. The interaction between water and solid particles, particularly cement grains, initiates hydration, forming C-S-H phase that contribute to the development of its solid framework. For an accurate representation of the mechanical response of fresh concrete, constitutive models must effectively account for these hydraulic processes.

Darcy's pioneering work in 1856 demonstrated that fluid flow through porous media, such as concrete, adheres to a linear relationship between the pressure gradient and discharge rate. In fresh concrete, the dynamics of fluid flow are governed by pressures in the liquid and gas phases, influenced by pore structure and particle arrangement. Furthermore, the deformation of concrete modifies its pore network, affecting flow paths and potentially introducing anisotropic behavior. This study focuses on modeling the flow dynamics within fresh concrete under isotropic conditions, incorporating the coupling effects of the flow, deformation, hydration, and evaporation processes to improve simulation fidelity.

Fluid flow

The linear momentum balance for the fluid phases is derived using the conservation of linear momentum, including the contributions of fluid stress and volume fractions. For both fluid phases $\beta \in \{L, G\}$, the general form of the linear momentum balance is expressed as

$$\mathbf{0} = \mathrm{div}\mathbf{T}^\beta + \rho^\beta \mathbf{b} + \hat{\mathbf{p}}^\beta, \tag{3.61}$$

where $\mathbf{T}^\beta$ represents the fluid stress tensor, $\rho^\beta \mathbf{b}$ denotes the body force acting on the fluid phase, and $\hat{\mathbf{p}}^\beta$ accounts for production terms. By introducing the phase stress relation from (3.47) and incorporating the entropy inequality constraints, the linear momentum balance

can be reformulated. Using equations (3.49) and (3.50), the momentum balance for each fluid phase takes the following form

$$\hat{\mathbf{p}}_E^L - \rho^L \frac{\partial \psi^L}{\partial s^L} \operatorname{grad} s^L = n^L \operatorname{grad} p^L - \rho^L \mathbf{b}, \tag{3.62a}$$

$$\hat{\mathbf{p}}_E^G = n^G \operatorname{grad} p^G - \rho^G \mathbf{b}. \tag{3.62b}$$

For non-viscous fluids, the effective production term $\hat{\mathbf{p}}_E^\beta$ is related to the Darcy seepage velocity $\mathbf{w}_{\beta S}$ as

$$\hat{\mathbf{p}}_E^\beta = -(n^\beta)^2 \, \frac{\mu^\beta}{k^{r\beta} k \, \mathbf{I}} \, \mathbf{w}_{\beta S}, \tag{3.63}$$

where $k^{r\beta}$ denotes the relative permeability of the fluid phase β, k represents the intrinsic permeability of the solid skeleton, and μ^β is the viscosity of phase β.

After deriving the linear momentum balance in (3.61) and taking care of production terms in (3.62) and (3.63), we obtain the following form for the seepage velocities of fluid phases, $\mathbf{w}_{LS}$ and $\mathbf{w}_{GS}$, commonly referred to as Darcy's law

$$n^L \, \mathbf{w}_{LS} = -\frac{k^{rL} k \, \mathbf{I}}{\mu^L} \left(\operatorname{grad} p^L - \rho^{LR} \, \mathbf{b} + \rho^L \frac{\partial \psi^L}{\partial s^L} \operatorname{grad} s^L \right), \tag{3.64a}$$

$$n^G \, \mathbf{w}_{GS} = -\frac{k^{rG} k \, \mathbf{I}}{\mu^G} \left(\operatorname{grad} p^G - \rho^{GR} \, \mathbf{b} \right). \tag{3.64b}$$

Here, considering the slow nature of mass exchange processes in the medium, the term $\hat{\rho}^\beta \mathbf{x}'_\beta \approx 0$ has been neglected. This simplification significantly reduces the complexity of the governing equations while maintaining physical relevance. The presented formulation provides a robust framework for modeling coupled processes of fluid flow and deformation in porous materials [44, 64, 121].

Intrinsic and relative permeability in fresh concrete

The transformation of the internal structure during concrete maturation significantly alters its intrinsic permeability. These changes are driven not only by a reduction in porosity but also by modifications in pore connectivity. Parameters such as tortuosity and the critical pore radius, as discussed in [74, 96], play crucial roles in defining these structural changes. Intrinsic permeability, a fundamental material property, measures the ease of fluids flow through a porous medium under a pressure gradient. This property is typically determined through experimental studies using water or gas as the penetrating medium.

Schneider and Herbst [123] conducted experiments to investigate how temperature and gas pressure influence the intrinsic permeability of various concrete types. Their results were

approximated using the following phenomenological formula [63]

$$k(\Theta, p^G) = k_0 \cdot 10^{A_T(\Theta-\Theta_0)} \left(\frac{p^G}{p^0}\right)^{A_p}, \tag{3.65}$$

where A_T and A_p are material-specific constants and k_0 is the reference permeability. While intrinsic permeability is a key property of the concrete matrix, the behavior of gaseous and liquid phases within concrete differs significantly, necessitating the use of relative permeability to describe phase-specific flow. Muskat and Meres [106] proposed treating the permeability of a specific phase β as isotropic, represented as $k^{r\beta}$. The relative permeability approach for capillary porous materials follows the method introduced by van Genuchten [141]

$$\begin{aligned} k^{rL}(s^L) &= \sqrt{s^L}\,(1-(1-(s^L)^{1/m})^m)^2, \\ k^{rG}(s^L) &= \sqrt{1-s^L}\,(1-(s^L)^{1/m})^{2m}, \end{aligned} \tag{3.66}$$

where m is an experimentally determined parameter [98]. The fluid viscosities are dependent on temperature, particularly during the early stages of concrete hardening when significant heat generation occurs due to exothermic hydration reactions. Liquid viscosity as a function of temperature can be approximated using the Watson formula [136]

$$\begin{aligned} \mu^L(\Theta) &= 0.6612(\Theta-229)^{-1.562}, \\ \mu^G(\Theta) &= 3.85\cdot 10^{-8}\Theta. \end{aligned} \tag{3.67}$$

Partially saturated zone

The behavior of the partially saturated zone is critical for evaluating pore-fluid mobility in concrete. Deformation-free water retention tests provide the data necessary to describe the retention curve, which characterizes the relationship between capillary pressure, p^C, and liquid saturation, s^L. For concrete under typical conditions, where temperatures remain below the critical point of water ($\Theta < \Theta_{cr}$), and within the capillary saturation range, the capillary pressure is defined as

$$p^C = p^G - p^L = p - \left(p + s^L \rho^{LR} \frac{\partial \psi^L}{\partial s^L}\right) = -s^L \rho^{LR} \frac{\partial \psi^L}{\partial s^L}. \tag{3.68}$$

This equation applies under thermodynamic equilibrium conditions and can be derived using the Coleman-Noll method [71, 72]. Relative humidity Φ, as a function of capillary pressure, is derived using Kelvin's equation for equilibrium states of capillary water [87]

$$\Phi = \exp\left(-\frac{p^C}{\rho^{LR}}\frac{M_W}{R\Theta}\right), \tag{3.69}$$

where M_W is the molar mass of water and R is the universal gas constant. The relationship between capillary pressure and relative humidity, as illustrated in (3.69), highlights the impact of microstructural evolution during hydration on hygral behavior [63, 92].

The free Helmholtz energy of incompressible pore water, ψ^L, provides the basis for deriving water saturation values [24]. Early hydration mainly affects micro- and smaller meso-pores, altering porosity, which is described by sorption isotherms linking saturation to relative humidity. Retention curves, relating saturation to capillary pressure, can be modeled using Brooks-Corey [21] and van Genuchten [141] constitutive relations

$$s^L = \left(1 + \left(\frac{p^C}{a}\right)^{b/(b-1)}\right)^{-1/b}, \tag{3.70}$$

where a and b are material constants determined experimentally [5, 64]. For a detailed discussion on the link between the free energy function of water and the saturation formulation, the reader is referred to the literature [64]. It should be noted, however, that this connection, the relationship between capillary pressure and degree of saturation, can become unstable under high-temperature conditions, due to rapid evaporation, phase changes, and non-equilibrium effects. In such cases, alternative formulations or temperature-dependent regularization may be necessary. For further insight into these high-temperature instabilities and their treatment, the reader is referred to [30, 112, 113].

Density of liquid water

In this model, liquid water is treated as an incompressible fluid, meaning that its volume and realistic density, ρ^{LR}, remain unchanged under variations in pressure. However, ρ^{LR} exhibits a significant dependency on temperature, as extensively documented in the literature [60, 67]. The temperature-dependent nature of liquid water density is critical for accurately capturing its physical properties and behavior, particularly in simulations of concrete processes where thermal effects play a crucial role. The temperature dependency of ρ^{LR} is expressed using the following empirical, non-linear state equation

$$\begin{aligned}\rho^{LR} =& (b_0 + b_1\Theta + b_2\Theta^2 + b_3\Theta^3 + b_4\Theta^4 + b_5\Theta^5) + \\ & (p_{\mathrm{w1}} - p_{\mathrm{w,ref}})(a_0 + a_1\Theta + a_2\Theta^2 + a_3\Theta^3 + a_4\Theta^4 + a_5\Theta^5),\end{aligned} \tag{3.71}$$

where p_{w1} and $p_{\mathrm{w,ref}}$ are reference pressures assumed to remain constant. The coefficients a_i and b_i ($i = 0, 1, \ldots, 5$) are material-specific empirical constants determined through experimental studies. This formulation effectively captures the influence of temperature and pressure on the density of liquid water, as demonstrated in studies such as [32, 62, 63].

Pore gas

Unlike solid and liquid phases, the pore gas is treated as a compressible fluid. Its realistic density, ρ^{GR}, varies with temperature and pressure. The Clapeyron equation of state for an ideal gas describes the realistic density of the gas phase

$$\rho^{GR} = p^{G} \frac{M_G}{R\Theta}, \tag{3.72}$$

where M_G is the molar mass of the gas, and R is the universal gas constant. This equation allows for the explicit representation of gas compressibility and its response to varying thermodynamic conditions. The Helmholtz free energy function provides the thermodynamic basis for describing the gas phase's behavior [122]. It is given as

$$\psi^{G}(\rho^{GR}, \Theta) = R\,\Theta\,\ln\rho^{GR} + g(\Theta). \tag{3.73}$$

This formulation links the internal energy and entropy contributions to the compressibility and thermal behavior of the gas phase.

3.5 Mass and heat exchange

The modeling of multiphase materials presents a significant challenge, necessitating a comprehensive understanding of mass and energy transfer mechanisms within the system. Central to this framework is the concept of mass exchange, which plays a pivotal role in describing the behavior of porous materials. Mass exchange governs the transport of mass between the three phases and is explicitly captured through the production terms in the mass balance equations for each phase, as detailed in (3.9a), (3.9b), and (3.9c).

In addition to mass transfer, the model incorporates the enthalpy balance for the entire mixture, accounting for the distribution of heat across various thermodynamic processes within the phases. The enthalpy transfer is crucial in describing the thermal behavior of the system, as heat is both accumulated and redistributed due to interactions between the phases. Two primary processes drive heat generation within the material: mass exchange between the phases and the associated heat effects of these processes. These interactions lead to variations in temperature and enthalpy, which influence the overall behavior of the material. The accurate representation of mass exchange and enthalpy transfer is critical for predicting the behavior of multiphase systems, particularly in the context of fresh concrete exposed to environmental conditions and undergoing maturing processes. In this regard, the subsequent sections explore the intricacies of mass exchange due to cement hydration and evaporation. Both processes are modeled as reversible, capturing their mutual interactions and their substantial impact on the thermodynamic and mechanical behavior of fresh concrete.

Hydration When cement comes into contact with water, a series of chemical reactions, collectively known as hydration, begins. Hydration is a complex sequence of interactions primarily involving the liquid and solid phases. This process leads to the formation of hydration products that progressively increase the solid phase's volume fraction over time. As these hydration products develop and expand, they occupy the pores within the material, resulting in a reduction of the volume fraction of the fluid phase and an increase in the density of the solid phase.

The ongoing development of concrete's microstructure during hydration has a direct influence on its mechanical and transport properties, both of which are commonly described as functions of the hydration degree. In this work, the evolution of cement hydration and material aging is modeled following the approach proposed by Gawin et al. [62, 130]. The cement hydration degree, denoted by $\xi(t)$, quantifies the extent of the hydration reaction by expressing the ratio between the mass of hydrated cement at time t, $c_{\text{hyd}}(t)$, and the initial cement mass c

$$\xi(t) = \frac{c_{\text{hyd}}(t)}{c}. \tag{3.74}$$

Due to the typically low water-to-cement ratio (w/c) in concrete mixes, complete hydration rarely occurs. As a result, $\xi(t)$ approaches a limiting value $\xi_\infty \leq 1$ over time. To better represent hydration progress under such constraints, the hydration degree $\Gamma(t)$ is introduced

$$\Gamma(t) = \frac{m_{\text{hyd}}(t)}{m_{\text{hyd},\infty}}, \tag{3.75}$$

where $m_{\text{hyd}}(t)$ is the mass of chemically bound water at time t, and $m_{\text{hyd},\infty}$ is its theoretical maximum under full hydration. The link between $\xi(t)$ and $\Gamma(t)$ is given as

$$\xi(t) = \xi_\infty \Gamma(t). \tag{3.76}$$

The theoretical upper limit of hydration, $\bar{\xi}_\infty$, can be estimated using Powers' model [115], which assumes full consumption of capillary water. However, the actual value of ξ_∞ is often lower and must be determined empirically. One widely used estimation is given by Mills' equation [105, 130]

$$\xi_\infty = \frac{1.031\ \frac{w}{c}}{0.194 + \frac{w}{c}}. \tag{3.77}$$

Powers' model also relates the total chemically bound water content to the concrete mix composition. Under the assumption that $\xi_\infty = \bar{\xi}_\infty$, the bound water at full hydration can be calculated as

$$m_{\text{hyd},\infty} = 0.228 c \xi_\infty. \tag{3.78}$$

The mass exchange due to hydration, denoted as $\hat{\rho}^S$ in equation (3.9a), is modeled as

$$\hat{\rho}^S = \hat{\rho}_{\text{hydr}} = \frac{\mathrm{d}\Gamma_{\text{hydr}}}{\mathrm{d}t}\, m_{\text{hyd},\infty}, \qquad \frac{\mathrm{d}\Gamma_{\text{hydr}}}{\mathrm{d}t} = A_\Gamma(\Gamma_{\text{hydr}})\beta_\Phi(\Phi)\exp\left(\frac{-E_a}{R\Theta}\right), \tag{3.79}$$

where $\frac{\mathrm{d}\Gamma_{\mathrm{hydr}}}{\mathrm{d}t}$ represents the rate of hydration degree within concrete [64]. This rate depends on temperature Θ, the universal gas constant R, the coefficient β_Φ, the activation energy E_a and the normalized affinity A_Γ. The normalized affinity, A_Γ, is determined experimentally through adiabatic tests [22, 139] and is given as

$$A_\Gamma(\Gamma_{\mathrm{hydr}}) = A_1 \left(\frac{A_2}{\kappa_\infty} + \kappa_\infty \Gamma_{\mathrm{hydr}} \right) (1 - \Gamma_{\mathrm{hydr}}) \exp(-\bar{\eta}\Gamma_{\mathrm{hydr}}), \tag{3.80}$$

where the coefficients $(A_1, A_2, \kappa_\infty, \bar{\eta})$ are derived from the observed temperature evolution during hydration. The chemical reactions occurring during hydration are exothermic, leading to heat and mass sources within the material. The intensity of these heat sources can be measured directly through calorimetric tests, which are often used to determine the hydration degree. Alternatively, the heat sources can be indirectly related to mass sources by assuming a constant specific enthalpy of hydration, $\Delta h_{\mathrm{hydr}} = h^L - h^S$, which is widely accepted in practice. As hydration progresses, particularly during the early stages, the generated heat causes a significant rise in temperature. In massive concrete structures, temperature increases of up to $70 - 80$ K are commonly observed, a phenomenon referred to as self-heating [13]. Concurrently, the hydration reactions consume a substantial amount of water, leading to a decrease in the volume fraction of the liquid phase.

Evaporation In parallel with the hydration process, evaporation occurs, involving the phase transition of liquid water into the gas phase within the pores due to internal or environmental conditions. Evaporation affects the density and volume of the medium, influencing the overall behavior of the material. Factors such as temperature, humidity, permeability and the hydration stage all contribute to the evaporation process. The coupling between hydration and evaporation processes plays a critical role in determining the material's response to external factors, including environmental exposure and the progression of concrete maturing. While hydration increases the density of the solid phase, evaporation can lead to a reduction in the overall density of the medium.

To investigate evaporation during the early stages of concrete hardening, a new formulation for the evaporation process is proposed

$$\hat{\rho}^G(\mathrm{w}_{LS}, \Gamma_{\mathrm{hydr}}) = \mathcal{C}\, \hat{\rho}^G_{\mathrm{w}}(\mathrm{w}_{LS})\, \hat{\rho}^G_\Gamma(\Gamma_{\mathrm{hydr}})\,, \tag{3.81}$$

where $\hat{\rho}^G(\mathrm{w}_{LS}, \Gamma_{\mathrm{hydr}})$ represents the evaporation rate of the liquid phase, influenced by two primary factors: $\hat{\rho}^G_{\mathrm{w}}(\mathrm{w}_{LS})$, which accounts for the effect of seepage velocity $\|\mathbf{w}_{LS}\|$ of the liquid phase, and $\hat{\rho}^G_\Gamma(\Gamma_{\mathrm{hydr}})$, which captures the impact of hydration degree on the interaction between cement particles and liquid water. The parameter $\mathcal{C}$ denotes the maximum mass exchange between the fluid phases. The first factor, $\hat{\rho}^G_{\mathrm{w}}(\mathrm{w}_{LS})$, is modeled as a function of the norm of the seepage velocity $\|\mathbf{w}_{LS}\|$

$$\hat{\rho}^G_{\mathrm{w}}(\mathrm{w}_{LS}) = \exp(\beta_1\, \|\mathrm{w}_{LS}\|)\,, \tag{3.82}$$

which reflects the increasing energy and mobility of water molecules as hydration progresses and heat is generated within the material. The enhanced mobility of water disrupts liquid bonds, leading to increased evaporation rates, as illustrated in Figure 3.2.

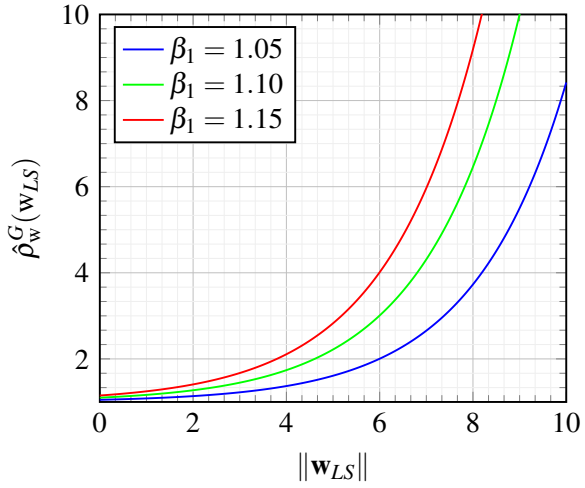

Figure 3.2: Evaporation rate $\hat{\rho}_{\mathrm{w}}^{G}(\mathrm{w}_{LS})$ as a function of seepage velocity for $\beta_1 = 1.05, 1.1, 1.15$ [s/mm].

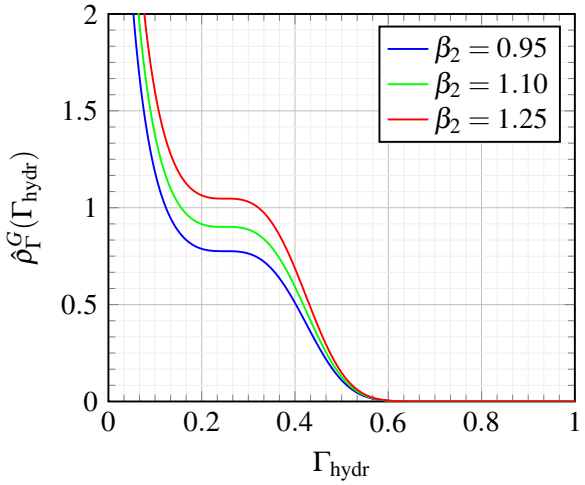

Figure 3.3: Variation of evaporation rate $\hat{\rho}_{\Gamma}^{G}(\Gamma_{\mathrm{hydr}})$ as a function of hydration degree $\Gamma_{\mathrm{hydr}} \in [0,1]$, demonstrating the influence of β_2 values ($\beta_2 = 0.95, 1.10, 1.25$ [−]) with fixed parameters $\beta_3 = 125.0$ [−] and $\beta_4 = 0.25$ [−].

The second factor, $\hat{\rho}_{\Gamma}^{G}(\Gamma_{\mathrm{hydr}})$, describes the influence of the hydration degree on the evaporation rate and is modeled as

$$\hat{\rho}_{\Gamma}^{G}(\Gamma_{\mathrm{hydr}}) = \exp[\beta_2 - \beta_3\ (\Gamma_{\mathrm{hydr}} - \beta_4)^3]\ . \tag{3.83}$$

The parameters $\beta_i, i \in (1,2,3,4)$ are material constants calibrated to replicate the material's physical behavior. During the early hydration stage, the interaction between cement particles and liquid water results in peak hydration and evaporation rates ($\Gamma_{\text{hydr}} \in [0, 0.2]$). Over time, as hydration progresses ($\Gamma_{\text{hydr}} \in [0.2, 0.4]$), the evaporation rate gradually decreases, eventually leading to a rigid, low-permeability structure that limits further interaction between phases.

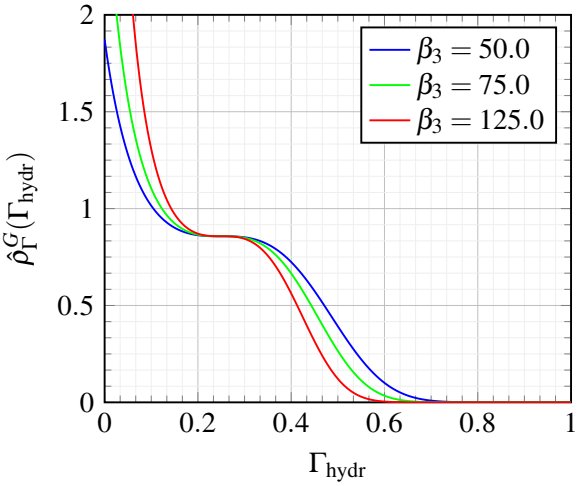

Figure 3.4: Dependence of evaporation rate $\hat{\rho}^G_\Gamma(\Gamma_{\text{hydr}})$ on hydration degree $\Gamma_{\text{hydr}} \in [0,1]$, showing the effect of varying β_3 values ($\beta_3 = 50.0, 75.0, 125.0$ $[-]$) with fixed parameters $\beta_2 = 1.05$ $[-]$ and $\beta_4 = 0.25$ $[-]$.

Figures 3.3, 3.4, and 3.5 highlight the dependency of evaporation rates on parameters β_2, β_3, and β_4. These figures demonstrate how changes in parameter values influence the evaporation function. The enthalpy equation for the entire mixture incorporates the enthalpies of the gas and liquid phases. The specific enthalpy difference between these phases is given as

$$\Delta h_{\text{evap}} = h^G - h^L = 2.672 \cdot 10^5 (\Theta - \Theta_{cr}), \tag{3.84}$$

where Θ_{cr} is the critical temperature of water [32].

3.6 Constitutive modeling of heat fluxes and thermal capacities

The modeling of hygro-thermal processes relies on establishing precise relationships between the flow of extensive thermodynamic properties and the corresponding intensive thermodynamic quantities, also known as thermodynamic forces. These relationships, derived from fundamental principles such as entropy inequality, define the transport properties and interactions within the system. Fourier's law governs heat conduction within

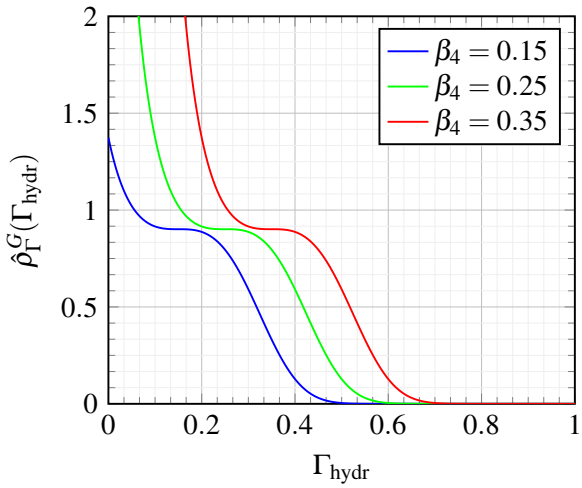

Figure 3.5: Variation of evaporation rate $\hat{\rho}_\Gamma^G(\Gamma_{\text{hydr}})$ with hydration degree $\Gamma_{\text{hydr}} \in [0,1]$, illustrating the influence of β_4 values ($\beta_4 = 0.15, 0.25, 0.35$ $[-]$) under fixed parameters $\beta_2 = 1.1$ $[-]$ and $\beta_3 = 125.0$ $[-]$.

materials like aging concrete

$$\mathbf{q} = -\lambda_{\text{eff}}(\Theta)\ \text{grad}\Theta, \qquad \text{with} \qquad \mathbf{q} = \sum_\alpha \mathbf{q}^\alpha, \tag{3.85}$$

where $\mathbf{q}$ represents the total heat flux, and the effective thermal conductivity $\lambda_{\text{eff}}(\Theta)$ is a function of temperature, moisture content and hydration levels. Experimental studies on fresh and fully cured concrete under varying temperatures reveal that $\lambda_{\text{eff}}(\Theta)$ accounts for not only conduction but also micro-scale processes like radiation and convection within the pore structure. The hydration degree indirectly affects $\lambda_{\text{eff}}(\Theta)$ by influencing fluid volume fractions and saturation levels. The effective thermal conductivity is expressed as

$$\lambda_{\text{eff}}(\Theta) = \lambda_{\text{dry}}(\Theta)\left(1 + \frac{4\rho^L}{\rho^S}\right), \qquad \text{with} \qquad \lambda_{\text{dry}}(\Theta) = \lambda_{\text{d0}}(1 + A_\lambda(\Theta - \Theta_0)), \tag{3.86}$$

where $\lambda_{\text{dry}}(\Theta)$ represents the thermal conductivity of the dry material, Θ_0 is the reference temperature, and A_λ is an experimentally derived constant. Notable studies, including those by Harmathy [75] and Gawin et al. [66], provide detailed insights into these dependencies.

The thermal capacity of partially saturated concrete is computed as a summation of the capacities of its individual components

$$\rho C_P = \rho^S C_{P0}^S + \rho^L C_{P0}^L + \rho^G C_{P0}^G. \tag{3.87}$$

While the phase-specific heat capacities C_{P0}^α are generally considered independent of temperature, this assumption simplifies the modeling process without substantially impacting

the overall thermal capacity [63]. These capacities correspond to the solid, liquid and gas phases at the initial time $t = 0$. The relationship to enthalpy is derived in Appendix A.1. Comprehensive discussions on this topic are provided in sources such as [122] and [47].

4 EXPERIMENTAL INVESTIGATIONS OF FRESH CONCRETE

The behavior of fresh concrete, particularly during its early stages, is critical to understanding how the material will perform both during and after construction. Fresh concrete, in its still deformable state, undergoes continuous changes due to the interactions between its solid, liquid and gaseous phases. These interactions, driven by ongoing hydration and evaporation, play a significant role in defining the long-term properties of the concrete, such as its strength and durability. In this thesis, the focus is not on experimentally studying the behavior of fresh concrete but on combining this data with numerical models to provide a more comprehensive understanding of the material's performance. The integration of experimental results with numerical simulations allows for more accurate predictions of the behavior of fresh concrete in practical applications.

This chapter is structured to first establish the motivation and importance of studying the properties of fresh concrete. We begin by discussing the relevance of early-stage hydration behavior in ensuring concrete's workability and durability. Following this, the chapter introduces the experimental setup used for studying these behaviors, particularly focusing on the Dynamic Vapor Sorption (DVS) machine. The methodology and principles behind DVS are discussed to highlight its relevance in analyzing mass and heat exchanges within concrete due to the evaporation process. Next, we move on to the materials and sample preparation procedures, providing details on how samples are prepared to ensure consistent and reliable results. Finally, initial experimental tests are conducted to fine-tune the setup, setting the stage for the final tests, which aim to gather the data required for the numerical modeling of evaporation.

Understanding the behavior of fresh concrete is crucial due to its direct impact on construction efficiency and the performance of the final structure. Its properties are shaped by complex phase interactions during early hydration, which ultimately influence the long-term durability and strength of the structure [54, 100]. A deeper understanding of these early-age behaviors is essential for optimizing concrete mix designs, especially in demanding applications such as large-scale infrastructure [82, 119].

This chapter introduces the experimental methodology used to investigate moisture transport and phase interaction in fresh concrete, with a particular focus on evaporation during early hydration. The setup, based on Dynamic Vapor Sorption, provides high-resolution data that later serves to calibrate and validate the numerical model presented in the following chapters. By integrating experimental results with simulation tools, the research supports more accurate prediction and optimization of early-age performance, contributing to more efficient and sustainable construction practices [55, 146].

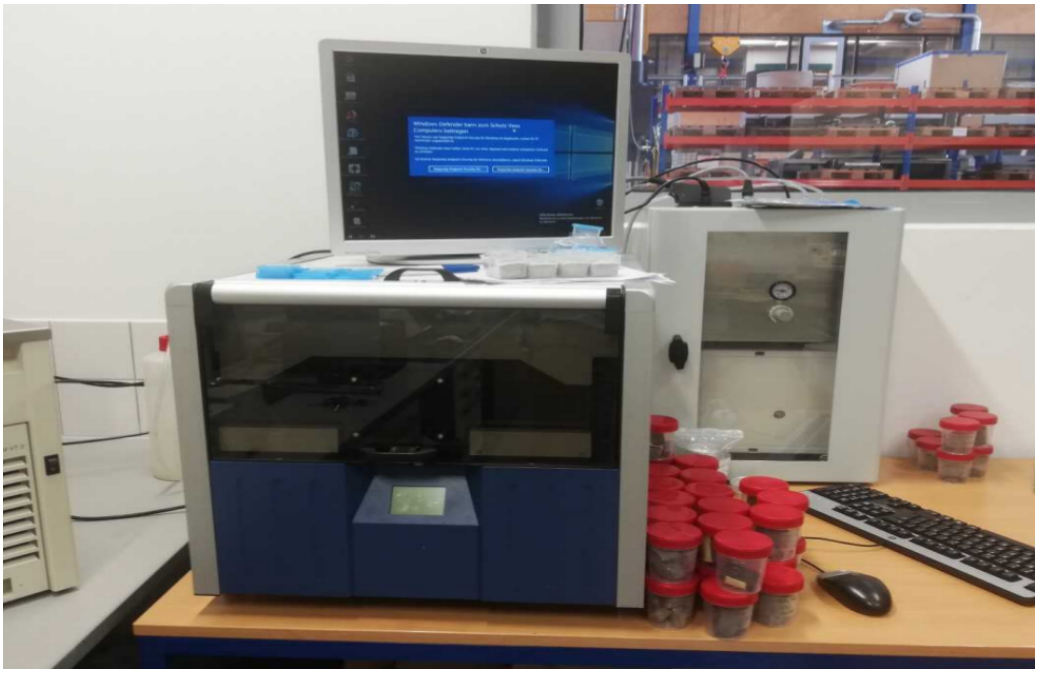

Figure 4.1: External view of the dynamic vapor sorption machine setup.

4.1 Experimental setup

The study utilizes the Dynamic Vapor Sorption (DVS) technique as a fundamental tool for investigating the interaction of water and gas phase within the fresh concrete. This method is essential for understanding moisture transport, sorption behavior, and their impact on hydration and evaporation processes, ultimately influencing concrete durability and microstructural formation. The DVS system, equipped with precision humidity and temperature controls, facilitates the simulation of realistic environmental curing conditions for cement-based materials. Within a controlled chamber, an external view of which is shown in Figure 4.1, the DVS setup can systematically alter relative humidity (Φ) and temperature to replicate exposure scenarios, which are crucial for assessing concrete's long-term durability under varying conditions [45, 58, 120]. Central to the DVS's utility is its ability to monitor real-time mass changes in concrete samples, which directly reflect moisture uptake and desorption in response to variations of relative humidity. These insights allow researchers to characterize moisture-dependent properties like permeability, which impacts how concrete withstands degradation processes such as carbonation, chloride ingress, and freeze-thaw cycles in service environments [1, 12].

The DVS system can produce water vapor sorption isotherms, which show how much moisture a material holds at different humidity levels, making it especially useful for material science research. These isotherms reveal the pore structure and mass exchange within

cementitious materials, with high-resolution data enabling detailed assessments of the concrete properties [93, 132]. Additionally, the system is sensitive enough to capture sorption hysteresis, a behavior often linked to irreversible hydration reactions and pore-blocking effects during cyclic moisture loading and unloading [143]. For studies on cement mixtures containing supplementary cementitious materials (SCMs), such as fly ash or slag, the DVS method provides invaluable insights into how these additives alter moisture behavior and pore structure [95, 144]. These measurements are critical for predictive modeling, where DVS-generated data inform simulations used to estimate service life and performance of concrete structures exposed to fluctuating humidity and temperature conditions [86, 116, 145].

4.1.1 Chamber configuration and sample monitoring

The DVS setup includes a specialized humidity-controlled chamber that balances dry and saturated air streams to maintain accurate relative humidity levels, while a high-sensitivity microbalance continuously records mass changes as the sample absorbs or releases moisture. This setup enables the examination of how concrete samples respond to specific relative humidity and temperature conditions that affect the microstructural properties of cementitious materials [45, 86, 132]. The controlled environment simulates realistic curing and exposure conditions, ensuring moisture interactions comparable to real-life scenarios [12, 84, 120]. Its design minimizes condensation and ensures uniform vapor distribution, which is crucial for accurate sorption data. Uneven vapor distribution can lead to moisture gradients within the sample, potentially distorting results and yielding inaccurate assessments of sorption characteristics. With a configuration that prevents condensation, the DVS chamber provides reliable measurements across a broad range of humidity levels, including both hygroscopic and super-hygroscopic conditions that are critical for analyzing pore structure and moisture retention [58, 145]. To visually illustrate the DVS chamber setup, Figure 4.2 provides a glimpse into the internal structure of the DVS chamber, showcasing the sample placement area and humidity control components that facilitate precise environmental monitoring.

The DVS's high-precision microbalance is central to its ability to detect even minimal changes in sample mass due to moisture uptake or release. This sensitivity enables the detection of subtle variations in moisture content that correlate with microstructural changes, such as the development of calcium-silicate-hydrate (C-S-H) gels during hydration. These gels significantly influence the pore structure and moisture transport properties of concrete, especially when subjected to different relative humidity levels and contribute to understanding the durability of concrete in varying conditions [93, 95].

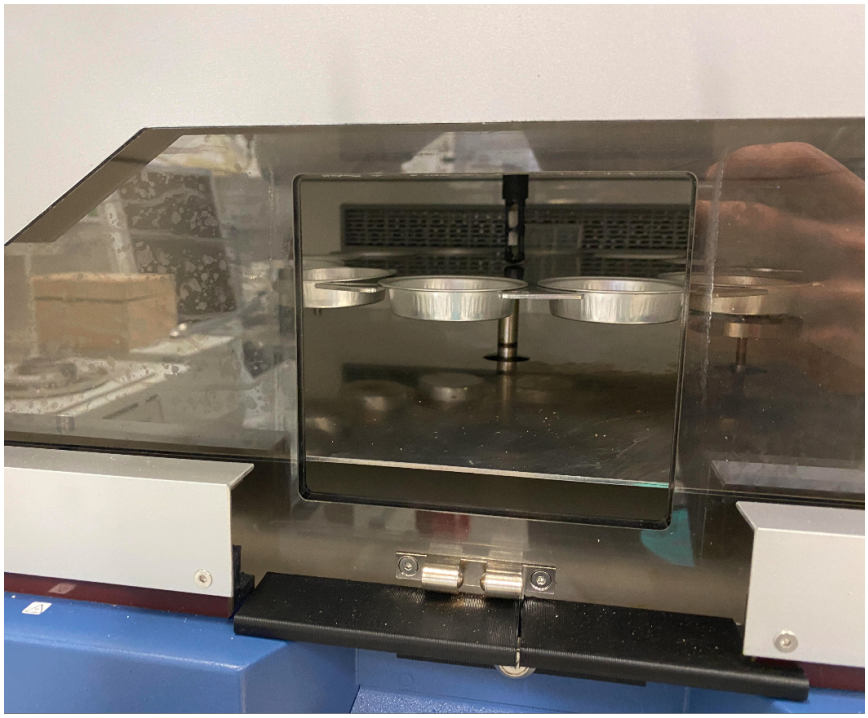

Figure 4.2: Internal view of the DVS machine chamber showing sample placement and humidity control components.

4.1.2 Humidity and temperature control

The Dynamic Vapor Sorption system precisely regulates relative humidity and temperature by mixing dry and saturated air streams, ensuring a controlled environment for moisture transport studies in cementitious materials [1, 116]. Since even minor temperature variations can distort sorption data and pore structure interpretation, the system uses a real-time feedback loop to maintain thermal stability [58, 132]. Figure 4.3 illustrates the DVS setup, highlighting how humidity is controlled through air mixing and how symmetric reference compensation ensures consistent baseline conditions. The design minimizes condensation and promotes uniform vapor distribution, critical for accurate relative humidity regulation around the sample [86, 95].

This level of control enables high-resolution measurement of moisture absorption and desorption rates, providing key insights into hydration behavior and microstructural development. As a result, the DVS system supports the generation of reliable data for calibrating models of moisture-driven degradation in concrete [104, 144, 145].

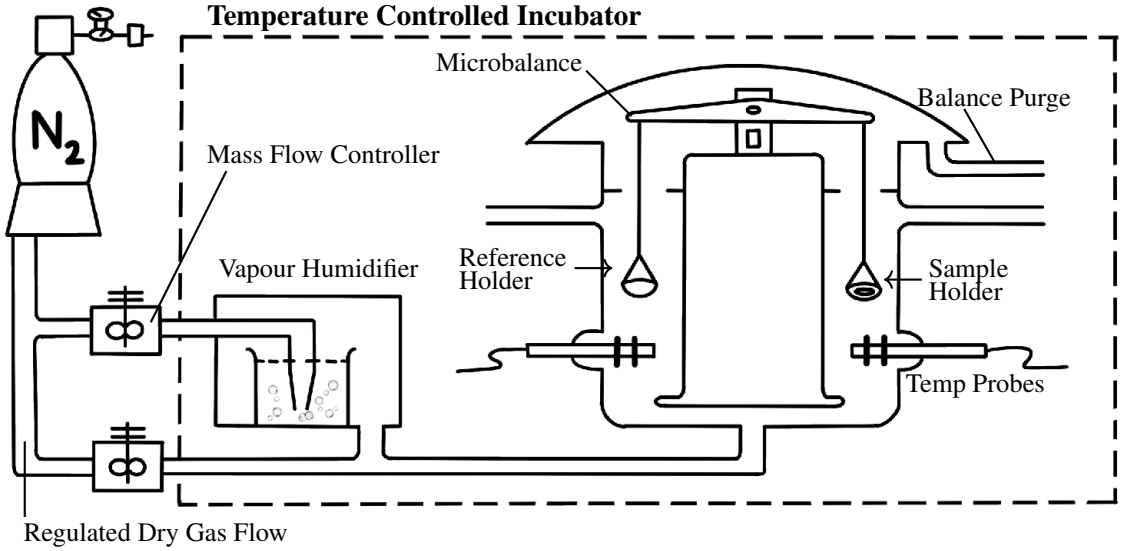

Figure 4.3: Schematic of a Dynamic Vapor Sorption (DVS) system (adapted from [79]) showing the controlled mixing of dry and saturated air to reach the desired relative humidity along with symmetric reference compensation.

4.1.3 Data collection and analysis

The sorption data collected is processed to generate water vapor sorption isotherms, which depict the relationship between equilibrium moisture content and relative humidity at a fixed temperature and atmospheric pressure. The data acquisition software further ensures continuous and sensitive measurement of the mass exchange between the specimens and the environment in the DVS chamber. This is particularly important for materials containing supplementary cementitious materials (SCMs) like slag or silica fume. Moreover, through DVS measurement, it captures transient sorption behavior, offering insight into the non-Fickian diffusion often observed in cement-based materials. This feature allows for the evaluation of sorption rates and capacity across different pore structures, advancing our understanding of how water interacts with hydrated phases [95, 104].

The system's sensitivity to these conditions requires precise calibration before each test, which helps to guarantee the reliability of measurements and ensures that results are consistent and reproducible. Research has shown that variations of relative humidity can significantly influence moisture sorption behavior in cement-based materials, underscoring the importance of precision in these experiments [12, 58, 145]. To mitigate the effects of minor oscillations that may occur during measurement, an initial series of tests is conducted to fine-tune the experimental setup, followed by additional trials using multiple samples. This approach ensures that results more closely resemble real-world conditions,

providing a better understanding of mass exchange behavior in concrete.

4.2 Materials and sample preparation

For this study, Normsand (DIN EN 196-1) and CEM I cement were chosen for the concrete samples to ensure material purity and consistency in the experimental results, as summarized in Table 4.1. CEM I, containing approximately 95% Portland clinker, was chosen to provide a reliable baseline for analyzing moisture transport and sorption characteristics without interference from supplementary materials or fillers. The high clinker content in CEM I minimizes variability often seen with other cement types, making it ideal for studying the fundamental hydration and sorption behaviors of cement-based materials. This purity ensures that any observed moisture-related properties reflect the inherent characteristics of cement hydration and pore structure development, free from the effects of additional compounds.

Property	**Normsand (DIN EN 196-1)**	**CEM I Cement**
Standard	DIN EN 196-1	EN 197-1
Main Composition	Pure quartz sand	95% Portland clinker
Grain Size Distribution	0.08 - 2.0 mm	Fine powder
Specific Surface Area	Not specified	Typically 3000-3500 cm^2/g
Color	Light beige	Gray
Additives	None	None (up to 5% minor constituents)
Purity	99% SiO_2	High purity, no supplementary cementitious materials
Application	Standardized testing for cement	Concrete and mortar production

Table 4.1: Main characteristics of Normsand (DIN EN 196-1) and CEM I cement.

The water-to-cement ratio (w/c) was set to 0.4, a widely recognized value in concrete research that balances workability and durability, providing optimal conditions for hydration while minimizing excess pore water. This ratio aligns with benchmarks in similar studies, including those by Gawin et al. [62], which allows for meaningful comparisons with the established concrete model. At a 0.4 w/c ratio, the mix retains sufficient moisture for full hydration without introducing excess free water that might affect results by altering pore

size distribution or promoting capillary condensation. The materials and preparation methods were selected with a strong focus on purity, consistency, and practical relevance.

The preparation of samples involved a standardized mixing process to ensure uniform distribution of cement and sand particles, essential for reliable and consistent results in moisture-related testing. In the beginning, CEM I cement and Normsand were mixed with water at a 0.4 w/c ratio under controlled conditions to avoid introducing air voids or other inconsistencies. After mixing, the fresh concrete was cast into standardized molds, compacted to remove any entrapped air, and covered to prevent moisture loss during the initial setting phase. Once set, samples were placed in a temperature- and humidity-controlled chamber to simulate ideal hydration conditions. This curing process ensures that the cement paste develops a well-defined pore structure, for accurate DVS measurements and for replicating the natural curing environment of concrete in structural applications [95, 132].

After mixing, the curing phase lasted for 3 days, allowing the concrete to attain its initial rigid form. Throughout this phase, samples were stored in a controlled environment maintained at 20°C and 94% relative humidity. These conditions align with established concrete curing standards designed to promote optimal hydration. The high humidity prevents premature drying and shrinkage, preserving the intended pore structure and minimizing any potential effects on moisture transport properties that could arise from early surface evaporation. During the curing period, samples were monitored at 30-minute intervals using a high-sensitivity scale within the DVS chamber.

4.3 Preliminary tests and final setup

Before conducting the final experiments, initial tests are carried out to calibrate the experimental setup and ensure that the DVS machine is functioning optimally. These tests involve trial runs with sample materials to fine-tune the experimental conditions and validate the machine's accuracy. The initial results from these tests will be used to adjust the parameters of the final tests, ensuring that the data collected is suitable for both experimental analysis and numerical modeling.

4.3.1 Preliminary analysis of mass reduction in fresh concrete samples at different relative humidity levels

This study analyzes the mass loss behavior of two fresh concrete samples exposed to different relative humidity conditions in a DVS machine. The samples were exposed to relative humidity of 65% and 94% to assess the impact of environmental humidity on the initial

hydration and evaporation processes in concrete. It is important to note that the DVS machine was set to a maximum of 94% instead of 100% due to the risk of air condensation at the specimen surface at full saturation. Such condensation could lead to water accumulating on the surface of the specimen or on the chamber walls, which would interfere with the mass scale and result in unreliable data. The relative humidity of $\Phi = 94\%$ setting closely simulates high-humidity conditions without risking condensation, thereby allowing for accurate and consistent measurements of mass changes.

As part of the standard procedure, an empty sample (reference point) was included in both cases to account for baseline mass fluctuations within the chamber environment. This reference sample, represented by the blue line in Figure 4.4, allows for differentiation between the inherent mass changes in the concrete samples and any external influences within the DVS chamber.

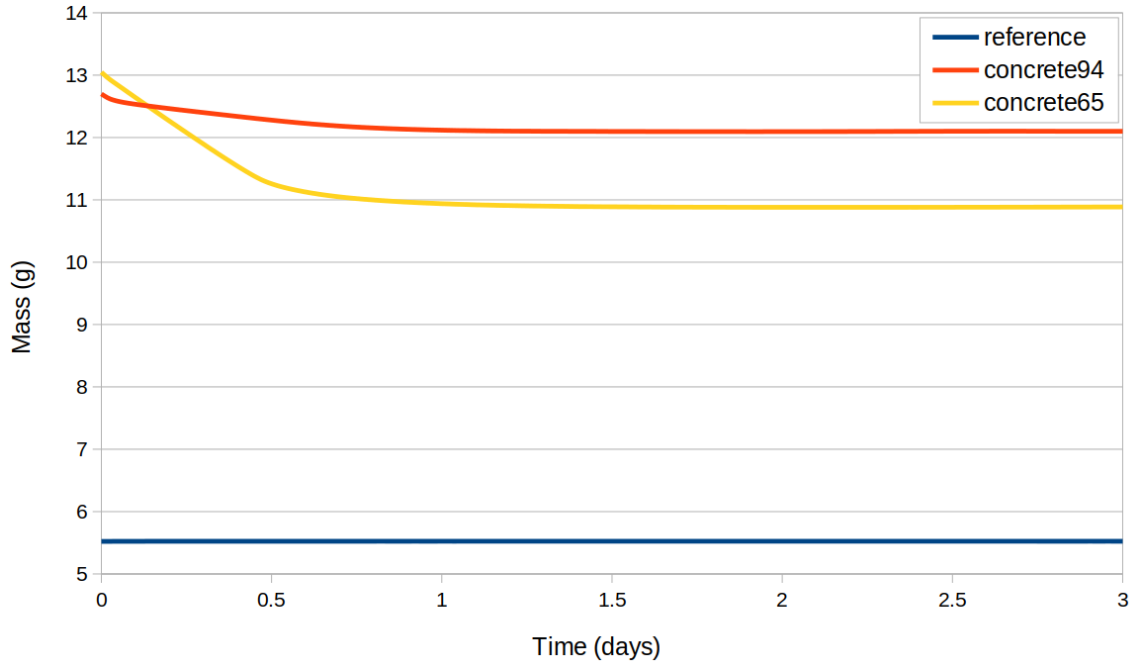

Figure 4.4: Time-dependent mass loss of fresh concrete at 65% and 94% relative humidity, including empty reference measurement (blue line) from DVS testing.

The mass changes of two fresh concrete samples subjected to different relative humidity conditions in the DVS chamber were monitored over three days, as shown in Figure 4.4. The only difference between the samples was the relative humidity setting, one at 65% and the other at 94% ($\Phi = 0.65$ and $\Phi = 0.94$, respectively). The sample exposed to 65% relative humidity exhibited a rapid mass loss during the initial 1000 minutes, stabilizing around 11.0 grams. In contrast, the sample maintained at 94% relative humidity showed a slower and more gradual reduction in mass, reaching equilibrium near 12.0 grams. The

data in Figure 4.4 clearly illustrate the influence of relative humidity on moisture loss. The pronounced early mass loss at 65% humidity reflects an increased evaporation rate driven by the lower ambient humidity. Conversely, the higher humidity environment ($\Phi = 94\%$) effectively reduced the evaporation rate, promoting moisture retention within the concrete. This controlled environment better supports the hydration process by limiting rapid water loss, which is critical for cement hydration kinetics. These observations highlight the significant role of relative humidity in regulating early-stage hydration and moisture dynamics in fresh concrete, emphasizing the need to carefully control environmental conditions to optimize concrete curing.

Conclusion

This preliminary test demonstrates the significant influence of relative humidity on the mass reduction and hydration behavior of fresh concrete samples. The data indicate that a higher relative humidity level (94%) within the DVS chamber helps to retain moisture within the concrete matrix, reducing evaporation and allowing more water to remain available for the hydration process. This moisture retention is essential for supporting ongoing hydration reactions, which contribute to the strength and durability of the material in its early stages. In laboratory settings, samples for evaluating early-stage concrete hardening are typically kept at or near 100% relative humidity. This high humidity level minimizes the risk of crack propagation by ensuring sufficient moisture for consistent and complete hydration, preventing the development of internal stresses that may arise from rapid drying.

In practical construction environments, similar precautions are taken to preserve high humidity levels during early hardening. After concrete is poured into walls or onto ground surfaces, protective measures such as formwork boards or plastic sheeting are used to maintain a near-100% relative humidity around the material. These coverings prevent premature moisture loss, creating conditions that allow the concrete to develop strength without the risk of drying-induced cracks. Based on these observations, the 94% setting will be used in subsequent tests to replicate high-humidity conditions that not only reflect controlled laboratory environments but also resemble optimal real-world curing conditions during the critical early hardening phase of concrete.

4.3.2 Preliminary analysis of mass reduction in fresh concrete with different sample sizes

To investigate the influence of specimen size on moisture exchange over the initial 3 days of curing, a controlled experiment was conducted on four fresh concrete samples with varying initial masses (10g, 20g, 30g, and 40g). This study builds upon previous findings, which highlighted the importance of maintaining high ambient humidity to ensure

consistent hydration behavior. The primary objective is to identify an optimal specimen size for future mass exchange analyses in maturing concrete, particularly with respect to evaporation-driven water loss. The experiment was carried out under stable environmental conditions, relative humidity at $\Phi = 94\%$, temperature of 20°C and atmospheric pressure, previously determined to minimize condensation and ensure data reliability. Real-time mass tracking at 30-minute intervals was employed using a DVS system to capture detailed mass loss profiles for each specimen. An empty reference container was included to account for baseline fluctuations within the chamber, enabling isolation of the hydration and evaporation effects occurring in the concrete samples. By comparing the mass reduction and evaporation trends across different sample sizes, this preliminary investigation provides insights into how geometric scaling influences moisture loss

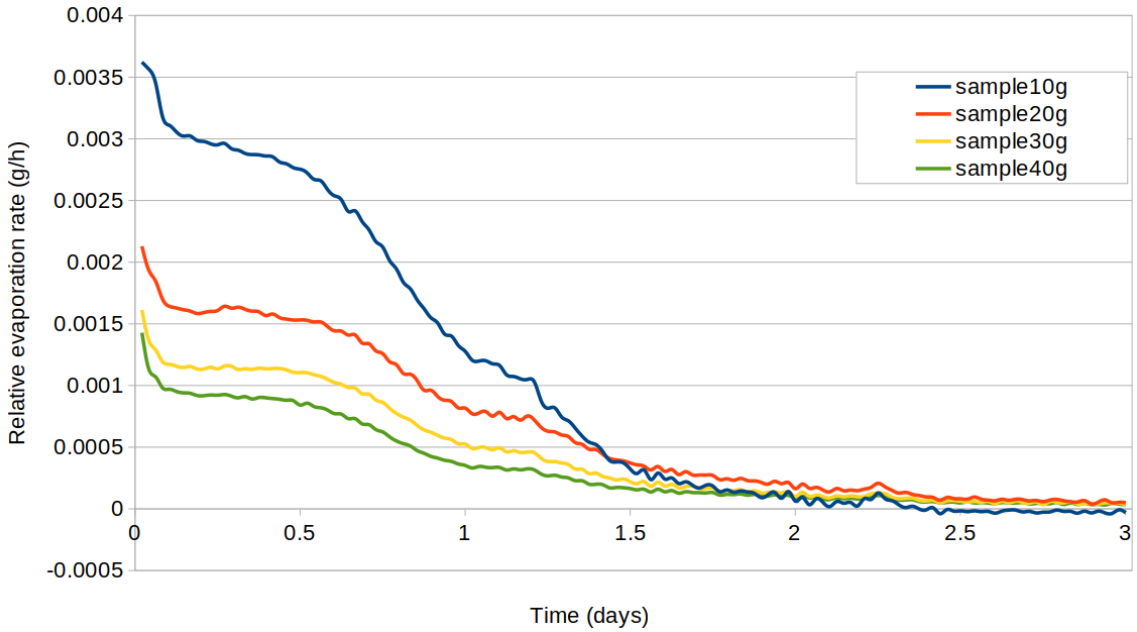

Figure 4.5: Effect of sample size on relative evaporation rate in the first 3 days.

Figure 4.5 illustrates the relative evaporation rate, defined as the mass loss normalized by the initial sample mass, highlighting how evaporation efficiency varies with specimen size. Smaller samples (10 g and 20 g) exhibited significantly higher relative evaporation rates, especially during the early phase. This elevated rate results from their larger surface-area-to-volume ratios, which facilitate rapid moisture exchange with the environment. However, this rate decreases over time as surface water is depleted and internal diffusion becomes the controlling factor.

In contrast, Figure 4.6 presents the absolute evaporation rate, representing total mass loss per hour. Larger specimens (30 g and 40 g) initially showed the highest absolute evaporation values due to their greater overall water content. Yet, when normalized by their mass,

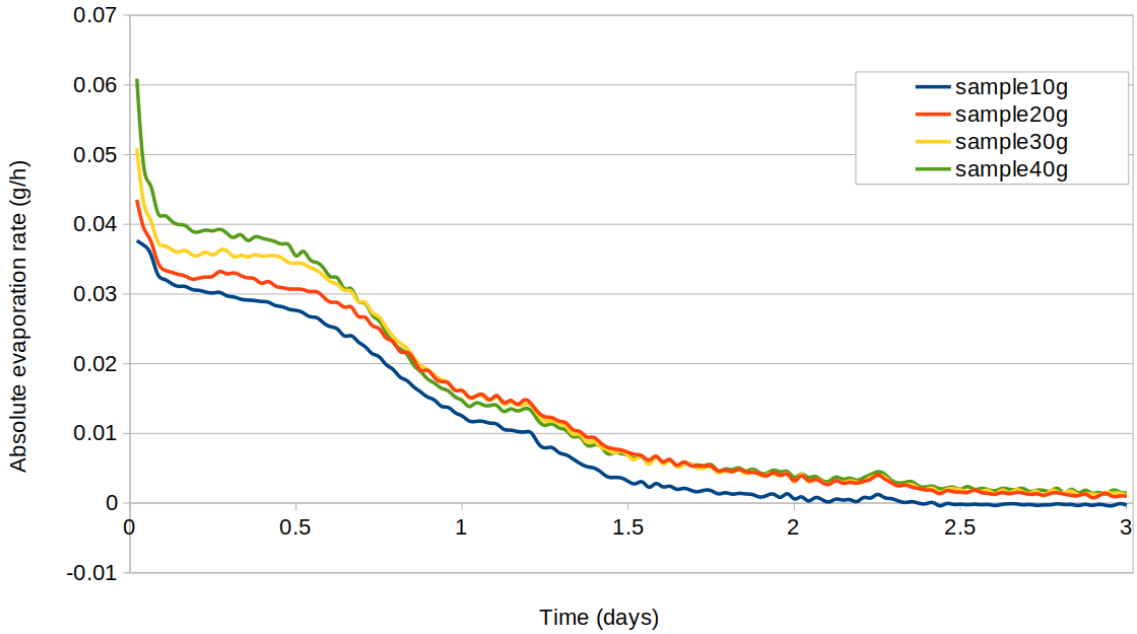

Figure 4.6: Effect of sample size on absolute evaporation rate in the first 3 days.

their relative evaporation rates remain comparatively low, demonstrating more effective moisture retention. All specimens exhibited a continuous mass reduction throughout the three-day experiment, confirming ongoing moisture loss by evaporation. Notably, a clear distinction emerged between smaller and larger samples. This behavior is primarily explained by differences in surface-area-to-volume ratio, smaller samples have a relatively larger surface exposed to air, accelerating evaporation, whereas the compact geometry of larger samples limits moisture loss.

Conclusion and final setup

The experimental investigation into mass change and evaporation rates across concrete samples of varying initial masses (10 g, 20 g, 30 g, and 40 g) highlights the critical influence of sample size on early hydration dynamics. Larger specimens, particularly those weighing 30 g and 40 g, exhibit evaporation behavior that more closely mirrors real-world curing conditions due to their reduced surface-area-to-volume ratios. This slower, more controlled moisture loss supports sustained hydration and helps to prevent premature drying and associated risks such as surface cracking. Among the tested samples, the 40 g specimen stands out as the most representative model for future studies. Its evaporation profile balances initial moisture release with prolonged retention, effectively simulating the drying conditions typical of larger-scale concrete applications. This finding is pivotal

for designing experiments that aim to capture hydration and evaporation processes under conditions relevant to practical construction.

Building on these insights, the final experimental setup will involve simultaneous monitoring of eight identical 40 g specimens alongside an empty reference to account for environmental baseline variations. Recognizing that evaporation markedly slows after approximately 48 hours, the focus will be placed on this critical early period, which strongly influences the long-term performance of concrete. By concentrating on this window and employing the 40 g sample size, we expect to obtain robust, realistic data that enhance understanding of moisture transport during the formative stages of concrete curing.

5 NUMERICAL TREATMENT

This chapter presents the numerical methods employed to solve the Initial-Boundary Value Problem (IBVP) in chapter 3. The Finite Element Method (FEM) is widely adopted for such problems, operating within a time-stepping finite-difference scheme to solve systems of partial differential equations (PDEs). The governing equations are first reformulated into their weak integral form, followed by spatial discretization using FEM and temporal discretization via the finite difference method. Finally, a numerical scheme is proposed to efficiently solve the resulting discrete system.

In contrast to traditional porous mechanics applications, where nonlinear behavior often leads to differential-algebraic equations (DAEs) that combine PDEs for global balance laws with additional algebraic constraints, fresh concrete modeling presents unique challenges due to its continuously evolving material properties. Efficient numerical strategies are essential for solving these DAE systems. Various approaches have been explored in the literature, including those by Ehlers [43, 46, 51, 52] and Schrefler et al. [124, 127, 128].

In this research, we employ FEniCSx, a powerful open-source platform for solving differential equations using FEM. Designed for high-performance computing, it automates code generation, enables adaptive mesh refinement, and provides efficient solvers. This flexibility makes it particularly suited for nonlinear multiphysics problems, such as the evolving behavior of fresh concrete, allowing efficient formulation and solution of complex governing equations. The first part of this chapter explores the FEM-based numerical implementation of fresh concrete modeling, highlighting FEniCSx's efficiency in handling materials nonlinearities. This is followed by a discussion on parameter identification. The aim was to calibrate the evaporation model from chapter 3 using the experimental data presented in chapter 4. Parameter identification was performed through nonlinear least-squares optimization, improving model accuracy and robustness by fitting the model to the observed data [107, 129, 134].

5.1 Finite Element Method

The Finite Element Method is a powerful tool for solving complex engineering problems across disciplines. With the rapid advancement of computational power, FEM has become essential for handling increasingly nonlinear and intricate simulations [4]. However, FEM solutions remain approximations of Initial-Boundary Value Problems, where accuracy depends on factors such as mesh discretization, material modeling, and numerical stability. Ensuring numerical convergence is crucial to obtaining reliable results. For a comprehensive discussion on FEM and nonlinear continuum mechanics, the reader is referred to Bathe [6], Braess [19] and Hughes [83].

5.1.1 Weak formulation

Using the method of weighted residuals, the weak form of the governing equations is derived. This includes the mixture's momentum balance (3.12), the mass balances for the solid (3.9a), liquid (3.9b) and gas phases (3.9c), as well as the mixture's enthalpy balance (3.16). Trial solutions with shape functions are introduced, leading to residuals that are weighted by test functions and enforced to vanish. This process converts the original differential equations into an integral form that is mathematically consistent and less restrictive. Assuming thermal equilibrium and applying Darcy's law for fluid flow, the problem is reduced to five independent variables

$$\mathcal{U} = \mathcal{U}(\mathbf{x},t) = \left\{\mathbf{u}_S, n^S, p^C, p^G, \Theta\right\}. \tag{5.1}$$

Following the Bubnov-Galerkin approach, the weak formulations are derived by multiplying the governing strong forms with appropriate test functions $\delta\mathbf{u}_S, \delta n^S, \delta p^C, \delta p^G, \delta\Theta$. Integrating in the spatial domain V, applying integration by parts and utilizing the divergence theorem, we obtain weak formulations governing multiphase material.

- Mass balance of solid:

$$\int_V \left(\rho^{SR}(n^S)'_S + n^S(\rho^{SR})'_S + n^S\rho^{SR}\operatorname{div}\mathbf{x}'_S - \hat{\rho}^S\right)\,\delta n^S\,\mathrm{dv} = 0 \tag{5.2}$$

- Mass balance of liquid:

$$\begin{aligned}
&\int_V \left(\rho^{LR}(n^L)'_S + n^L(\rho^{LR})'_S + n^L\rho^{LR}\operatorname{div}\mathbf{x}'_S - \hat{\rho}^L\right)\,\delta p^C\,\mathrm{dv}\\
&+\int_V \rho^{LR}\left(\frac{k^{rL}k\,\mathbf{I}}{\mu^L}\,\left(\operatorname{grad}p^G - \operatorname{grad}p^C - \rho^{LR}\mathbf{b} - \frac{p^C}{s^L}\operatorname{grad}s^L\right)\right)\cdot\operatorname{grad}\delta p^C\,\mathrm{dv}\\
&+\int_{A_C^q} \tilde{\mathrm{w}}_{LS}\,\delta p^C\,\mathrm{da} = 0
\end{aligned} \tag{5.3}$$

- Mass balance of gas:

$$\begin{aligned}
&\int_V \left(\rho^{GR}(n^G)'_S + n^G(\rho^{GR})'_S + n^G\rho^{GR}\operatorname{div}\mathbf{x}'_S - \hat{\rho}^G\right)\,\delta p^G\,\mathrm{dv}\\
&+\int_V \rho^{GR}\left(\frac{k^{rG}k\,\mathbf{I}}{\mu^G}\,\left(\operatorname{grad}p^G - \rho^{GR}\mathbf{b}\right)\right)\cdot\operatorname{grad}\delta p^G\,\mathrm{dv} + \int_{A_G^q}\tilde{\mathrm{w}}_{GS}\,\delta p^G\,\mathrm{da} = 0
\end{aligned} \tag{5.4}$$

- Momentum balance of mixture:

$$\begin{aligned}
&\int_V (\mathbf{T}_E^S - p^{FR}\mathbf{I}) : \operatorname{grad}\delta\mathbf{u}_S \,\mathrm{dv} - \int_V (n^S\rho^{SR} + n^L\rho^{LR} + n^G\rho^{GR})\,\mathbf{g}\cdot\delta\mathbf{u}_S \,\mathrm{dv} \\
&- \int_{A_u^q} \bar{\mathbf{t}}\cdot\delta\mathbf{u}_S \,\mathrm{da} = \mathbf{0}
\end{aligned} \tag{5.5}$$

- Enthalpy balance of mixture:

$$\begin{aligned}
&\int_V (\rho C_p)\,(\Theta)_S'\,\delta\theta \,\mathrm{dv} - \int_V (\mathbf{T}_E^S : \mathbf{L}_S)\,\delta\theta \,\mathrm{dv} \\
&- \int_V \left(\rho^{LR} C_p^L \,\frac{k^{rL} k\,\mathbf{I}}{\mu^L}\,\left(\operatorname{grad} p^L - \rho^{LR}\,\mathbf{b} - \frac{p^C}{s^L}\operatorname{grad} s^L\right)\right)\cdot\operatorname{grad}\Theta\,\delta\theta \,\mathrm{dv} \\
&- \int_V \left(\rho^{GR} C_p^G \,\frac{k^{rG} k\,\mathbf{I}}{\mu^G}\,\left(\operatorname{grad} p^G - \rho^{GR}\,\mathbf{b}\right)\right)\cdot\operatorname{grad}\Theta\,\delta\theta \,\mathrm{dv} \\
&- \int_V \left((p^S)_S' + (p^L)_S' + (p^G)_S'\right)\,\delta\theta \,\mathrm{dv} + \int_V (\lambda_{\mathrm{eff}}\operatorname{grad}\Theta)\cdot\operatorname{grad}\delta\theta \,\mathrm{dv} \\
&- \int_{A_\Theta^q} \tilde{\mathrm{q}}^\Theta\,\delta\theta \,\mathrm{da} - \int_V (\hat{\rho}^S \Delta h_{\mathrm{hydr}} - \hat{\rho}^G \Delta h_{\mathrm{evap}})\,\delta\theta \,\mathrm{dv} = 0
\end{aligned} \tag{5.6}$$

To fully specify the model, it is necessary to define the initial and boundary conditions. The initial conditions describe the distribution of the primary variables across the domain V and its boundary A at the initial time $t = 0$, ensuring a well-posed problem formulation. These conditions are expressed as

$$n^S = n_0^S, \quad p^C = p_0^C, \quad p^G = p_0^G, \quad \mathbf{u}_S = \mathbf{u}_{S0}, \quad \Theta = \Theta_0. \tag{5.7}$$

Some governing equations give rise to surface integrals, which are Neumann boundary conditions. As a result, the boundary $A = \partial V$ is partitioned accordingly

$$\begin{aligned}
A &= A_{\mathbf{u}_S} \cup A_{\mathbf{t}} \qquad \text{with} \qquad A_{\mathbf{u}_S} \cap A_{\mathbf{t}} = \varnothing, \\
A &= A_{p_c} \cup A_{q_c} \qquad \text{with} \qquad A_{p_c} \cap A_{q_c} = \varnothing, \\
A &= A_{p_g} \cup A_{q_g} \qquad \text{with} \qquad A_{p_g} \cap A_{q_g} = \varnothing, \\
A &= A_{n_s} \cup A_{\upsilon} \qquad \text{with} \qquad A_{n_s} \cap A_{\upsilon} = \varnothing, \\
A &= A_\Theta \cup A_{q_\Theta} \qquad \text{with} \qquad A_\Theta \cap A_{q_\Theta} = \varnothing.
\end{aligned} \tag{5.8}$$

Here, the boundary segments $A_{\mathbf{u}_S}$, A_{p_c}, A_{p_g}, A_{n_s}, and A_Θ correspond to Dirichlet boundaries, where fixed values are prescribed for the primary variables. Specifically, the solid

mass balance is governed by the Dirichlet boundary A_{n_s}, ensuring a prescribed value for n^S. Similarly, fixed displacements $\mathbf{u}_S$ and temperature Θ are applied on the boundaries $A_{\mathbf{u}_S}$ and A_Θ, respectively. On the other hand, the boundaries $A_\mathbf{t}$, A_{q_c}, A_{q_g}, A_υ, and A_{q_Θ} denote the Neumann boundaries, where fluxes are specified. For the solid mass balance, only a Dirichlet boundary condition is prescribed on A_{n_s}. Since the governing equation is a first-order differential equation, no Neumann boundary condition naturally arises in this case. This comprehensive decomposition of the boundary conditions ensures a well-posed problem formulation while accommodating the complex interactions between the primary variables. For the momentum balance, the external traction vector applied on the Neumann boundary $A_\mathbf{t}$ is given by

$$\bar{\mathbf{t}} = (\mathbf{T}_E^S - p^{FR}\mathbf{I}) \cdot \mathbf{n}, \tag{5.9}$$

where $\mathbf{n}$ denotes the outward unit normal vector to the surface. Similarly, the Neumann boundary conditions for mass transfer in the fluid phases are expressed as

$$\tilde{\mathrm{w}}_{LS} = n^L \rho^{LR} \mathbf{w}_{LS} \cdot \mathbf{n}, \quad \tilde{\mathrm{w}}_{GS} = n^G \rho^{GR} \mathbf{w}_{GS} \cdot \mathbf{n}, \tag{5.10}$$

where $\tilde{\mathrm{w}}_{LS}$ and $\tilde{\mathrm{w}}_{GS}$ represent the liquid and gas mass effluxes on the Neumann boundaries A_{q_c} and A_{q_g}, respectively. To account for heat flux interactions at the thermal boundary A_{q_Θ}, a Robin boundary condition is imposed to model convective heat exchange with the surroundings

$$-\mathbf{q} \cdot \mathbf{n} = h_\Theta (\Theta - \Theta_\infty), \tag{5.11}$$

where h_Θ is the convective heat transfer coefficient, and Θ_∞ denotes the ambient temperature. This formulation ensures that the heat flux accurately accounts for thermal convection effects at the boundary. Together, these boundary conditions provide a comprehensive and consistent framework for governing the interactions of mass, momentum, and enthalpy within the system. This ensures a physically accurate representation of the modeled material behavior, maintaining the integrity of the numerical solution. To proceed with the numerical formulation, it is necessary to select an appropriate ansatz for the trial functions of the primary variables

$$\left\{\mathbf{u}_S, p^C, p^G, n^S, \Theta\right\},$$

and the corresponding test functions

$$\left\{\delta\mathbf{u}_S, \delta p^C, \delta p^G, \delta n^S, \delta\Theta\right\}.$$

These functions are chosen from the Sobolev space $\mathcal{H}^1(V)$, ensuring sufficient regularity for the weak formulation

$$\mathcal{S}_{\mathbf{u}_S}(t) = \left\{\mathbf{u}_S \in \mathcal{H}^1(V)^D \;:\; \mathbf{u}_S(\mathbf{x}) = \bar{\mathbf{u}}_S(\mathbf{x},t) \text{ on } A_{\mathbf{u}_S}\right\}, \tag{5.12}$$

$$\mathcal{S}_{p_c}(t) = \left\{p^C \in \mathcal{H}^1(V) \;:\; p^C(\mathbf{x}) = \bar{p}^C(\mathbf{x},t) \text{ on } A_{p_c}\right\}, \tag{5.13}$$

$$\mathcal{S}_{p_g}(t) = \left\{p^G \in \mathcal{H}^1(V) \;:\; p^G(\mathbf{x}) = \bar{p}^G(\mathbf{x},t) \text{ on } A_{p_g}\right\}, \tag{5.14}$$

$$\mathcal{S}_{n^S}(t) = \left\{n^S \in \mathcal{H}^1(V) \;:\; n^S(\mathbf{x}) = \bar{n}^S(\mathbf{x},t) \text{ on } A_{n_s}\right\}, \tag{5.15}$$

$$\mathcal{S}_\Theta(t) = \left\{ \Theta \in \mathcal{H}^1(V) \quad : \quad \Theta(\mathbf{x}) = \bar{\Theta}(\mathbf{x},t) \text{ on } A_\Theta \right\}, \tag{5.16}$$

$$\mathcal{T}_{\mathbf{u}_S} = \left\{ \delta\mathbf{u}_S \in \mathcal{H}^1(V)^D : \quad \delta\mathbf{u}_S(\mathbf{x}) = \mathbf{0} \text{ on } A_{\mathbf{u}_S} \right\}, \tag{5.17}$$

$$\mathcal{T}_{p_c} = \left\{ \delta p^C \in \mathcal{H}^1(V) \quad : \quad \delta p^C(\mathbf{x}) = 0 \text{ on } A_{p_c} \right\}, \tag{5.18}$$

$$\mathcal{T}_{p_g} = \left\{ \delta p^G \in \mathcal{H}^1(V) \quad : \quad \delta p^G(\mathbf{x}) = 0 \text{ on } A_{p_g} \right\}, \tag{5.19}$$

$$\mathcal{T}_{n^S} = \left\{ \delta n^S \in \mathcal{H}^1(V) \quad : \quad \delta n^S(\mathbf{x}) = 0 \text{ on } A_{n^S} \right\}, \tag{5.20}$$

$$\mathcal{T}_\Theta = \left\{ \delta\Theta \in \mathcal{H}^1(V) \quad : \quad \delta\Theta(\mathbf{x}) = 0 \text{ on } A_\Theta \right\}. \tag{5.21}$$

In this monograph, we consider problems in 2D and 3D space, corresponding to $D \in \{2,3\}$ depending on the spatial dimension. To provide a concise and clear representation, the variational problem is formulated using the functional $\boldsymbol{\mathcal{G}}_\mathbf{u}$, which encompasses the weak forms of equations (5.2) to (5.6). The vector of unknowns $\mathbf{u}$ contains all the field variables to be solved

$$\boldsymbol{\mathcal{G}}_\mathbf{u} = \begin{bmatrix} \mathcal{G}_{\mathbf{u}_S} \\ \mathcal{G}_{p_c} \\ \mathcal{G}_{p_g} \\ \mathcal{G}_{n^S} \\ \mathcal{G}_\Theta \end{bmatrix}, \quad \mathbf{u} = \begin{bmatrix} \mathbf{u}_S \\ p^C \\ p^G \\ n^S \\ \Theta \end{bmatrix}, \quad \delta\mathbf{u} = \begin{bmatrix} \delta\mathbf{u}_S \\ \delta p^C \\ \delta p^G \\ \delta n^S \\ \delta\Theta \end{bmatrix}, \quad \mathbf{u}'_S = \begin{bmatrix} (\mathbf{u}_S)'_S \\ (p^C)'_S \\ (p^G)'_S \\ (n^S)'_S \\ (\Theta)'_S \end{bmatrix}, \quad \mathbf{u}_0 = \begin{bmatrix} \mathbf{u}_{S0} \\ p^C_0 \\ p^G_0 \\ n^S_0 \\ \Theta_0 \end{bmatrix}. \tag{5.22}$$

Here, the vector $\delta\mathbf{u}$ comprises the test functions, while the vector $\mathbf{u}'_S$ denotes the time derivatives of the unknowns, which will be discretized using an appropriate time integration scheme. The initial values of the unknowns are represented by the vector $\mathbf{u}_0 = \mathbf{u}(\mathbf{x},t_0)$. With these definitions, the variational problem corresponding to equations (5.2) to (5.6) can be expressed in a generalized form as

$$\text{Find} \quad \mathbf{u} \in \mathcal{S}_\mathbf{u}(t) \quad \text{such that} \quad \boldsymbol{\mathcal{G}}_\mathbf{u}(\mathbf{u},\delta\mathbf{u}) = \mathbf{0} \quad \forall \quad \delta\mathbf{u} \in \mathcal{T}_\mathbf{u}, t \in \left[t_0, T\right], \tag{5.23}$$

Here, the space $\mathcal{S}_\mathbf{u}(t)$ is defined as the combination of the trial spaces $\mathcal{S}_{\mathbf{u}_S}$, $\mathcal{S}_{p_c}$, $\mathcal{S}_{p_g}$, $\mathcal{S}_{n_S}$, and $\mathcal{S}_\Theta$, corresponding to the primary variables of the problem. Similarly, the space $\mathcal{T}_\mathbf{u}$ is formed by the test spaces $\mathcal{T}_{\mathbf{u}_S}$, $\mathcal{T}_{p_c}$, $\mathcal{T}_{p_g}$, $\mathcal{T}_{n_s}$, and $\mathcal{T}_\Theta$. These function spaces ensure the consistency of the weak formulation. The time interval under consideration is denoted by $\left[t_0 = 0, T\right]$. In the next step, we will precisely define the function spaces $\mathcal{S}_\mathbf{u}$ and $\mathcal{T}_\mathbf{u}$ to ensure the well-posedness of the variational problem.

5.1.2 Spatial discretization

The considered domain V is approximated by a spatially discretized domain V^h, which consists of a finite number of non-overlapping subdomains V_e, known as finite elements. These elements collectively form the finite element mesh

$$V \approx V^h = \bigcup_{e=1}^{N_e} V_e. \tag{5.24}$$

Each finite element is defined by a set of N_n nodes and the complete mesh contains N_N nodes in total. The trial and test functions are defined on the reference element, introducing the geometry transformation and local coordinates ξ. The mapping between the local coordinates ξ and the global coordinates $\mathbf{x}$ is given by

$$\mathbf{x}(\xi) = \sum_{i=1}^{N_n} \phi^i_{\text{geo}}(\xi)\mathbf{x}_i, \tag{5.25}$$

where $\mathbf{x}(\xi)$ represents the position in global coordinates, and ϕ^i_{geo} are the geometry transformation basis functions. Here, the same quadratic basis functions are used for both the geometry transformation and solid displacements $\mathbf{u}_S$, ensuring isoparametric mapping for solid displacements. For the other primary variables, a superparametric mapping is applied, where the approximation order for the geometry is higher than that of the primary variables. For further details on the numerical integration scheme used in the reference element, including coordinate transformations and Gauss quadrature, see Stroud [133], Zienkiewicz and Taylor [149].

Furthermore, the discretization enables the transformation of the continuous trial and test spaces $\mathcal{S}_\mathbf{u}$ and $\mathcal{T}_\mathbf{u}$ into their discrete counterparts, denoted as $\mathcal{S}^h_\mathbf{u}$ and $\mathcal{T}^h_\mathbf{u}$, respectively. Accordingly, the discrete trial functions can be expressed as

$$\begin{aligned}
\mathbf{u}_S(\mathbf{x},t) \approx \mathbf{u}^h_S(\mathbf{x},t) &= \sum_{j=1}^{N_{\mathbf{u}_S}} N^j_{\mathbf{u}_S}(\mathbf{x})\mathbf{u}^j_S(t) \quad \in \mathcal{S}^h_{\mathbf{u}_S}(t),\\
p^C(\mathbf{x},t) \approx p^{C,h}(\mathbf{x},t) &= \sum_{j=1}^{N_{pc}} N^j_{p_c}(\mathbf{x})p^{C,j}(t) \in \mathcal{S}^h_{p_c}(t),\\
p^G(\mathbf{x},t) \approx p^{G,h}(\mathbf{x},t) &= \sum_{j=1}^{N_{pg}} N^j_{p_g}(\mathbf{x})p^{G,j}(t) \in \mathcal{S}^h_{p_g}(t),\\
n^S(\mathbf{x},t) \approx n^{S,h}(\mathbf{x},t) &= \sum_{j=1}^{N_{n_s}} N^j_{n_s}(\mathbf{x})n^{S,j}(t) \in \mathcal{S}^h_{n_S}(t),\\
\Theta(\mathbf{x},t) \approx \Theta^h(\mathbf{x},t) &= \sum_{j=1}^{N_\Theta} N^j_\Theta(\mathbf{x})\Theta^j(t) \quad \in \mathcal{S}^h_\Theta(t).
\end{aligned} \tag{5.26}$$

Similarly, the discrete test functions are given by

$$\begin{aligned}
\delta\mathbf{u}_S(\mathbf{x}) \approx \delta\mathbf{u}^h_S(\mathbf{x}) &= \sum_{j=1}^{N_{\mathbf{u}_S}} M^j_{\mathbf{u}_S}(\mathbf{x})\delta\mathbf{u}^j_S \quad \in \mathcal{T}^h_{\mathbf{u}_S},\\
\delta p^C(\mathbf{x}) \approx \delta p^{C,h}(\mathbf{x}) &= \sum_{j=1}^{N_{pc}} M^j_{p_c}(\mathbf{x})\delta p^{C,j} \in \mathcal{T}^h_{p_c},
\end{aligned}$$

$$\delta p^G(\mathbf{x}) \approx \delta p^{G,h}(\mathbf{x}) = \sum_{j=1}^{N_{pg}} M_{p_g}^j(\mathbf{x}) \delta p^{G,j} \in \mathcal{T}_{p_g}^h, \tag{5.27}$$

$$\delta n^S(\mathbf{x}) \approx \delta n^{S,h}(\mathbf{x}) = \sum_{j=1}^{N_{ns}} M_{n_s}^j(\mathbf{x}) \delta n^{S,j} \in \mathcal{T}_{n_s}^h,$$

$$\delta \Theta(\mathbf{x}) \approx \delta \Theta^h(\mathbf{x}) = \sum_{j=1}^{N_\Theta} M_\Theta^j(\mathbf{x}) \delta \Theta^j \in \mathcal{T}_\Theta^h.$$

In this context, the set $\left\{N_{\mathbf{u}_S}, N_{p_c}, N_{p_g}, N_{n_s}, N_\Theta\right\}$ represents the number of nodes used for approximating the corresponding field variables. The quantity $\left\{N_\alpha\right\} \leq N_N$ may vary depending on the required accuracy of the approximation. The basis functions for the trial functions are denoted by $\left\{N_{\mathbf{u}_S}^j, N_{p_c}^j, N_{p_g}^j, N n_s{}^j, N_\Theta^j\right\}$, while the time-dependent nodal degrees of freedom (DOF) are given by $\left\{\mathbf{u}_S^j, p^{C,j}, p^{G,j}, n^{S,j}, \Theta^j\right\}$. Correspondingly, the basis functions for the test functions are denoted by $\left\{M_{\mathbf{u}_S}^j, M_{p_c}^j, M_{p_g}^j, M_{n_s}^j, M_\Theta^j\right\}$, with $\left\{\delta \mathbf{u}_S{}^j, \delta p^{C,j}, \delta p^{G,j}, \delta n^{S,j}, \delta \Theta^j\right\}$ representing the nodal values of the test functions [4, 73, 122].

We employ the Bubnov-Galerkin method, where the same basis functions are used for both trial and test functions, i.e., $N_{(\cdot)}^j \equiv M_{(\cdot)}^j = \phi_{(\cdot)}^j$. Moreover, the test functions $\delta(\cdot)$ naturally vanish on the homogeneous Dirichlet boundaries. It is important to note that the basis functions $\left\{\phi_{\mathbf{u}_S}^j, \phi_{p_c}^j, \phi_{p_g}^j, \phi_{n_s}^j, \phi_\Theta^j\right\}$ are position-dependent ($\mathbf{x}$), whereas the unknown nodal quantities $\left\{\mathbf{u}_S^j, p^{C,j}, p^{G,j}, n^{S,j}, \Theta^j\right\}$ are functions of time. Using the discrete trial and test functions from (5.26) and (5.27), the discretized variational problem corresponding to (5.23) can be formulated as

$$\text{Find} \quad \mathbf{u}^h \in \mathcal{S}_\mathbf{u}^h(t) \quad \text{so that} \quad \mathcal{G}_\mathbf{u}^h(\mathbf{u}^h, \delta\mathbf{u}^h) = \mathbf{0} \quad \forall \quad \delta\mathbf{u}^h \in \mathcal{T}_\mathbf{u}^h, t \in \left[t_0, T\right]. \tag{5.28}$$

For the spatial discretization of the triphasic model using the FEM, a mixed formulation is necessary to approximate all unknowns simultaneously due to the strong coupling of the governing equations. Special attention is required when selecting shape functions to ensure numerical stability, as the equations are highly coupled. To maintain stability, the shape functions must satisfy the inf-sup condition, also known as the Ladyzhenskaya-Babuška-Brezzi (LBB) condition, which ensures compatibility between approximation spaces. A common choice are Taylor-Hood elements, which use quadratic shape functions for the solid displacement $\mathbf{u}_S$. In contrast, linear shape functions are applied to the pressures p^C and p^G, solid volume fraction n^S and temperature Θ. Figure 5.1 illustrates two configurations of Taylor-Hood elements for 2D and 3D geometries. It results in a mixed finite element formulation, as recommended by Taylor and Hood [135]. This configuration satisfies the LBB condition, preventing non-physical oscillations in the solution. For further details on the mixed finite element formulation and the LBB condition, see Langtangen and Tveito [91], Brezzi and Fortin [20] and Braess [19].

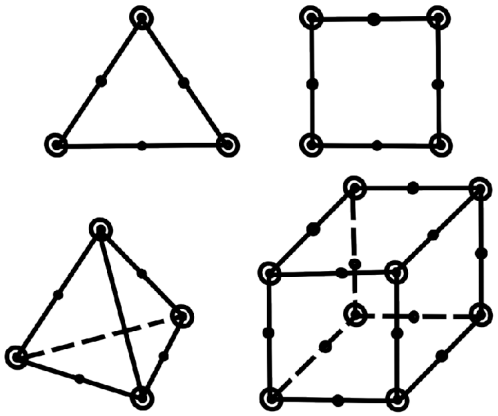

- solid displacement $\mathbf{u}_S$
- solid displacement $\mathbf{u}_S$, capillary pressure p^C, gas pressure p^G, solid volume fraction n^S and temperature Θ

Figure 5.1: Configurations of Taylor-Hood elements for 2D and 3D geometries [73].

5.1.3 Time discretization

Time-dependent variables are discretized using a finite-difference method. In this work, the implicit (backward) Euler scheme is used due to its suitability for solving differential-algebraic systems [38, 44]. After spatial discretization, the semi-discrete system is still time-dependent and requires temporal discretization. Unlike explicit methods, the implicit Euler approach allows for larger time steps and efficient handling of strongly coupled multiphysics problems. It approximates unknowns at the current time step n

$$\mathbf{u}_n'(t_n) = \frac{\Delta \mathbf{u}_n}{\Delta t_n} = \frac{\mathbf{u}_n - \mathbf{u}_{n-1}}{\Delta t_n} \quad \text{with} \quad \Delta t_n = t_n - t_{n-1}, \tag{5.29}$$

where $\mathbf{u}_n = \mathbf{u}_{n-1} + \Delta \mathbf{u}_n$ and Δt_n represents the time increment. With spatial discretization, the semi-discrete system is formulated by assembling all the degrees of freedom (nodal values) into the vector $\mathbf{u}$. The semi-discrete variation problem in (5.28) seeks a solution $\mathbf{u}^h$ in the discrete function space $\mathcal{S}_{\mathbf{u}}^h(t)$ such that the residual $\mathcal{G}_{\mathbf{u}}^h$ vanishes for all admissible test functions $\delta \mathbf{u}^h \in \mathcal{T}_{\mathbf{u}}^h$. When this weak formulation is discretized in space using finite elements and assembled over the domain, it leads to a system of differential-algebraic equations of the form $\boldsymbol{\mathcal{F}}(t, \mathbf{u}, \mathbf{u}') = \mathbf{M}\mathbf{u}' + \mathbf{K}\mathbf{u} - \mathbf{f} = \mathbf{0}$, where $\mathbf{M}$ is the generalized mass matrix, $\mathbf{K}$ the stiffness matrix and $\mathbf{f}$ the external load vector.

Furthermore, we introduce the relation in (5.29), which results in a nonlinear system of equations due to the dependence of $\mathbf{K}$ on the unknowns $\mathbf{u}$. In this formulation, the incre-

ment $\Delta\mathbf{u}_n$ appears implicitly, leading to the following nonlinear functional

$$\boldsymbol{\mathcal{F}}(t_n, \mathbf{u}_{n-1} + \Delta\mathbf{u}_n, \frac{\Delta\mathbf{u}_n}{\Delta t_n}) = \mathbf{R}_n(\Delta\mathbf{u}_n) = \mathbf{0}. \tag{5.30}$$

The nonlinear residual $\mathbf{R}_n(\Delta\mathbf{u}_n)$ at time step n is solved iteratively using the Newton-Raphson method [15]. This requires the Jacobian (or tangent) matrix, which is evaluated as

$$\mathbf{J}_n = \frac{\mathrm{d}\mathbf{R}_n}{\mathrm{d}\Delta\mathbf{u}_n} = \left.\frac{\partial\boldsymbol{\mathcal{F}}}{\partial\mathbf{u}}\right|_z + \frac{1}{\Delta t_n}\left.\frac{\partial\boldsymbol{\mathcal{F}}}{\partial\mathbf{u}'}\right|_z, \tag{5.31}$$

where $z = (t_n, \mathbf{u}_n, \mathbf{u}'_n)$ denotes the current evaluation point of the functional $\boldsymbol{\mathcal{F}}$ [73]. At each Newton iteration k, the solution increment is computed as

$$\Delta\mathbf{u}_n^{k+1} = \mathbf{u}_n^{k+1} - \mathbf{u}_n^k = -(\mathbf{J}_n^k)^{-1}\mathbf{R}_n^k, \quad \text{where} \quad \left\|\mathbf{R}_n^{k+1}\right\| < \mathrm{tol}_{\mathbf{R}} \tag{5.32}$$

The iterations proceed until the residual norm satisfies the convergence criterion. For the hydration evolution equation in (3.79) and (3.80), the material data appearing in equations are evaluated explicitly, using their values from the previous time step. This explicit treatment, which is commonly adopted in similar formulations (cf. Gawin et al. [64, 65]), simplifies the numerical implementation while maintaining sufficient accuracy for the considered application.

5.2 Parameter identification

The primary motivation of this section is to calibrate the evaporation formulation introduced in chapter 3 using the experimental data presented in chapter 4, to achieve realistic and reliable simulations of the fresh concrete's curing. Achieving such predictive capability requires that the material's physical behavior be accurately represented through constitutive equations in (5.2) to (5.6). This demands a careful identification of the model parameters $\mathbf{s}$ from experimental observations, a process referred to as the indirect problem. In contrast, the direct problem entails solving the Initial Boundary Value Problem using known parameters to compute the resulting stress, deformation, and transport fields under given boundary conditions. Ultimately, the quality of the simulation depends not only on the numerical method, but critically on the accuracy of the identified parameters and the ability of the constitutive model to capture the essential physical mechanisms involved [4].

The direct problem can be represented in an abstract form using the input quantity $\mathbf{U}$, the known material parameters $\mathbf{s}$, and the unknown output quantity $\boldsymbol{\Phi}$. It is formulated through the model function f as

$$\text{Find } \boldsymbol{\Phi}^\star \quad \text{so that} \quad f(\mathbf{s}, \mathbf{U}, \boldsymbol{\Phi}) = 0 \quad \text{for given } \{\mathbf{s}, \mathbf{U}\}, \tag{5.33}$$

where $\mathbf{\Phi}^\star$ represents the solution that satisfies the model function f in the direct problem. In parameter identification, the *indirect problem* involves finding the parameter set $\mathbf{s}^\star$ that produces a simulated material response consistent with the experimental data. This can be formulated as

$$\text{Find } \mathbf{s}^\star \quad \text{so that} \quad f(\mathbf{s}, \mathbf{U}, \mathbf{\Phi}) = 0 \quad \text{for given } \{\mathbf{U}, \mathbf{\Phi}\}. \tag{5.34}$$

In this context, the quantities $\mathbf{U}$ and $\mathbf{\Phi}$ are obtained from experimental observations. Therefore, the parameter set $\mathbf{s}^\star$ must be identified by solving an inverse problem, ensuring that the model function f is satisfied. Specifically, for the simulation example of the DVS experiment, the controlled input quantity $\mathbf{U}$ corresponds to the known mass loss of the sample.

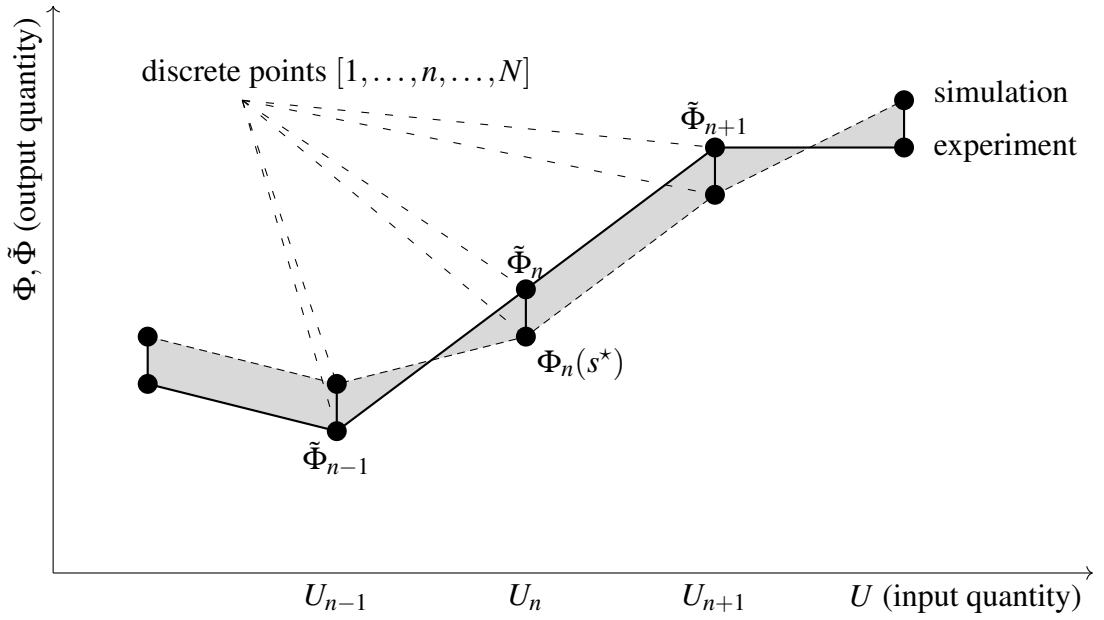

Figure 5.2: Comparison of the simulated and experimental data sets, illustrating the error $|\Phi_n - \tilde{\Phi}_n|$ between the output quantities at each discrete point n for the corresponding input quantity U_n. The shaded areas represent the discrepancy between simulation and experimental results, highlighting the variation in output across the sampled discrete points.

Complex material behavior often involves nonlinear relationships, making parameter identification challenging. In this case, the parameter set $\mathbf{s}$ is determined by minimizing the error

$$I_n = \left|\Phi_n(\mathbf{s}) - \tilde{\Phi}_n\right|, \tag{5.35}$$

at each discrete data point n out of a total of N data points, shown in the Figure 5.2. The aim of this work is to calibrate the evaporation process in fresh concrete, as modeled in

chapter 3, using experimental data presented in chapter 4. To accurately reproduce the evaporation behavior observed in fresh concrete, the material parameters governing the mass exchange process, shown in Figure 3.2 to Figure 3.5, must be identified. These parameters, while central to the formulation, cannot be measured directly and are therefore determined indirectly through calibration. As a result, their identification is framed as an indirect problem and addressed through nonlinear optimization techniques. Starting from an initial guess $\mathbf{s}^0$, the parameter vector $\mathbf{s}$ is iteratively updated to minimize the discrepancy between simulation results and experimental observations, ultimately converging to an optimal set $\mathbf{s}^\star$. Here, $\Phi_n(\mathbf{s})$ denotes the simulated response at the n-th data point, and $\tilde{\Phi}_n$ is the corresponding value measured in the DVS experiment. The objective is to minimize the error across all data points, thereby ensuring the best possible agreement between the model and the observed evaporation behavior. To ensure a valid and consistent comparison, the same input conditions U_n are applied in both the simulation and experiment. In addition, for time-dependent problems such as this, the temporal evolution must be treated consistently in both datasets. This approach ensures that the identified parameters $\mathbf{s}^\star$ reliably characterize the material behavior within the framework of the governing model function f. Finally, the efficiency and robustness of the optimization process strongly depend on the choice of initial values $\mathbf{s}_0$. Providing well-informed initial guesses can substantially enhance convergence speed and stability. Nonetheless, the method remains applicable even when only rough or uninformed initial estimates are available.

The Least-Squares Method is employed to minimize the objective function f, which quantifies the total simulation error based on deviations between simulated and experimentally observed material behavior. The experimental data are considered the reference for the true material response. A multi-criterion objective function is used to capture this deviation

$$f(\mathbf{s}) = \frac{1}{2} \sum_{k=1}^{K} \sum_{n=1}^{N_k} w^k I_n^2 \rightarrow \min, \tag{5.36}$$

where each term I_n represents the pointwise error between simulation and experiment and w^k is a weighting factor specific to each experimental data set k. The factor w^k is defined as the inverse of the maximum reference value $\left|\Phi_0^k\right|$ in the data set, divided by the number of data points N_k

$$w^k = \frac{1}{\left|\Phi_0^k\right| N_k}. \tag{5.37}$$

This normalization guarantees consistent error scaling across various experiments, enabling each data set to contribute proportionally to the overall optimization. It is important to note that the parameter identification is formulated as a constrained optimization problem, minimizing $f(\mathbf{s})$ subject to the equality constraints $h_j(\mathbf{s}) = 0$ for $j = 1, \ldots, N_{eq}$, where these constraints ensure agreement between the model predictions and our experimental results.

6 MODELLING OF FRESH CONCRETE

The primary innovation of the proposed model for fresh concrete lies in the explicit inclusion of the evaporation rate term, a crucial factor affecting concrete's long-term durability and structural performance. By incorporating this term, the model aims to enhance the understanding of evaporation kinetics, thereby improving the accuracy of moisture transport predictions. To achieve a comprehensive analysis of moisture dynamics, the study is structured into three interconnected stages. Initially, an experimental investigation was conducted to calibrate the evaporation rate term utilizing Dynamic Vapor Sorption (DVS) technology. DVS allows accurate measurements of moisture interactions under precisely controlled environmental conditions, thereby providing robust experimental data for calibrating the model. Subsequently, the theoretical accuracy of the model was validated by benchmarking its predictions against the established findings by Gawin et al. [64]. This validation links empirical results to a strong theoretical foundation, thus ensuring that the developed model adheres to fundamental physical principles that govern moisture transport within cementitious materials.

In contrast to prior models, the present study introduces a mass balance equation for the solid phase, enabling a physically grounded investigation of the commonly assumed linear relationship between porosity and the degree of hydration. This assumption, made explicitly by Gawin et al. [64] and implicitly through the use of the Powers model in the work of Sciumè et al. [130], is critically assessed in our framework by directly modeling the evolution of solid phase. The validity of this linear porosity–hydration relationship is examined for two different concrete types under distinct environmental conditions, providing new insight into its applicability during early-age hydration and material evolution. The model further refines Pichler's micromechanical approach [111] within a multiscale strength prediction framework for early-age concrete by integrating it with Powers' hydration model [115]. A significant advancement of this study is the explicit incorporation of strength evolution as a function of the hydration degree, which varies spatially throughout the domain. By directly linking strength development to the progressing hydration state, the model provides a more accurate and physically consistent representation of material behavior. To validate the implementation, numerical simulations based on Pichler's methodology are performed and, subsequently, compared with experimental data from a benchmark study [85], ensuring the robustness and applicability of the proposed framework.

All three numerical studies simulate the early stages of concrete curing, covering a period of two to three days depending on the specific example. During this time, the evaporation process evolves dynamically before approaching a stabilized, quasi-stationary state. In all three cases, an adaptive time-stepping scheme was employed to accurately capture the transient behavior, with time step lengths ranging from 1 s to 180 s, depending on the progress

of hydration. At $t = 0$, both hydration and evaporation processes initiate within the porous material, leading to mass exchange among the solid, liquid, and gaseous phases.

6.1 Experimental validation of the evaporation process

The objective of this section is to calibrate the evaporation formulation introduced in section 3.5 using experimental data obtained through the Dynamic Vapor Sorption method, described in detail in chapter 4. This validation ensures that the model accurately reflects the evaporation in fresh concrete under controlled environmental conditions. The experimental data obtained from the DVS experiment is used in calibrating the mass exchange equation (3.79). To systematically investigate the evaporation behavior in fresh concrete,

Property	**Cement**	**Water**	**Normsand**
Standard	CEM I, EN 197-1	-	DIN EN 196-1
Main Composition	95% Portland clinker	H_2O	Pure quartz sand
Mass [g]	302	120 (added) + 11.22 (adsorbed)	748

Table 6.1: Concrete properties and mix composition characteristics.

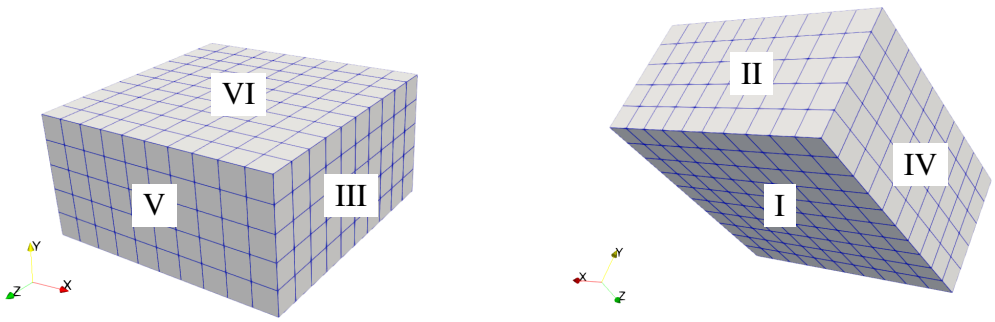

Figure 6.1: Three-dimensional geometry and mesh representation of the DVS sample with numbered surfaces.

DVS experiments were performed on eight small rectangular samples, see chapter 4. The material properties of these samples are outlined in Table 6.1. To ensure consistency, all specimens were prepared under controlled conditions and placed within the DVS chamber as shown in chapter 4, where their mass changes were continuously monitored over

time. Figure 6.1 provides a three-dimensional representation of the sample geometry and its corresponding computational mesh. In this visualization, the surfaces of the sample are distinctly numbered from I to VI, facilitating a clear identification of boundary conditions and aiding in the interpretation of materials behavior.

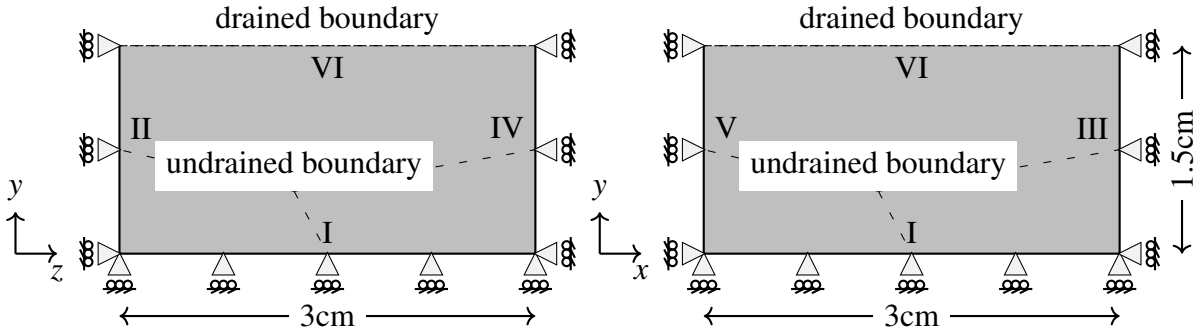

a) y-z plane cross-section. b) x-y plane cross-section.

Figure 6.2: Cross-sections of the DVS sample geometry in the y-z and x-y planes.

To provide a detailed understanding of the experimental geometry and boundary conditions, Figures in 6.2 present cross-sectional views of the sample geometry of Figure 6.1. Figure 6.2.b shows a cross-section of the sample in the x-y plane, illustrating its horizontal dimensions and the applied boundary conditions along the vertical edges. Figure 6.2.a complements this by showing the y-z plane, giving a view of the sample's vertical structure and how it interacts with its surroundings in depth. Together, these schematic views help to visualize the experimental setup and clearly define how the boundaries of the sample are treated. The specific boundary conditions used in the simulation are summarized in Table 6.2.

In the computational domain, the top surface (labeled VI) is designated as a drained boundary, allowing exchange, whereas all remaining surfaces are treated as undrained boundaries, restricting any flux. To ensure mechanical stability, the bottom edge is constrained in the y-direction, while the side edges are constrained in the x- and z-direction, preventing displacements in these respective directions. The chamber environment is maintained at a constant temperature of 293 K, relative humidity Φ of 0.94, and atmospheric pressure $p^G = p^{\text{atm}}$ of 101.325 kPa. To reflect the controlled conditions of the closed chamber described in the preceding experimental section, boundary conditions are applied in the numerical model accordingly.

Importantly, because of the relationship between capillary pressure and relative humidity, as given by Equation (3.69), the applied boundary condition along edge VI in Figure 6.2, where the relative humidity is fixed at 0.94, corresponds to a capillary pressure of 8.352 MPa. This ensures that the simulation accurately reflects the moisture conditions

Side	Boundary conditions	Unit
I	$u_y = 0$	m
	$\tilde{w}_{LS} = 0$	$kg/(m^2 s)$
	$\tilde{w}_{GS} = 0$	$kg/(m^2 s)$
	$\tilde{q}^{\Theta} = 0$	W/ms
II, IV	$u_z = 0$	m
	$\tilde{w}_{LS} = 0$	$kg/(m^2 s)$
	$\tilde{w}_{GS} = 0$	$kg/(m^2 s)$
	$\tilde{q}^{\Theta} = 0$	W/m^2
III, V	$u_x = 0$	m
	$\tilde{w}_{LS} = 0$	$kg/(m^2 s)$
	$\tilde{w}_{GS} = 0$	$kg/(m^2 s)$
	$\tilde{q}^{\Theta} = 0$	W/m^2
VI	$p^C = 8.352 \times 10^6$	Pa
	$p^G = 1.0132 \times 10^3$	Pa
	$\Theta = 293.15$	K

Table 6.2: Used boundary conditions for the cube geometry.

imposed during the experiment. For the numerical simulation, the material properties are adopted from literature sources [31, 64] and are detailed in Table A.1 in the Appendix.

To ensure an optimal balance between computational efficiency and accuracy, a mesh sensitivity study was conducted for this simulation before the inclusion of the evaporation process. Three different mesh resolutions were evaluated: a coarse mesh with 100 elements, a moderate-resolution mesh with 500 elements, and a fine mesh with 1152 elements. Figure 6.3 illustrates the cube geometry of the sample, displaying all three mesh sizes alongside the temperature distribution at $t = 1\,\mathrm{d}$.

	Absolute Error [-]	Relative Error [%]	Simulation Time Relative to Reference [%]
100-element mesh	0.0596	0.00064331%	8.397%
500-element mesh	0.0361	0.00038943%	38.855%

Table 6.3: Comparison of temperature evolution errors and simulation times for coarser meshes relative to the 1152-element reference model.

In this study, the 1152-element mesh simulation serves as the reference. Absolute errors are computed as the L_2 norm of the difference between the test and reference temperature profiles, while relative errors are obtained by normalizing this value against the L_2 norm of the reference and expressing it as a percentage. Although the differences are minimal, the

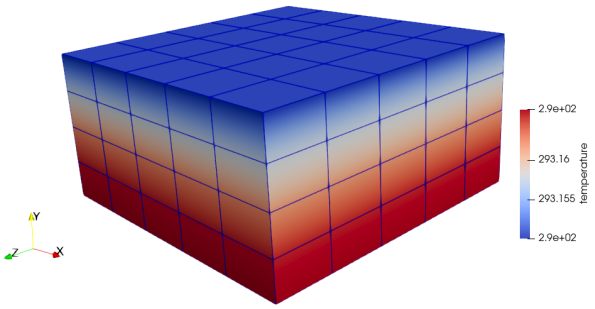

a) Mesh with 100 elements.

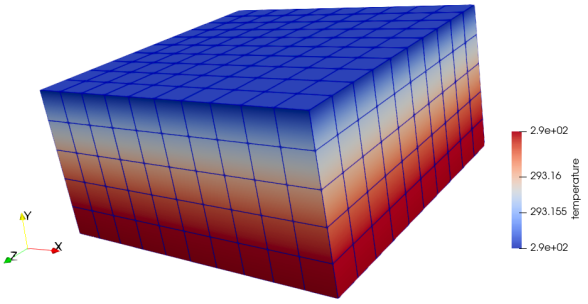

b) Mesh with 500 elements.

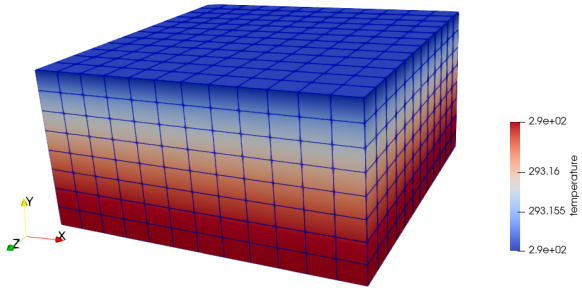

c) Mesh with 1152 elements.

Figure 6.3: Spatial temperature distribution at $t = 1\,\mathrm{d}$ for different mesh sizes under prescribed boundary conditions (Table 6.2).

500-element mesh shows slightly lower absolute (0.0361 vs. 0.0596) and relative errors (0.00038943% vs. 0.00064331%) than the 100-element mesh, see Table 6.3. Addition-

ally, the table includes a comparison of the simulation durations relative to the reference 1152-element mesh. The 100-element mesh requires only about 8.4% of the computation time of the reference, while the 500-element mesh takes approximately 38.86%. Considering the marginal gain in accuracy alongside the substantial reduction in computational cost, the 500-element mesh is chosen as the optimal compromise for all subsequent simulations. To further assess the impact of model complexity, an additional numerical study was conducted using the 500-element mesh. We compared a simplified formulation, accounting only for energy balance, hydration evolution and mass balance of the solid phase (treated as a two-phase system), with the full model that includes all governing equations. The full formulation required over 2500% more computational time than the simplified one, clearly illustrating the substantial cost associated with fully coupled thermo-hygro-chemo-mechanical modeling. It is also important to note that, unlike in previously mentioned high-temperature scenarios, where convergence issues tend to arise due to the strong nonlinear coupling between saturation and capillary pressure, no such difficulties were encountered in the present case. For detailed discussions and numerical strategies addressing these convergence problems, the reader is referred to the works of Dal Pont and Ehrlacher [29], Pohl et al. [113].

Symbol	Values	Unit
$\mathcal{C}$	0.3	$\mathrm{mg/sm^3}$
β_1	1.0	s/mm
β_2	1.05	-
β_3	125.0	-
β_4	0.3	-

Table 6.4: Calibrated material parameters for equations (3.82) and (3.83).

Furthermore, the parameters $\mathcal{C}$ and β_i, required in equations (3.82) and (3.83), have been now calibrated based on experimental data. The calibration process involves computing the mean value of the measured mass change across the eight sample boxes and comparing it with the numerical simulation results. It is important to note that the parameter set presented in Table 6.4 is not unique, multiple parameter combinations can satisfy the imposed constraints within the set error tolerance. However, the values reported in the table represent one physically meaningful and numerically robust solution, which was selected and used for the subsequent simulations presented in this work. After obtaining the calibrated set of parameters, a sensitivity analysis was performed to assess how variations in each individual parameter influence the evaporation rate model's accuracy. The results, summarized in Table 6.5, demonstrate the impact of these parameter changes on the model's performance. The parameter values tested were chosen arbitrarily to explore the model's response and should be interpreted with caution. The reference simulations use the calibrated parameters listed in Table 6.4. The parameter $\mathcal{C}$ serves as a global scaling factor that linearly controls the overall magnitude of the evaporated mass per volume and time.

Symbol	Value	L_2 Norm [kg/(m^{3}s)]	Relative L_2 Norm [%]
$\mathcal{C}$	0.03	5.396e-03	90.0
$\mathcal{C}$	0.15	3.002e-03	50.1
$\mathcal{C}$	0.6	6.036e-03	100.7
$\mathcal{C}$	1.5	2.441e-02	407.2
β_1	0.1	4.107e-06	0.1
β_1	0.5	2.282e-06	0.1
β_1	2.0	4.564e-06	0.1
β_1	5.0	1.825e-05	0.3
β_2	0.1	3.681e-03	61.4
β_2	0.5	2.541e-03	42.4
β_2	2.0	9.592e-03	160.0
β_2	5.0	3.743e-01	6244.9
β_3	12.5	5.918e-03	98.7
β_3	62.5	1.649e-03	27.5
β_3	250	3.536e-03	59.0
β_3	600	6.622e-02	1104.8
β_4	0.03	4.705e-03	78.5
β_4	0.15	3.458e-03	57.7
β_4	0.6	—	did not converge
β_4	1.5	—	did not converge

Table 6.5: L_2 norm and relative L_2 norm of simulated evaporation rates compared to the reference solution.

Changes in $\mathcal{C}$ proportionally increase or decrease the evaporation rate, as reflected by the corresponding L_2 values. The parameter β_1 models the coupling to the moisture gradient and exhibits exponential sensitivity, meaning higher values significantly amplify the evaporation response to saturation gradients, with only minor L_2 fluctuations indicating robustness. Parameter β_2 introduces an offset in the hydration-dependent term, causing modest shifts in the hydration baseline and resulting in moderate variations in L_2. Meanwhile, β_3 controls the steepness and nonlinearity of the hydration response, showing high sensitivity by localizing evaporation around the reference hydration. This is evident from larger L_2 changes at extreme values. Lastly, β_4 defines the reference hydration level, acting as the symmetry center of the hydration effect. Its variation moderately shifts the evaporation response peak, with values outside the typical range causing convergence issues. These observations highlight the varying degrees of influence each parameter exerts on the performance of the model.

As hydration progresses, the reaction between water and cement increases the solid volume fraction while reducing the availability of free water. Figure 6.4 illustrates this gradual

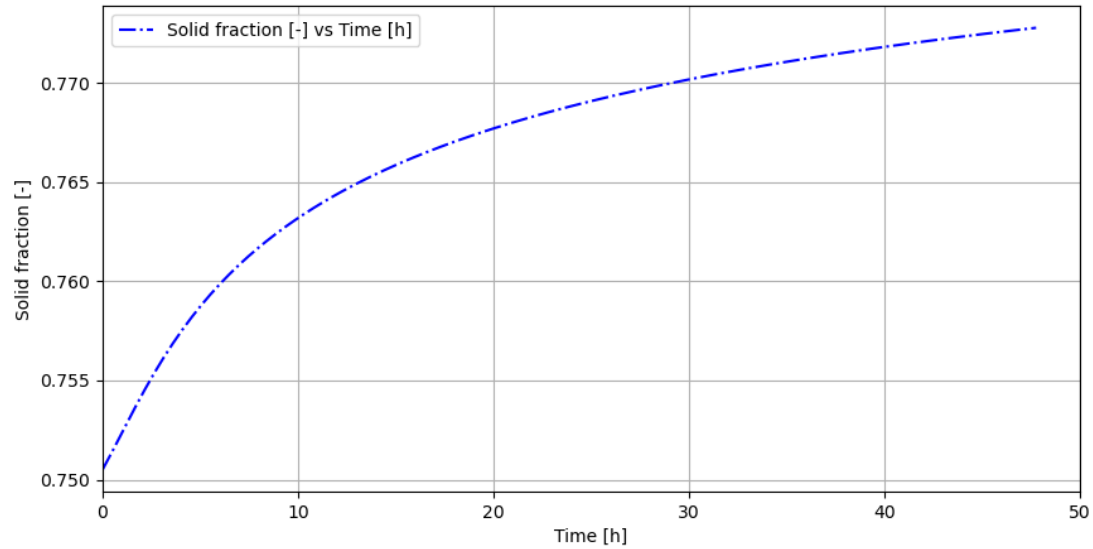

Figure 6.4: Mean solid volume fraction evolution during the first 2 days of concrete's hardening.

solidification by depicting the mean value of the solid fraction over time. This numerical

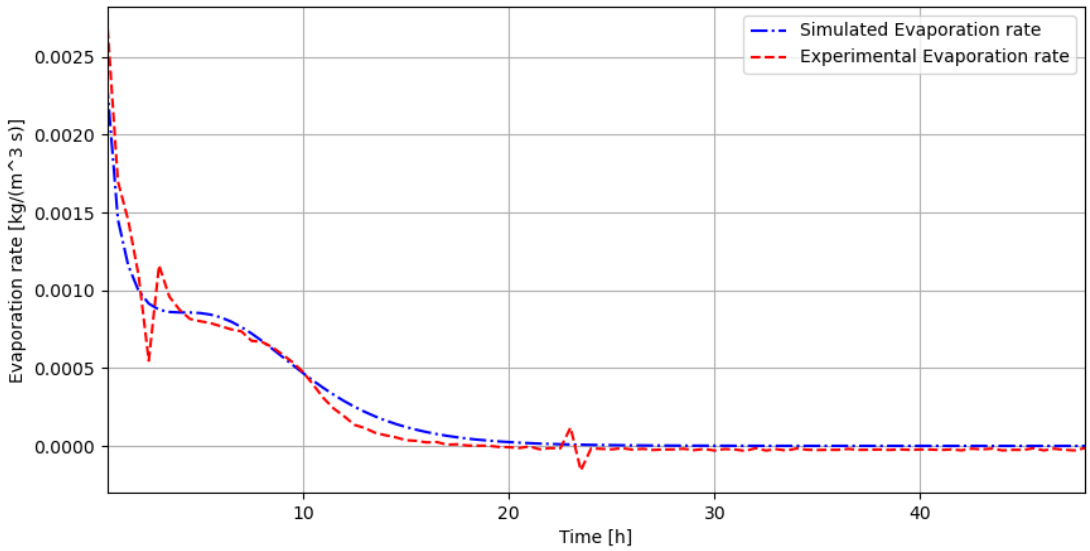

Figure 6.5: Comparison of numerical and experimental evaporation rate $\hat{\rho}^G$ [kg/m^{3}s] for the proposed model.

study examines the evaporation process, where liquid water transitions into dry air and escapes through the top boundary. The evaporation rate, defined by Equation (3.81), is influenced by calibration parameters $\mathcal{C}$ and β_i, with their calibrated values provided in Table 6.4. Figure 6.5 presents a comparison between experimental measurements and numerical simulations of evaporation rates. Initially, evaporation is high due to strong interactions between the solid and liquid phases, which accelerate hydration. As hydration advances, the reaction rate decreases, leading to a gradual reduction in evaporation within the material.

In Figure 6.5, the red line represents the experimental data. The oscillations observed in the curve are attributed to the sensitivity of the mass measurement, which is particularly noticeable during the initial phase of concrete hardening, especially around the three-hour mark. These fluctuations are a result of the high precision required for detecting small mass changes at early hydration stages. Conversely, the blue line in Figure 6.5 illustrates the mean value of numerical results obtained from the proposed computational model. This simulation incorporates key factors influencing the evaporation process, such as the hydration degree and the seepage velocity of the liquid phase. The comparison between the experimental and numerical curves demonstrates excellent agreement, confirming the success of the calibration. The model, using the calibrated parameters listed in Table 6.4, accurately captures the evaporation behavior during the early-age hardening of concrete.

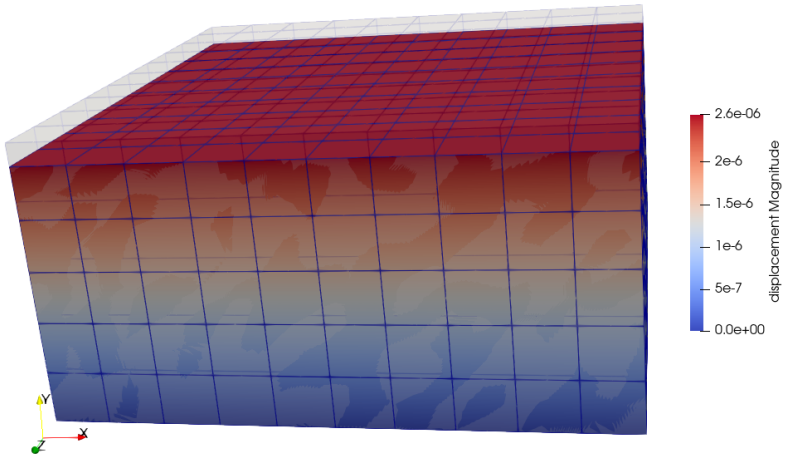

Figure 6.6: Displacement field of the 3D cube after 24 hours of concrete maturation, showing deformed (colored) versus undeformed (grey) mesh with exaggerated displacement magnitudes.

Following the successful calibration of the evaporation rate in the material model, the displacement field is evaluated on the original 3D cube geometry. Figure 6.6 illustrates the full cube, where the grey region represents the undeformed mesh, while the colored region shows the deformed configuration after 24 hours of concrete maturation. The 24-hour time

point was selected arbitrarily and the displacement magnitudes have been intentionally exaggerated to improve visual interpretation. Figure 6.7 provides a representative view of the

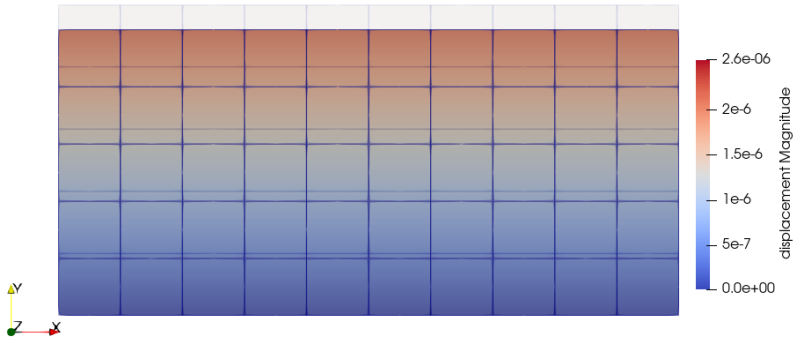

Figure 6.7: Displacement field on central x–y plane after 24 hours maturation, showing deformed (color) and undeformed (grey) mesh.

solid displacement field in the central x–y plane of the cube. This plane was chosen such that the y–z projection is geometrically equivalent, owing to the cubic shape of the specimen and the application of symmetric boundary conditions on all sides. The visualization corresponds to the state after 24 hours of concrete maturation and captures the early-age deformation behavior, showing both the magnitude and direction of the displacement vectors within this mid-plane.

6.2 Numerical validation

The preceding study focused on calibrating the evaporation process in concrete using dynamic vapor sorption experiments. Building on this foundation, we now validate the proposed model against Gawin's framework to assess its predictive capabilities. Gawin's model assumes a linear relationship between porosity and hydration degree, an empirical assumption derived from experimental observations and incorporated as a fixed relation. In contrast, our approach introduces evolution equations for hydration, providing a more flexible representation that is not limited to a predefined linear dependency. This extension allows for a broader exploration of hydration-porosity interactions beyond Gawin's fixed formulation. Furthermore, the proposed model incorporates a geometrically and materially non-linear formulation, enabling a more comprehensive representation of the evolving concrete structure. This non-linearity is particularly significant for accurately capturing behavior during early-age hydration.

This section examines two distinct cases under different environmental conditions, both from the benchmark model Gawin et al. [64]. The first scenario involves ordinary concrete specimens subjected to an adiabatic test, focusing on the material's thermal response in

an isolated environment. The second scenario investigates the influence of varying wall thicknesses, specifically analyzing the effect of convective heat transfer between two opposing surfaces of a wall. This comparative approach provides insights into both intrinsic thermal properties and the role of boundary interactions in heat dissipation. By comparing our results with Gawin's model, we examine the validity of his assumptions and identify potential improvements in predictive modeling.

6.2.1 Case 1: Adiabatic conditions

In the first scenario, a cylindrical specimen with a length of 60 cm and a diameter of 4 cm is considered, as shown in Figure 6.8. To reduce computational cost without compromising accuracy, the model takes advantage of axial and rotational symmetry. This allows the 3D problem to be simplified to a 2D representation in polar coordinates. As a result, only a cross-sectional slice, 30 cm in length and 2 cm in height, representing half the specimen, is modeled. The midline of the cylinder corresponds to the lower boundary in Figure 6.8. By applying this simplification, the computational model efficiently captures the essential mechanical response of the specimen while significantly reducing numerical complexity.

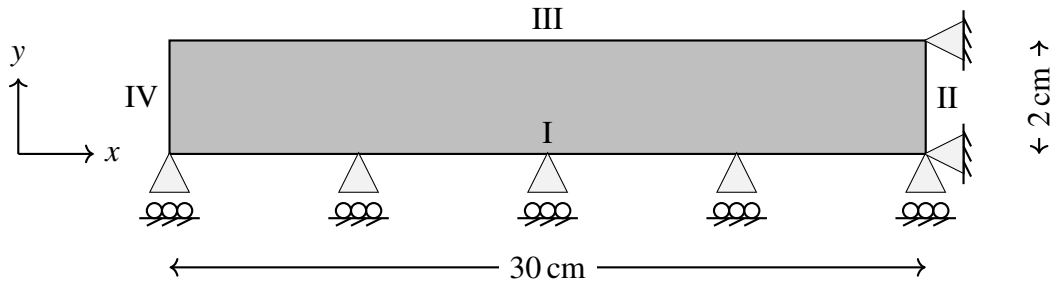

Figure 6.8: Geometry and boundary conditions of the cylindrical specimen based on Gawin et al. [64].

The boundary conditions for this setup adhere to an adiabatic formulation, consistent with the approach employed by Gawin et al. [64, 65], ensuring alignment with the reference model for direct comparison. As detailed in Table 6.6, all boundaries are treated as undrained surfaces, imposing a no-flux condition to replicate adiabatic behavior. Furthermore, zero normal solid displacement is enforced along the right and bottom edges, while traction-free conditions are applied in the tangential directions. This configuration ensures that the model accurately reflects the thermomechanical constraints necessary for evaluating the material response under adiabatic conditions during the initial three-day curing period. The simulation is conducted on ordinary concrete (OC), a material previously examined by Bentz et al. [13] and later utilized by Cervera et al. [22, 23] to

Side	Boundary conditions	Unit
I	$u_y = 0$	m
	$\tilde{w}_{LS} = 0$	$kg/(m^2s)$
	$\tilde{w}_{GS} = 0$	$kg/(m^2s)$
	$\tilde{q}^{\Theta} = 0$	W/ms
II	$u_x = 0$	m
	$u_y = 0$	m
	$\tilde{w}_{LS} = 0$	$kg/(m^2s)$
	$\tilde{w}_{GS} = 0$	$kg/(m^2s)$
	$\tilde{q}^{\Theta} = 0$	W/ms
III	$\tilde{w}_{LS} = 0$	$kg/(m^2s)$
	$\tilde{w}_{GS} = 0$	$kg/(m^2s)$
	$\tilde{q}^{\Theta} = 0$	W/m^2
IV	$\tilde{w}_{LS} = 0$	$kg/(m^2s)$
	$p^G = 101325$	Pa
	$\tilde{q}^{\Theta} = 0$	W/m^2

Table 6.6: Used boundary conditions for the cylindrical specimen in Figure 6.8.

validate their early-stage thermo-chemo-mechanical concrete model. The composition of OC closely resembles that studied by Baroghel-Bouny et al. [5] in their investigations of hygral properties. The basic material properties used in the simulations are taken from the literature and are summarized in Table A.1 in the appendix. In contrast, the material parameters calibrated through the experimental procedure presented in the previous section, shown in Table 6.4, represent the key contribution of this work. These calibrated values are incorporated into the validation case to ensure an accurate representation of the evaporation behavior. At the start of the simulation, the material is initialized with a temperature of $\Theta_0 = 293.15\,\mathrm{K}$, a relative humidity of $\Phi_0 = 0.999$ and an initial hydration degree of $\Gamma_0 = 0.1$.

Figure 6.9 presents the mean temperature evolution over a 72-hour period for the proposed model, highlighting the thermal development during the early hardening phase of fresh concrete. A comparative assessment against the results of Gawin et al. [64] reveals a strong correlation, validating the accuracy of the numerical model. In Figure 6.9, the blue line represents the mean temperature evolution predicted by the proposed extended model, while the dotted green line corresponds to the numerical results of Gawin et al. [64]. Additionally, the red crosses denote the experimental temperature data utilized in the benchmark study. The strong agreement among these three datasets confirms the accuracy and reliability of the proposed model. Further validation is provided in Figure 6.10, which depicts the evolution of the hydration degree over time, comparing the predictions of the proposed extended model with those of Gawin's benchmark model. The close agreement between the datasets confirms the model's accuracy in capturing early hydration of concrete. As pre-

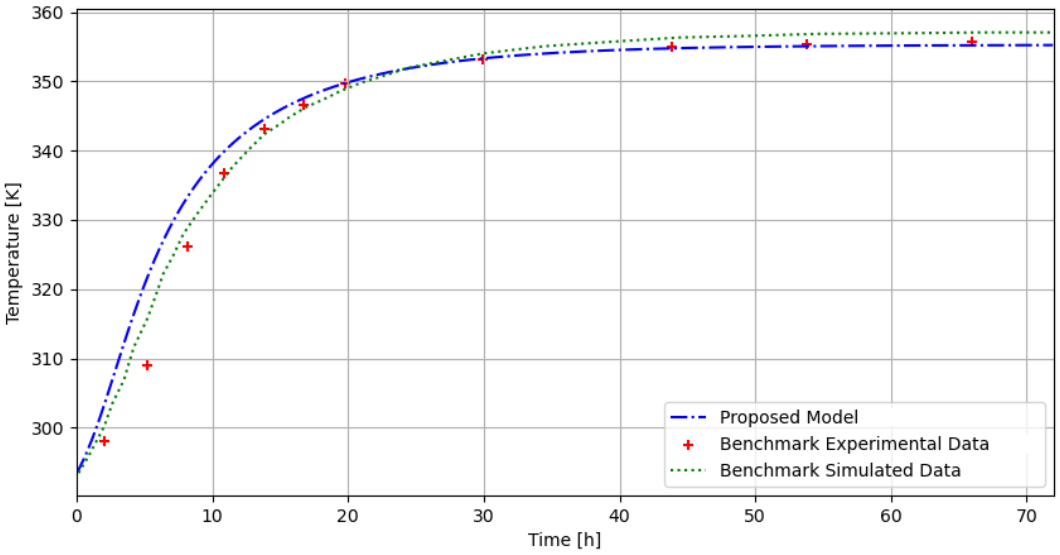

Figure 6.9: Comparison of temperature evolution during the first 72 hours of hydration: Proposed model vs. Gawin et al. [64] and experimental data used for validation.

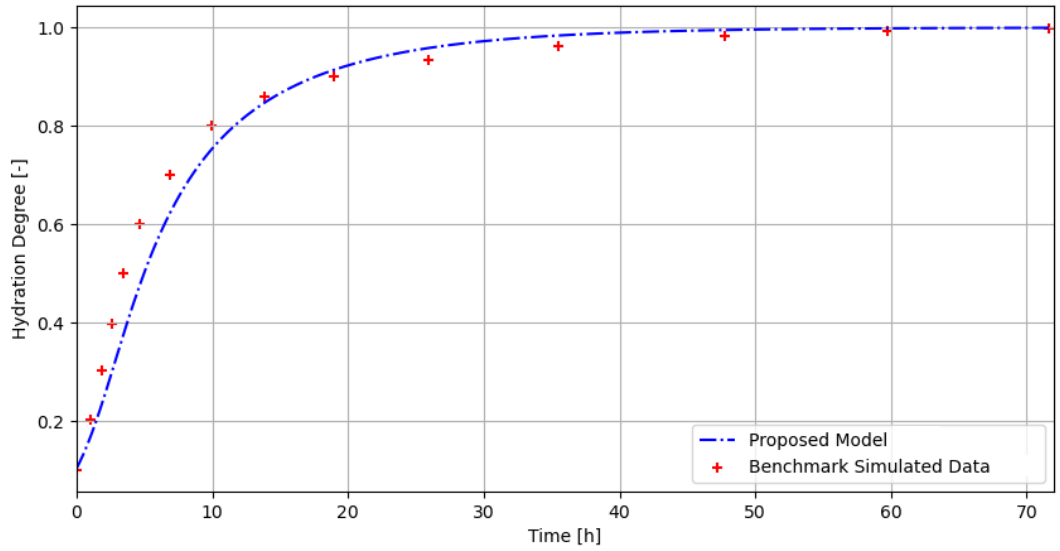

Figure 6.10: Comparison of hydration degree evolution during the first 72 hours: Proposed model vs. Gawin et al. [64].

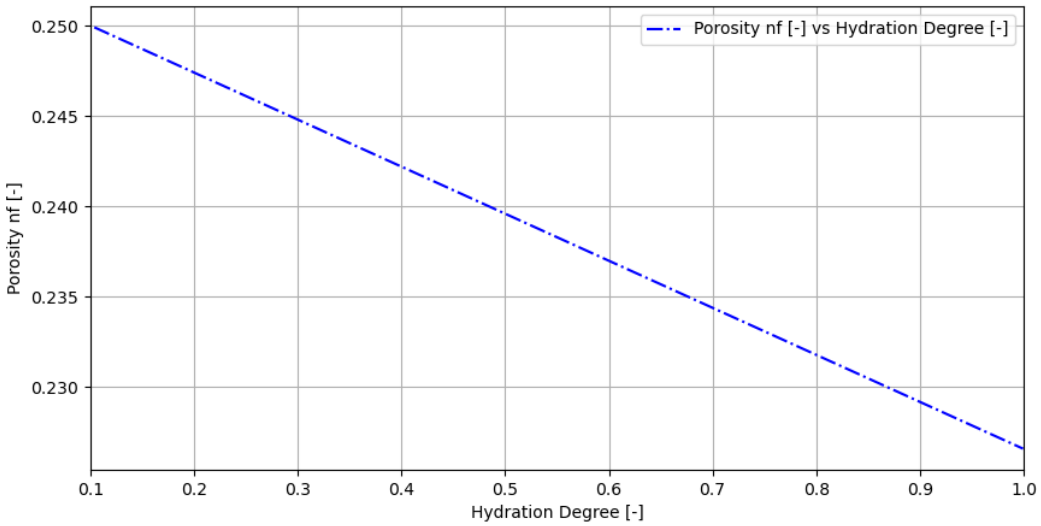

Figure 6.11: Mean value relation between porosity and hydration degree in fresh concrete.

viously discussed, Gawin's model assumes a linear relationship between porosity n^F and the hydration degree Γ_{hydr}, derived from experimental observations. The results from the proposed evolution equation accurately reproduce the observed linear relationship between porosity n^F and hydration degree Γ_{hydr}, highlighting the model's capability to capture this key behavior in early-age concrete, as illustrated in Figure 6.11. The values shown are averaged over the entire domain, demonstrating the model's ability to reflect the expected trend under the specified conditions. However, it is important to recognize that this linear correlation may not hold universally across all concrete mixtures or boundary conditions, as it depends on material composition and environmental factors. This relationship will be further examined in the next section under convective conditions for a different concrete mix.

6.2.2 Case 2: Convective conditions

Building on the previous case study, the second analysis examines the hygro-thermo-chemical behavior of a different concrete mix, C-30, within a 2D model, representing a wall section viewed from above as shown in Figure 6.12. The model includes convective heat exchange with a constant ambient environment to simulate realistic boundary interactions. Two thicknesses are considered, $d = 40\,\text{cm}$ and $d = 80\,\text{cm}$, corresponding to the label d in Figure 6.12. To validate the present model, the benchmark setup by Gawin was closely followed. Specifically, the geometry maintains the same thickness-to-height ratio ($d : h = 1 : 15$) as in Gawin's initial example.

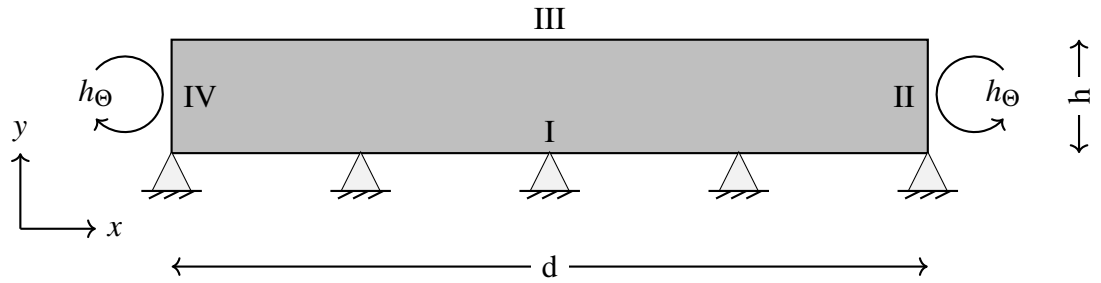

Figure 6.12: Geometric configuration of the wall model based on Gawin et al. [64] with varying thicknesses.

The hydration kinetics described by equations (3.79) and (3.80) are simulated using key material parameters specific to C-30 concrete. These parameters are listed in Table 6.7. Initially, the wall is assigned a temperature of $\Theta_0 = 293.15\,\mathrm{K}$, a relative humidity of $\Phi_0 = 0.999$ and an initial hydration degree of $\Gamma_{\mathrm{hydr},0} = 0.1$, reflecting that the material has already developed some structural rigidity.

Parameter	**Symbol**	**C-30**	**Unit**
Water/cement ratio	w/c	0.35	-
Heat of hydration	$Q_{\mathrm{hydr},\infty}$	102	$\mathrm{MJ/m^3}$
Activation Energy in Eq (3.79)	E_a/R	5000.0	K
Parameter in Eq (3.80)	A_1	0.95×10^4	$1/\mathrm{s}$
Parameter in Eq (3.80)	A_2	0.5×10^{-5}	-
Parameter in Eq (3.80)	κ_∞	0.66	-
Parameter in Eq (3.80)	$\bar{\eta}$	5.3	-

Table 6.7: Characteristics of C-30 concrete using data from the benchmark model Gawin et al. [64].

From this point onward, the external surfaces of the wall (sides II and IV, as specified in Table 6.8) are subjected to convective boundary conditions for heat exchange. This represents the scenario in which the wall has been demolded, except for cases where it remains sealed. The calibrated evaporation mass production (3.81) is incorporated into the main model. The convective heat transfer coefficient is set to $h_\Theta = 8.3\,\mathrm{W\,m^{-2}\,K^{-1}}$, while boundary conditions for normal displacements are consistent with those used in the first example (refer to Table 6.8). To validate the model, boundary and initial conditions are adopted from the benchmark model by Gawin et al. [64], ensuring a direct comparison with established numerical results.

Side	Boundary conditions	Unit
I	$u_x = 0$	m
	$u_y = 0$	m
	$\tilde{w}_{LS} = 0$	$kg/(m^2s)$
	$\tilde{w}_{GS} = 0$	$kg/(m^2s)$
	$\tilde{q}^{\Theta} = 0$	W/ms
II, IV	$\tilde{w}_{LS} = 0$	$kg/(m^2s)$
	$\tilde{w}_{GS} = 0$	$kg/(m^2s)$
	$\tilde{q}^{\Theta} = h_{\Theta}(\Theta - \Theta_{\infty})$,	W/ms
III	$\tilde{w}_{LS} = 0$	$kg/(m^2s)$
	$\tilde{w}_{GS} = 0$	$kg/(m^2s)$
	$\tilde{q}^{\Theta} = 0$	W/ms

Table 6.8: Used boundary conditions for the wall example.

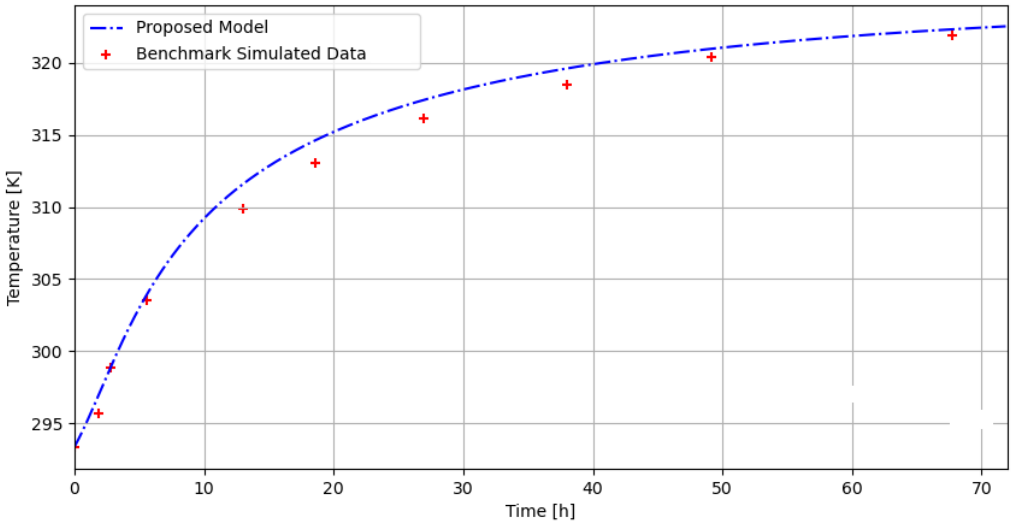

Figure 6.13: Comparison of temperature evolution in two models over the first 72 hours of concrete hydration under the adiabatic conditions.

The evolution of temperature and hydration degree over the first three days of concrete curing will be presented since early-age hydration plays a crucial role in defining the mechanical properties of fresh concrete. Special attention is given to this initial phase, where the most significant changes occur. As a crucial first step in validating the proposed model for the C-30 concrete mix, a preliminary simulation is performed under adiabatic conditions. This pretest focuses on the temperature evolution during hydration and serves to verify that the model accurately reproduces the benchmark results reported by Gawin. Once this val-

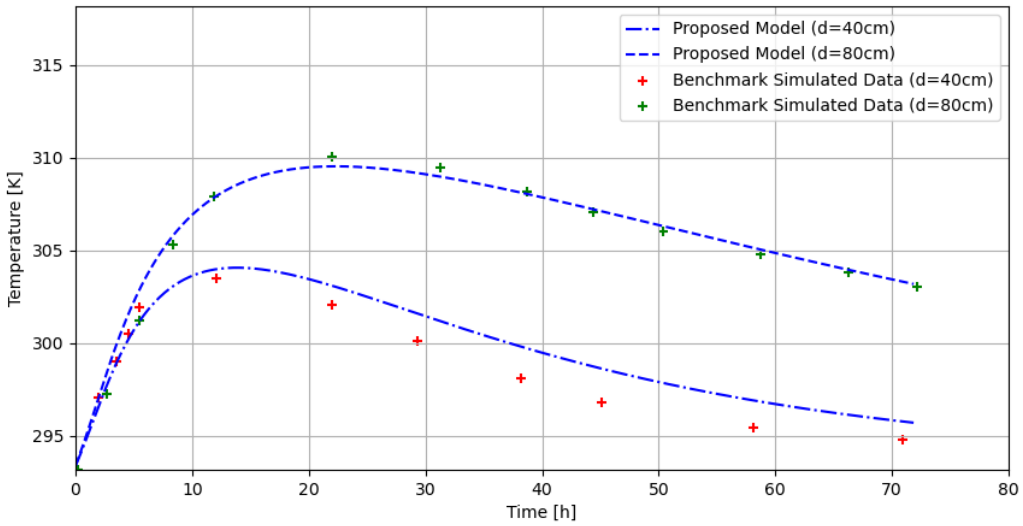

Figure 6.14: Temperature evolution during the first 72 hours of concrete hydration in the 2D wall configuration: Comparison between the proposed model and Gawin's benchmark data.

idation is achieved as shown in the Figure 6.13, the convection case is applied, where the external environment is maintained at a constant temperature of $\Theta = 293.15\,\mathrm{K}$, a relative humidity of $\Phi = 0.75$ and a gas pressure equal to atmospheric pressure $p^G = p^{\mathrm{atm}}$.

Figure 6.14 illustrates the temperature evolution over a 72-hour period, capturing the behavior of C-30 concrete in the wall configuration. A comparison with Gawin's results [64] demonstrates a strong correlation between the two models. In the figure, the blue lines represents the predicted temperature evolution from the proposed extended model for the both wall thicknesses $d = 40\,\mathrm{cm}$ and $d = 80\,\mathrm{cm}$, while the red and green markers correspond to Gawin's numerical results from [64]. The strong agreement between the two datasets confirms the validity of the extended model in accurately capturing the thermal behavior of early-age concrete for both wall thicknesses. Minor deviations between the proposed model and Gawin's benchmark data are observed, which can be attributed to differences in modeling approaches and potential variations in material parameters.

To further evaluate the proposed model, Figure 6.15 presents the evolution of the hydration degree over time for the two different wall thicknesses, 40 cm and 80 cm. The presented results depict the mean hydration degree computed across the entire domain under the influence of external environmental conditions. The spatial distribution of the hydration degree is a key factor in determining the material's mechanical properties, as it directly affects strength development and long-term durability. To further examine the role of convective heat and mass exchange between the surrounding environment and the concrete,

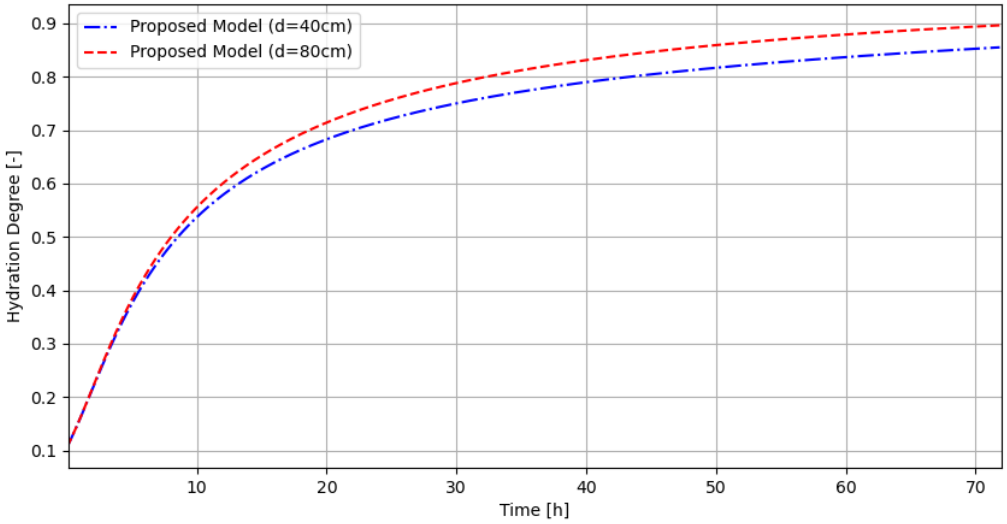

Figure 6.15: Evolution of the mean hydration degree over time for different wall thicknesses ($d = 40\,\text{cm}$ and $d = 80\,\text{cm}$).

Figure 6.16 illustrates the hydration degree distribution across the entire domain at $t = 3\,\text{d}$ for a wall thickness of $d = 40\,\text{cm}$.

Figure 6.16: Spatial evolution of the hydration degree across the domain for a wall thickness of 40 cm at $t = 3\,\text{d}$.

In this case, under convection conditions, we once again investigate the validity of this assumed linear correlation between porosity n^F and the hydration degree Γ_{hydr}. Figure 6.17 presents the computed relationship between porosity and hydration degree, plotted as the mean value across the entire domain for the case with an 80 cm wall thickness. The results confirm that the assumed linear correlation remains valid in this scenario, as well as for the 40 cm wall thickness. While a linear relationship is observed in this case, this does not imply it holds for all boundary conditions or concrete mixes.

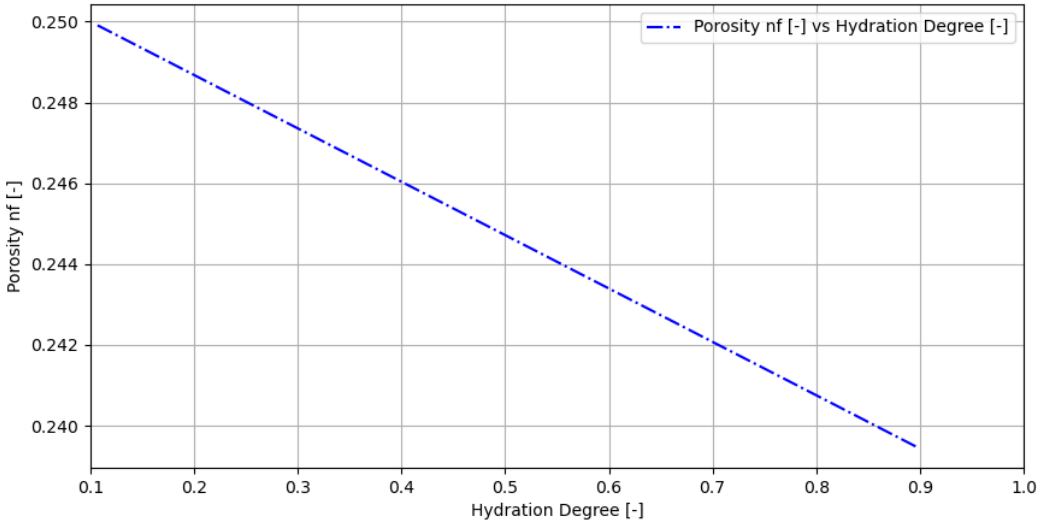

Figure 6.17: Relationship between porosity and hydration degree for fresh concrete with wall thickness $d = 80\,\text{cm}$.

6.3 Numerical validation of multiscale strength prediction for early-age concrete

To extend the analysis, we incorporate Pichler's multiscale model for compressive strength, which links macroscopic behavior to microstructural mechanisms by downscaling stress through the interfacial transition zone (ITZ) to the C-S-H phase. Failure is governed by a Drucker-Prager criterion calibrated with nanoindentation data [88, 111], while hydration progression is captured using Powers' model [115]. This framework allows for a nonlinear prediction of strength evolution under varying conditions. To validate the model's accuracy, numerical results are compared with experimental data from the benchmark study [85], focusing on the development of compressive strength and Young's modulus, the latter being derived via the standardized ACI formulation.

Calibrating the evolution of the hydration degree is essential to align the numerical model with the temperature development recorded in the benchmark experiments. The geometric configuration used for this comparison is shown in Figure 6.18. In the subsequent Figure 6.19, the hydration evolution equation is calibrated using the initial conditions specified in the benchmark study, which assumes an initial temperature of $\Theta_0 = 20\,^\circ\text{C}$ and adiabatic conditions, meaning all boundaries are sealed and no fluxes occur.

To further validate the model's predictive capability, the same setup was tested with a different initial temperature of $\Theta_0 = 10\,^\circ\text{C}$, allowing for an assessment of temperature evolu-

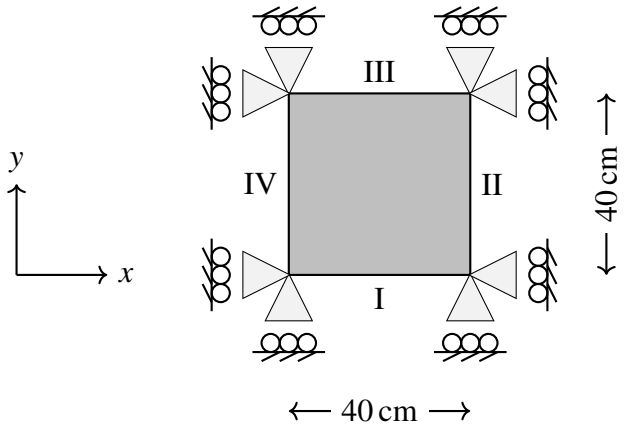

Figure 6.18: Description of the geometry setup (40×40 cm^2) from the benchmark [85]

tion under varying conditions. As shown in Figure 6.19, the blue dashed line represents the calibrated hydration evolution equation aligned with the benchmark data (green crosses) for the case with an initial temperature of 20 °C. The blue dash-dotted line corresponds to the case with an initial temperature of 10 °C and demonstrates the model's ability to accurately predict hydration kinetics and temperature development under varying thermal conditions, as validated against the benchmark data (red crosses). This process is formu-

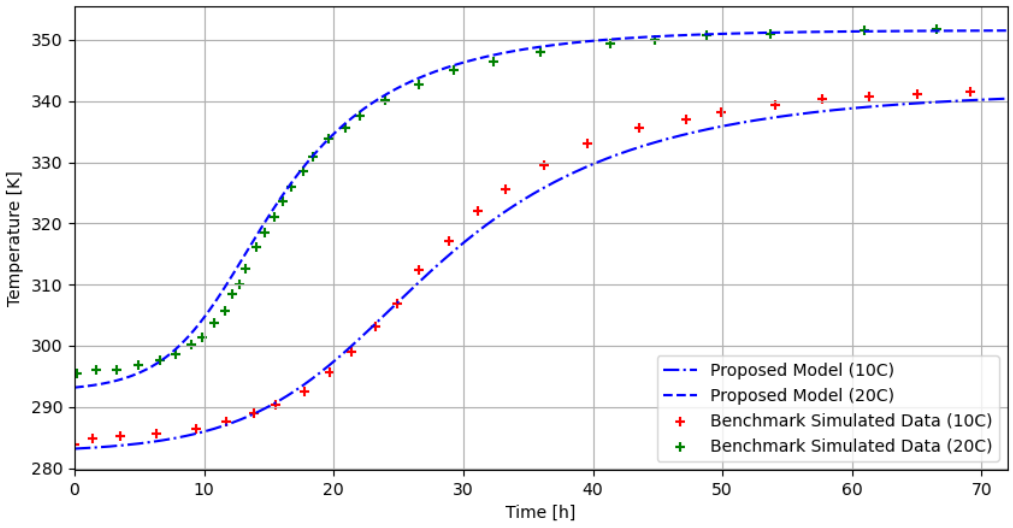

Figure 6.19: Calibration and validation of mean temperature evolution under sealed conditions against benchmark data [85] for initial temperatures $\Theta_0 = 10\,°C$ and $\Theta_0 = 20\,°C$.

lated based on the concrete mix composition (Table 6.9), along with the geometry problem

setup shown in Figure 6.18, initial conditions, and boundary conditions. The boundary conditions are established following the benchmark study [85], where thermal exchange with the surroundings is governed by convection and radiation, uniformly applied across all surfaces. The heat transfer mechanism is modeled using a Robin boundary condition (5.11), incorporating a thermal exchange coefficient h_Θ, which quantifies the interaction with external environment. The initial conditions are defined to represent the freshly mixed

Name	Value	Unit
Initial temperature Θ_0	293.15	K
Ambient temperature Θ_∞	293.15	K
Initial Hydration degree $\Gamma_{\text{hydr},0}$	0	–
Coefficient of thermal exchange	10	W/(m^2·K)
Convective Robin b.c.	$h_\Theta(\Theta - \Theta_\infty)$	W/(ms)

Table 6.9: Initial and boundary conditions for the given problem setup.

state of the concrete, with an initial temperature of $\Theta_0 = 293.15\,\text{K}$ and an initial hydration degree of $\Gamma_{\text{hydr},0} = 0$, ensuring alignment with the experimental setup, summarized in Table 6.9. The most significant thermal variations occur within the first 36 hours, driven primarily by heat generation from the hydration process. The temperature distribution across the domain is illustrated at six representative time points ($t = 0, 11, 15, 18, 25, 36\,\text{h}$) in Figure 6.20, highlighting the gradual development of thermal gradients, peaking in the center and diminishing toward the edges due to convective heat loss. This temperature pattern results from the interplay between internal heat release and external environmental influences, as governed by the imposed boundary conditions. A comparable spatial pattern, peaking at the center and decreasing toward the edges, is evident in the hydration degree distribution, highlighting the strong interdependence between thermal evolution and hydration processes during the early stages of concrete hardening.

In this study, Young's modulus is derived from the evolving compressive strength. As illustrated in Figure 6.21, the compressive strength increases very slowly during the first 12 hours, after which the material begins to transition into a more rigid concrete state. Beyond this point, the strength increases more steadily, eventually reaching approximately 43 MPa after a 3-day period.

Furthermore, the mean Young's modulus over the entire domain is compared to experimental data from [85], demonstrating strong agreement, particularly during the early-age phase, as shown in Figure 6.22. This validation confirms the model's ability to capture the mechanical response of the material and its evolution over time.

The evolution of Young's modulus across the domain is directly influenced by the spatial temperature distribution, rather than remaining constant. As illustrated in Figure 6.20, the

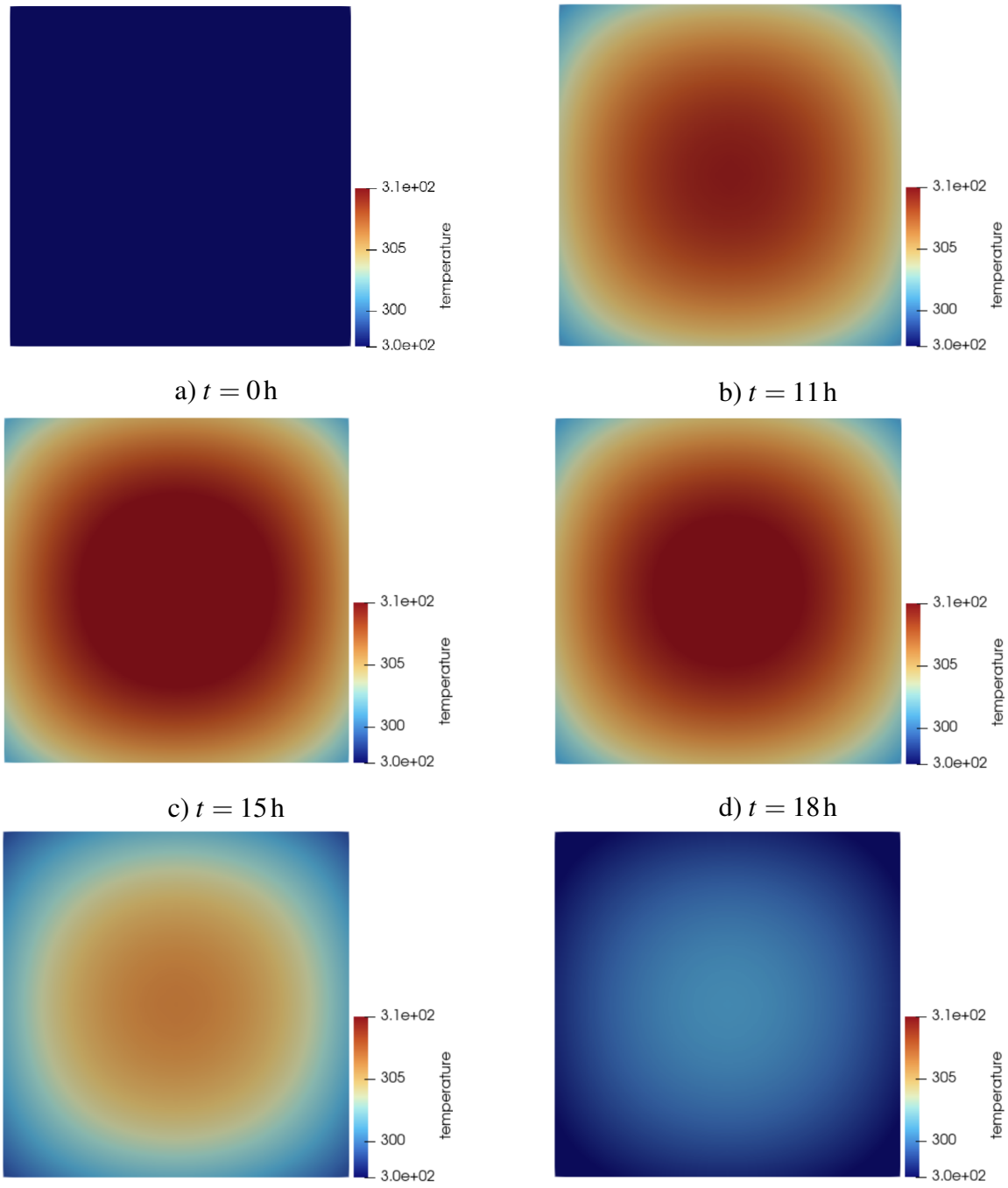

a) $t = 0\,\mathrm{h}$ b) $t = 11\,\mathrm{h}$

c) $t = 15\,\mathrm{h}$ d) $t = 18\,\mathrm{h}$

e) $t = 25\,\mathrm{h}$ f) $t = 36\,\mathrm{h}$

Figure 6.20: Temperature distribution and heat accumulation over time.

highest temperatures develop at the center of the domain due to heat accumulation, which accelerates hydration and leads to increased stiffness in this region. As a result, Young's

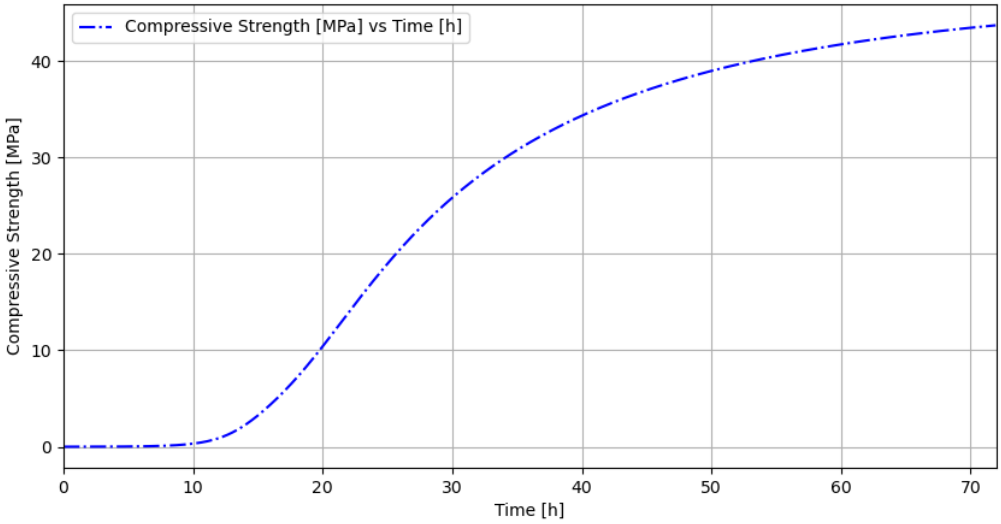

Figure 6.21: Mean compressive strength development over time.

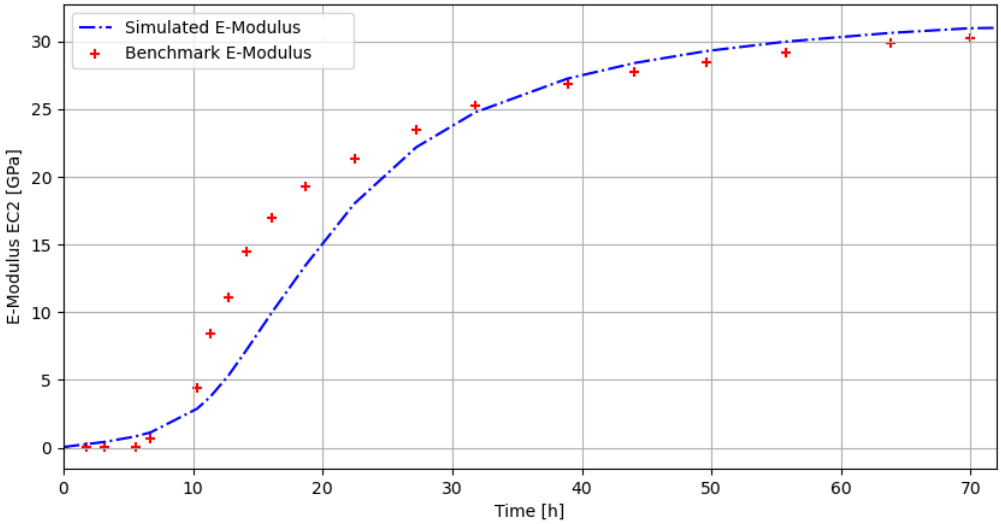

Figure 6.22: Mean Young's modulus development over time: Comparison with benchmark experiment [85].

modulus exhibits a characteristic circular distribution, with peak values concentrated at the core, while lower values appear near the boundaries, where cooling effects, primarily driven by lateral convection, slow hydration and reduce stiffness.

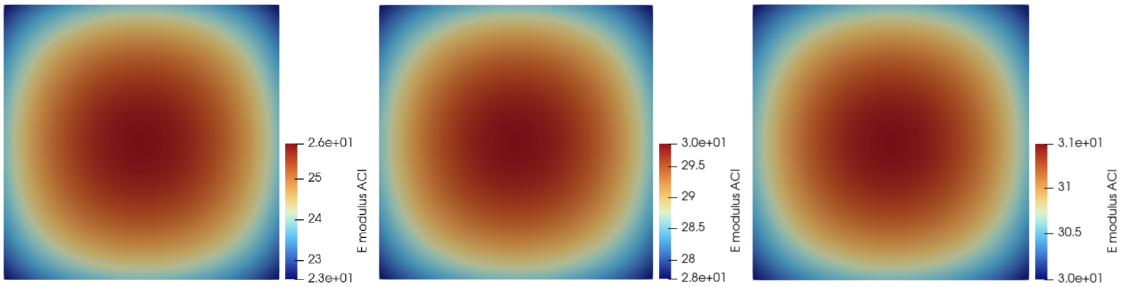

a) $t = 1\,\mathrm{d}$ b) $t = 2\,\mathrm{d}$ c) $t = 3\,\mathrm{d}$

Figure 6.23: Spatial variation of Young's modulus: Increased stiffness in the core driven by hydration at 1 d, 2 d and 3 d.

It is important to note that Figures 6.23 illustrate the Young's modulus distribution at $t = 1, 2, 3\,\mathrm{d}$, capturing its temporal evolution. While the overall spatial distribution pattern remains consistent, the scale of values differs significantly across the three snapshots, reflecting the progressive increase in stiffness as hydration advances and the material continues to harden.

7 CONCLUSION

7.1 Summary

In this work, we presented a numerical model to simulate the early-age behavior of concrete, building upon the established triphasic Theory of Porous Media framework originally proposed by Gawin. Concrete is modeled as a porous material comprising incompressible solid and liquid phases and a compressible gas phase, with hydration and evaporation serving as the key interaction mechanisms. The model focuses on the initial stages of concrete maturation, where moisture transport and phase interactions critically influence mechanical evolution.

A core innovation of this study is the introduction of a physically motivated and experimentally calibrated evaporation formulation. Using data obtained from Dynamic Vapor Sorption (DVS) experiments, we accurately captured the influence of moisture loss on hydration kinetics, an aspect frequently simplified in traditional approaches. This evaporation function was integrated into the numerical solver and validated against benchmark simulations, confirming its accuracy in predicting early-age concrete behavior. While a linear correlation between porosity and hydration degree is observed for the studied concrete mixes, it may not hold universally across all concrete types or boundary conditions. Crucially, the proposed model is not limited to linear behavior, it is capable of capturing more complex, nonlinear interactions shaped by varying material compositions and environmental influences. To assess the model under varied conditions, the validation uses a different concrete mix and modified boundary conditions, providing a broader evaluation of its robustness and general applicability.

Another significant advancement lies in the integration of a multiscale approach for predicting the development of mechanical properties. The evolution of Young's modulus was linked directly to hydration-driven strength gain using a thermodynamically consistent formulation. Simulation results showed good agreement with experimental data, both in terms of average mechanical response and local spatial variability. Notably, the model captured stiffness gradients arising from hydration and temperature variations, with peak stiffness occurring near the core due to thermal accumulation.

Overall, the developed model demonstrates strong predictive capabilities for simulating early-age concrete behavior. It provides a reliable framework for capturing both moisture transport and mechanical development under varying curing conditions, paving the way for future extensions involving different concrete mixes, environmental scenarios and enhanced microstructural resolution.

7.2 Outlook

The present work has laid a foundation for modeling the hygro-thermo-chemical behavior of fresh concrete, but several promising avenues remain for future exploration and development.

One key direction involves the optimization of the free energy function governing the solid phase of concrete. This advancement would enable the material to be described initially as a viscoelastic medium and, with the inclusion of porosity, extended to a porous viscoelastic formulation. To support this theoretical development, new experimental investigations will be essential. These should include normal force loading tests, relaxation experiments and cyclic loading protocols to capture the stress response of fresh concrete in a controlled manner. The main challenges are not only numerical but primarily experimental, specifically, in ensuring reliable specimen-device interaction. Achieving an ideal surface-to-surface contact between the concrete sample and loading apparatus is critical for extracting meaningful, reproducible results. This would also require precise alignment and surface preparation of the specimens.

Another promising research direction involves expanding the current modeling framework to simulate reinforced concrete structures. This would bring the model closer to practical civil engineering applications. The key challenge lies in accurately capturing the interaction between concrete and reinforcing steel, particularly the mechanical bond and its evolution over time. Simplified contact models must strike a balance between computational efficiency and physical realism, especially under conditions where the viscous behavior of concrete becomes significant at later hydration stages.

In addition, the observed linear relationship between porosity and hydration degree, as confirmed in this work, prompts further investigation. While the linearity holds under specific conditions, it is unlikely to be universal. Identifying scenarios where this relationship breaks down, such as under alternative boundary conditions or with different mix designs, could provide deeper insight into the limits of the current model and help to generalize its applicability.

A particularly promising extension of this research is the incorporation of ultrasonic wave propagation experiments as a non-destructive method to investigate the evolving properties of fresh concrete. In this context, concrete would again be treated as a multiphase material, enabling a more realistic representation of the interactions between solid, liquid and gaseous phases during early hydration. Ultrasonic waves propagating through the material can provide valuable insights into its internal structure, with measurable quantities such as wave velocity and attenuation being closely linked to key properties like porosity, stiffness and hydration state. Capturing this dynamic response requires an extension of the current modeling framework to include inertial (acceleration) terms and to account for wave reflection, transmission and dispersion phenomena within the heterogeneous medium. Such

a development could bridge the gap between experimental observations and numerical simulations, offering a powerful, real-time tool for characterizing fresh concrete during its early transformation into a load-bearing material.

A APPENDIX

A.1 Important relations

A.1.1 Reformulation of energy balance using stress power

The energy balance equation for a multiphase material can be simplified by expressing the internal stress power in terms of effective and pore pressures. The total mechanical power input by stresses across all constituents α is given by

$$\begin{aligned}\sum_{\alpha} \mathbf{T}^{\alpha} : \mathbf{L}_{\alpha} &= (\mathbf{T}_E^S - p^S \mathbf{I}) : \mathbf{L}_S + (-p^L \mathbf{I}) : \mathbf{L}_L + (-p^G \mathbf{I}) : \mathbf{L}_G \\ &= \mathbf{T}_E^S : \mathbf{L}_S - \sum_{\alpha} p^{\alpha} \operatorname{div} \mathbf{x}_{\alpha}^{'},\end{aligned} \tag{A.1}$$

where $\mathbf{T}_E^S$ denotes the effective stress tensor in the solid skeleton, and $\operatorname{div} \mathbf{x}_{\alpha}^{'}$ represents the velocity divergence of constituent α, noting that $\mathbf{I} : \mathbf{L}_{\alpha} = \operatorname{div} \mathbf{x}_{\alpha}^{'}$ due to the trace operation. By substituting equation (A.1) into the general energy balance equation (3.16), we arrive at the following compact form of the enthalpy balance

$$\sum_{\alpha} \left(\rho^{\alpha} (h^{\alpha})^{'} - (p^{\alpha})^{'} \right) = \mathbf{T}_E^S : \mathbf{L}_S - \sum_{\alpha} \operatorname{div} \mathbf{q}^{\alpha} - \sum_{\alpha} \hat{\rho}^{\alpha} h^{\alpha}. \tag{A.2}$$

A.1.2 Constitutive relation for specific heat capacity

To evaluate the rate of change of enthalpy with temperature, we introduce the specific heat capacity at constant pressure, denoted by C_p^{α}. It is defined as

$$C_p^{\alpha} = \frac{\partial h^{\alpha}}{\partial \Theta^{\alpha}}, \quad \text{such that} \quad (h^{\alpha})^{'} = C_p^{\alpha} \, (\Theta^{\alpha})^{'}. \tag{A.3}$$

This relation allows the temperature evolution to be linked directly to enthalpy variations under isobaric conditions. For a comprehensive thermodynamic background, the reader is referred to [117, 142].

A.2 Summary of all material parameters

The following Table A.1 displays all the material parameters used for this triphasic material model of ordinary fresh concrete (OC) and coefficients of the state equation for water.

Parameter	Symbol	Value	Unit
Lame constant	λ^S	1.1×10^{10}	$\mathrm{N/m^2}$
Lame constant	μ^S	1.65×10^{10}	$\mathrm{N/m^2}$
Hydration degree at $t = 0$	Γ_0	0.1	-
Temperature at $t = 0$	Θ_0	293	K
Gas pressure at $t = 0$	p_0^G	101325	Pa
Solid volume fraction at $t = 0$	n_0^S	0.75	-
Relative humidity at $t = 0$	Φ_0	0.999	-
Water apparent density at $t = 0$	ρ_0^{LR}	1.0×10^3	$\mathrm{kg/m^3}$
Solid apparent density at $t = 0$	ρ_0^{SR}	2.65×10^3	$\mathrm{kg/m^3}$
Molar mass of water	M_W	18.015×10^{-3}	kg/mol
Molar mass of air	M_G	28.964×10^{-3}	kg/mol
Universal gas constant	R	8.3144	J/(kg mol)
Parameter in Eq (3.70)	a	18.6237	MPa
Parameter in Eq (3.70)	b	2.2748	-
Intrinsic permeability	k_0	1×10^{-18}	$\mathrm{m^2}$
Parameter in Eq (3.65)	A_T	0.05	-
Parameter in Eq (3.65)	A_p	0.368	-
Parameter in Eq (3.66)	m	0.51	-
Parameter in Eq (3.86)	A_λ	0.0005	1/K
Therm. effective conductivity of dry material	λ_{d0}	1.67	W/(mK)
Specific heat of solid at $t = 0$	C_{P0}^S	800	J/(kgK)
Specific heat of water at $t = 0$	C_{P0}^L	4186.0	J/(kgK)
Specific heat of air at $t = 0$	C_{P0}^G	1006.0	J/(kgK)
Parameter in Eq (3.56)	A_s	0.000195	$\mathrm{kg/(m^3K)}$
Parameter in Eq (3.71)	p_{w1}	1.0×10^7	Pa
Parameter in Eq (3.71)	$p_{\mathrm{w,ref}}$	2.0×10^7	Pa
Heat of hydration process	Δh_{hydr}	2.5×10^6	J/kg
Parameter in Eq (3.79)	β_Φ	1.0	-
Activation Energy in Eq (3.79)	E_a/R	5000.0	K
Parameter in Eq (3.80)	A_1	0.95×10^4	1/s
Parameter in Eq (3.80)	A_2	0.5×10^{-5}	-
Parameter in Eq (3.80)	κ_∞	0.72	-
Parameter in Eq (3.80)	$\bar{\eta}$	5.3	-
Critical temperature in Eq (3.84)	Θ_{cr}	647.3	K

Table A.1: Material parameters for fresh concrete.

a_0	a_1	a_2	a_3	a_4	a_5
4.89×10^{7}	-1.65×10^{-9}	1.86×10^{-12}	2.43×10^{-13}	-1.60×10^{-15}	3.37×10^{-18}
b_0	b_1	b_2	b_3	b_4	b_5
1.02×10^{-3}	-7.74×10^{-1}	8.77×10^{-3}	-9.21×10^{-5}	3.35×10^{-7}	-4.40×10^{-10}

Table A.2: Coefficients of the state equation for water [57].

REFERENCES

[1] M. Addassi and B. Johannesson. Reactive mass transport in concrete including for gaseous constituents using a two-phase moisture transport approach. *Construction and Building Materials*, 232:117148, 2020.

[2] P. Adler. *Porous Media: Geometry and Transports*. Elsevier, Amsterdam, 2013. ISBN 9781483219189. doi: 10.1016/C2010-0-67073-4.

[3] M. G. Alexander and S. Mindess. *Aggregates in Concrete*. CRC Press, Boca Raton, FL, 2005. doi: 10.1201/9781482264647.

[4] O. Avci. Coupled deformation and flow processes of partially saturated soil: Experiments, model validation and numerical investigations. Bericht Nr. II-26, Universität Stuttgart, Institut für Mechanik, Lehrstuhl II, 2013.

[5] V. Baroghel-Bouny, M. Mainguy, T. Lassabatère, and O. Coussy. Characterization and identification of equilibrium and transfer moisture properties for ordinary and high-performance cementitious materials. *Cement and Concrete Research*, 29(8): 1225–1238, 1999. doi: 10.1016/S0008-8846(99)00102-7.

[6] K. J. Bathe. *Finite Element Procedures*. Klaus-Jürgen Bathe, Boston, MA, 2006. ISBN 978-0979004902.

[7] Z. Bazant and B. H. Oh. Crack band theory for fracture of concrete. *Materials and Structures*, 16:155–177, 1983. doi: 10.1007/bf02486267.

[8] Z. P. Bazant. Prediction of concrete creep and shrinkage: Past, present and future. *Nuclear Engineering and Design*, 203:27–38, 2001. doi: 10.1016/s0029-5493(00)00299-5.

[9] Z. P. Bazant and L. Najjar. Nonlinear water diffusion in nonsaturated concrete. *Materials and Structures*, 5:3–20, 1972. doi: 10.1007/bf02479073.

[10] Z. P. Bazant and J. Planàs. *Fracture and Size Effect in Concrete and Other Quasibrittle Materials*. CRC Press, Boca Raton, FL, 2019. doi: 10.1201/9780203756799.

[11] Z. P. Bazant and P. C. Prat. Microplane model for brittle-plastic material: I. Theory. *Journal of Engineering Mechanics*, 114:1672–1688, 1988. doi: 10.1061/(asce)0733-9399(1988)114:10(1672).

[12] R. Belarbi, N. Issaadi, A. Nouviaire, and A. Aït-Mokhtar. Moisture characterization of cementitious material properties: Assessment of water vapor sorption isotherm and permeability variation with ages. *Construction and Building Materials*, 83: 237–247, 2015. doi: 10.1016/j.conbuildmat.2015.03.081.

[13] D. P. Bentz, V. Waller, and F. de Larrard. *Prediction of Adiabatic Temperature Rise in Conventional and High-Performance Concretes Using a 3-D Microstructural Model*. U.S. Dept. of Commerce, NIST, 1998. doi: 10.1016/S0008-8846(97)00264-0.

[14] M. A. Biot. General theory of three-dimensional consolidation. *Journal of Applied Physics*, 12(2):155–164, 1941. doi: 10.1063/1.1712886.

[15] J. Bonet and R. D. Wood. *Nonlinear Continuum Mechanics for Finite Element Analysis*. Cambridge University Press, Cambridge, UK, 1997. ISBN 0-521-57272-X. doi: 10.1017/CBO9780511755446.

[16] R. M. Bowen. Theory of mixtures. In A. C. Eringen, editor, *Continuum Physics*, volume 3, pages 1–127. Academic Press, New York, 1976. doi: 10.1016/B978-0-12-240803-8.50017-7.

[17] R. M. Bowen. Incompressible porous media models by use of the theory of mixtures. *International Journal of Engineering Science*, 18:1129–1148, 1 1980. ISSN 0020-7225. doi: 10.1016/0020-7225(80)90114-7.

[18] R. M. Bowen. Compressible porous media models by use of the theory of mixtures. *International Journal of Engineering Science*, 20(6):697–735, 1982. doi: 10.1016/0020-7225(82)90079-7.

[19] D. Braess. *Finite Elements: Theory, Fast Solvers, and Applications in Solid Mechanics*. Cambridge University Press, Cambridge, UK, 2001. ISBN 978-0521011952.

[20] F. Brezzi and M. Fortin. *Mixed and Hybrid Finite Element Methods*, volume 15. Springer Science & Business Media, Berlin, Heidelberg, 2012. ISBN 978-0387983379.

[21] R. H. Brooks and A. T. Corey. Properties of porous media affecting fluid flow. *Journal of the Irrigation and Drainage Division, ASCE*, 92(2):61–88, 1966. doi: 10.1061/JRCEA4.0000425.

[22] M. Cervera, J. Oliver, and T. Prato. Thermo-chemo-mechanical model for concrete. I: Hydration and aging. *Journal of Engineering Mechanics*, 125(9):1018–1027, 1999. doi: 10.1061/(ASCE)0733-9399(1999)125:9(1018).

[23] M. Cervera, R. Faria, J. Oliver, and T. Prato. Numerical modelling of concrete curing, regarding hydration and temperature phenomena. *Computers & Structures*, 80:1511–1521, 2002. doi: 10.1016/S0045-7949(02)00104-9.

[24] Z. Chen, H. Steeb, and S. Diebels. A EVI-space-time galerkin method for dynamics at finite deformation in porous media. *Computational Mechanics*, 43(5):585–601, 2008. doi: 10.1007/s00466-008-0332-9.

[25] B. D. Coleman and W. Noll. The thermodynamics of elastic materials with heat conduction and viscosity. In W. Noll, editor, *The Foundations of Mechanics and Thermodynamics: Selected Papers*, pages 145–156. Springer, Berlin, Heidelberg, 1974. doi: 10.1007/978-3-642-65817-4_9.

[26] O. Coussy. *Poromechanics*. John Wiley & Sons, Chichester, UK, 2004. doi: 10.1002/0470092718.

[27] J. J. Cross. Mixtures of fluids and isotropic solids. *Archives of Mechanics*, 25(6): 1025–1039, 1973.

[28] B. Dacorogna. *Direct Methods in the Calculus of Variations*, volume II. Springer, New York, 2007. doi: 10.1007/978-0-387-55249-1.

[29] S. Dal Pont and A. Ehrlacher. Numerical and experimental analysis of chemical dehydration, heat and mass transfers in a concrete hollow cylinder submitted to high temperatures. *International Journal of Heat and Mass Transfer*, 47:135–147, 2004. doi: 10.1016/s0017-9310(03)00381-8.

[30] S. Dal Pont and A. Ehrlacher. Numerical and experimental analysis of chemical dehydration, heat and mass transfers in a concrete hollow cylinder submitted to high temperatures. *International Journal of Heat and Mass Transfer*, 47(1):135–147, 2004. doi: 10.1016/S0017-9310(03)00381-8.

[31] S. Dal Pont, S. Durand, and B. Schrefler. A multiphase thermo-hydro-mechanical model for concrete at high temperatures — finite element implementation and validation under LOCA load. *Nuclear Engineering and Design*, 237(22):2137–2150, 2007. doi: 10.1016/j.nucengdes.2007.03.047.

[32] S. Dal Pont, F. Meftah, and B. Schrefler. Modeling concrete under severe conditions as a multiphase material. *Nuclear Engineering and Design*, 241:562–572, 2011. doi: 10.1016/j.nucengdes.2010.04.015.

[33] D. Dauti, A. Tengattini, S. Dal Pont, N. Toropovs, M. Briffaut, and B. Weber. Analysis of moisture migration in concrete at high temperature through in-situ neutron tomography. *Cement and Concrete Research*, 111:41–55, 2018. doi: 10.1016/j.cemconres.2018.06.010.

[34] C. T. Davie, C. J. Pearce, and N. Bičanić. Coupled heat and moisture transport in concrete at elevated temperatures, effects of capillary pressure and adsorbed water. *Numerical Heat Transfer, Part A: Applications*, 49(8):733–763, 2006. doi: 10.1080/10407780500503854.

[35] R. de Boer. *Theory of Porous Media*. Springer, Berlin, 2000. doi: 10.1007/978-3-642-59637-7.

[36] R. de Boer and W. Ehlers. Theorie der Mehrkomponentenkontinua mit Anwendung auf bodenmechanische Probleme. Teil I. Technical report, Universität-GH Essen, Forschungsberichte Bauwesen, Heft 40, 1986.

[37] R. K. Dhir and T. D. Dyer. *Modern Concrete Materials: Binders, Additions and Admixtures*. Thomas Telford Publishing, London, 1999. ISBN 9780727728227. doi: 10.1680/mcm.25944.

[38] S. Diebels. Spannungs-Verformungsverhalten granularer Materialien am Beispiel von Berliner Sand. Bericht Nr. II-6, Universität Stuttgart, Institut für Mechanik, Lehrstuhl II, 2000.

[39] W. Ehlers. Poröse Medien: Ein kontinuumsmechanisches Modell auf der Basis der Mischungstheorie. Technical report, Universität Essen, Forschungsbericht Bauwesen, Heft 47, 1989.

[40] W. Ehlers. Toward finite theories of liquid-saturated elasto-plastic porous media. *International Journal of Plasticity*, 7(5):433–475, 1991. doi: 10.1016/0749-6419(91)90013-O.

[41] W. Ehlers. Compressible, incompressible and hybrid two-phase models in porous theories. 158:25–38, 1993. Proceedings of the ASME Winter Annual Meeting, New Orleans, Louisiana, USA.

[42] W. Ehlers. Constitutive equations for granular materials in geomechanical context. In Kolumban Hutter, editor, *Continuum Mechanics in Environmental Sciences and Geophysics*, pages 313–402. Springer, Vienna, 1993. doi: 10.1007/978-3-7091-2600-4_4.

[43] W. Ehlers. Grundlegende Konzepte in der Theorie poröser Medien. *Technische Mechanik*, 16(1):63–76, 1996. doi: 10.24352/UB.OVGU-2017-064.

[44] W. Ehlers. Foundations of multiphasic and porous materials. In W. Ehlers and J. Bluhm, editors, *Porous Media: Theory, Experiments and Numerical Applications*, pages 3–86. Springer Berlin Heidelberg, Berlin, Heidelberg, 2002. ISBN 978-3-662-04999-0. doi: 10.1007/978-3-662-04999-0_1.

[45] W. Ehlers and C. Andersson. Sorption mechanisms in cement paste and its influence on concrete durability. *Cement and Concrete Research*, 32(8):1239–1250, 2002. doi: 10.1016/S0008-8846(02)00736-6.

[46] W. Ehlers and O. Avci. Stress-dependent hardening and failure surfaces of dry sand. *International Journal for Numerical and Analytical Methods in Geomechanics*, 37 (8):787–809, 2013. doi: 10.1002/nag.1112.

[47] W. Ehlers and Joachim Bluhm, editors. *Porous Media: Theory, Experiments and Numerical Applications*. Springer Science & Business Media, Berlin, 2002. doi: 10.1007/978-3-662-04999-0.

[48] W. Ehlers and B. Markert. On the viscoelastic behaviour of fluid-saturated porous materials. *Granular Matter*, 2(3):153–161, 2000. doi: 10.1007/s100350000030.

[49] W. Ehlers and B. Markert. A linear viscoelastic biphasic model for soft tissues based on the theory of porous media. *Journal of Biomechanical Engineering*, 123 (5):418–424, 2001. doi: 10.1115/1.1392316.

[50] W. Ehlers, P. Ellsiepen, P. Blome, D. Mahnkopf, and B. Markert. Theoretische und numerische Studien zur Lösung von Rand- und Anfangswertproblemen in der Theorie poröser Medien. *Abschlußbericht zum DFG-Forschungsvorhaben Eh*, 107: 6–2, 1999.

[51] W. Ehlers, T. Graf, and M. Ammann. Deformation and localization analysis of partially saturated soil. *Computer Methods in Applied Mechanics and Engineering*, 193(27-29):2885–2910, 2004. doi: 10.1016/j.cma.2004.01.028.

[52] W. Ehlers, O. Avci, and B. Markert. Computation of slope movements initiated by rain-induced shear bands in small-scale tests and in situ. *Vadose Zone Journal*, 10 (2):512–525, 2011. doi: 10.2136/vzj2010.0074.

[53] A. Cemal Eringen. Linear theory of micropolar elasticity. *Journal of Mathematics and Mechanics*, 15(6):909–923, 1966.

[54] C. Ferraris, F. de Larrard, and N. Martys. Fresh concrete rheology: Recent developments. In S. Mindess, editor, *Materials Science of Concrete VI*, pages 215–241. American Ceramic Society, 2001.

[55] C. F. Ferraris, P. Billberg, R. Ferron, D. Feys, J. Hu, S. Kawashima, E. Koehler, M. Sonebi, J. Tanesi, and N. Tregger. Role of rheology in achieving successful concrete performance. *Concrete International*, 39(6):43–51, 2017.

[56] K. G. Fey, I. Riehl, R. Wulf, and U. Gross. Experimental and numerical investigation of the first heat-up of refractory concrete. *International Journal of Thermal Sciences*, 100:108–125, 2016. doi: 10.1016/j.ijthermalsci.2015.10.013.

[57] D. Furbish. Fluid physics in geology: An introduction to fluid motions on Earth's surface and within its crust. *Choice Reviews Online*, 34:34–3873–34–3873, 1997. doi: 10.5860/choice.34-3873.

[58] H. Garbalińska, M. Bochenek, Malorny, W., and J. von Werder. Comparative analysis of the dynamic vapor sorption (dvs) technique and the traditional method for sorption isotherms determination. *Cement and Concrete Research*, 91:97–105, 2017.

[59] D. Gawin, B. Schrefler, and M. Galindo. Thermo-hydro-mechanical analysis of partially saturated porous materials. *Engineering Computations*, 13(7):113–143, 1996. doi: 10.1108/02644409610151584.

[60] D. Gawin, C. Majorana, and B. Schrefler. Numerical analysis of hygro-thermal behaviour and damage of concrete at high temperature. *Mechanics of Cohesive-Frictional Materials*, 4(1):37–74, 1999. doi: 10.1002/(SICI)1099-1484(199901)4:1<37::AID-CFM8>3.0.CO;2-J.

[61] D. Gawin, F. Pesavento, and B. Schrefler. Simulation of damage–permeability coupling in hygro-thermo-mechanical analysis of concrete at high temperature. *Communications in Numerical Methods in Engineering*, 18(2):113–119, 2002. doi: 10.1002/cnm.472.

[62] D. Gawin, F. Pesavento, and B. A. Schrefler. Modelling of hygro-thermal behaviour and damage of concrete at temperature above the critical point of water. *International Journal for Numerical and Analytical Methods in Geomechanics*, 26(6): 537–562, 2002. doi: 10.1002/nag.211.

[63] D. Gawin, F. Pesavento, and B. A. Schrefler. Modelling of hygro-thermal behaviour of concrete at high temperature with thermo-chemical and mechanical material degradation. *Computer Methods in Applied Mechanics and Engineering*, 192 (13-14):1731–1771, 2003. doi: 10.1016/S0045-7825(03)00200-7.

[64] D. Gawin, F. Pesavento, and B. Schrefler. Hygro-thermo-chemo-mechanical modelling of concrete at early ages and beyond. Part I: Hydration and hygro-thermal phenomena. *International Journal for Numerical Methods in Engineering*, 67:299–331, 2006. doi: 10.1002/nme.1615.

[65] D. Gawin, F. Pesavento, and B. Schrefler. Hygro-thermo-chemo-mechanical modelling of concrete at early ages and beyond. Part II: Shrinkage and creep of concrete. *International Journal for Numerical Methods in Engineering*, 67:332–363, 2006. doi: 10.1002/nme.1636.

[66] D. Gawin, F. Pesavento, and B. A. Schrefler. What physical phenomena can be neglected when modelling concrete at high temperature? A comparative study. Part 1: Physical phenomena and mathematical model. *International Journal of Solids and Structures*, 48(13):1927–1944, 2011. doi: 10.1016/j.ijsolstr.2011.03.004.

[67] D. Gawin, M. Koniorczyk, and F. Pesavento. Modelling of hydro-thermo-chemo-mechanical phenomena in building materials. *Bulletin of the Polish Academy of Sciences: Technical Sciences*, 61(1):51–63, 2013. doi: 10.2478/bpasts-2013-0004.

[68] S. R. Ghadiani. A multiphasic continuum mechanical model for design investigations of an effusion-cooled rocket thrust chamber. Bericht, Universität Stuttgart, Institut für Mechanik, 2005.

[69] W. Graf. Modeling and simulation of multiphase flow in porous media: Constitutive modeling and numerical treatment. Bericht, Universität Stuttgart, Institut für Mechanik, Lehrstuhl II, 2008.

[70] P. Grassl and M. Jirásek. Damage-plastic model for concrete failure. *International journal of solids and structures*, 43(22-23):7166–7196, 2006. doi: 10.1016/j.ijsolstr.2006.01.017.

[71] W. G. Gray. Macroscale equilibrium conditions for two-phase flow in porous media. *International Journal of Multiphase Flow*, 26(3):467–501, 2000. doi: 10.1016/S0301-9322(99)00021-X.

[72] W. G. Gray and B. A. Schrefler. Thermodynamic approach to effective stress in partially saturated porous media. *European Journal of Mechanics - A/Solids*, 20(4):521–538, 2001. doi: 10.1016/S0997-7538(01)01158-5.

[73] I. Gupta. *Modelling growth and formation of thrombus: A multiphasic approach*. Verlag der Technischen Universität Graz, 2023.

[74] P. Halamickova, R. J. Detwiler, D. P. Bentz, and E. J. Garboczi. Water permeability and chloride ion diffusion in portland cement mortars: Relationship to sand content and critical pore diameter. *Cement and Concrete Research*, 25(4):790–802, 1995. doi: 10.1016/0008-8846(95)00069-O.

[75] T. Z. Harmathy. Simultaneous moisture and heat transfer in porous systems with particular reference to drying. *Industrial & Engineering Chemistry Fundamentals*, 8(1):92–103, 1969. doi: 10.1021/i160029a016.

[76] M. Hassanizadeh and W. G. Gray. General conservation equations for multi-phase systems: 1. Averaging procedure. *Advances in Water Resources*, 2:131–144, 1979. doi: 10.1016/0309-1708(79)90025-3.

[77] P. Haupt. Foundation of continuum mechanics. In Kolumban Hutter, editor, *Continuum Mechanics in Environmental Sciences and Geophysics*, pages 1–77. Springer, Vienna, 1993. ISBN 978-3-211-82449-8. doi: 10.1007/978-3-7091-2600-4_1.

[78] G. Heinrich and K. Desoyer. Hydromechanische Grundlagen für die Behandlung von stationären und instationären Grundwasserströmungen. *Ingenieur-Archiv*, 23 (2):73–84, 1955. doi: 10.1007/BF00536733.

[79] C. Hill, A. J. Norton, and G. Newman. The water vapour sorption properties of sitka spruce determined using a dynamic vapour sorption apparatus. *Wood Science and Technology*, 44:497–514, 2010.

[80] A. Hillerborg, M. Modéer, and P. E. Petersson. Analysis of crack formation and crack growth in concrete by means of fracture mechanics and finite elements. *Cement and Concrete Research*, 6(6):773–781, 1976. doi: 10.1016/0008-8846(76)90007-7.

[81] G. A. Holzapfel. Nonlinear solid mechanics: A continuum approach for engineering science. *Meccanica*, 37(4):489–490, 2002. doi: 10.1023/A:1020843529530.

[82] J. Hu and K. Wang. Effect of coarse aggregate characteristics on concrete rheology. *Construction and Building Materials*, 25(3):1196–1204, 2011. doi: 10.1016/j.conbuildmat.2010.09.018.

[83] T. J. R. Hughes. *The Finite Element Method: Linear Static and Dynamic Finite Element Analysis*. Dover Publications, Mineola, NY, 2003. ISBN 978-0486411811.

[84] N. Issaadi, A. Nouviaire, R. Belarbi, and A. Ait-Mokhtar. Moisture characterization of cementitious material properties: Assessment of water vapor sorption isotherm and permeability variation with ages. *Construction and Building Materials*, 83:237–247, 2015.

[85] A. Jędrzejewska, F. Benboudjema, L. Lacarriere, M. Azenha, D. Schlicke, S. Dal Pont, A. Delaplace, J. Granja, K. Hajkova, P. J. Heinrich, et al. COST TU1404 Benchmark on macroscopic modelling of concrete and concrete structures at early age: Proof-of-concept stage. *Construction and Building Materials*, 174:173–189, 2018. doi: 10.1016/j.conbuildmat.2018.04.088.

[86] B. F. Johannesson. Prestudy on diffusion and transient condensation of water vapor in cement mortar. *Cement and Concrete Research*, 32(5):731–736, 2002.

[87] D. K. Kondepudi and I. Prigogine. *Modern Thermodynamics: From Heat Engines to Dissipative Structures*. John Wiley & Sons, Chichester, UK, 2nd edition, 2014. ISBN 978-1-118-69869-3. doi: 10.1002/9781118698723.

[88] Markus Königsberger, Michal Hlobil, Brice Delsaute, Stéphanie Staquet, Christian Hellmich, and Bernhard Pichler. Hydrate failure in ITZ governs concrete strength: A micro-to-macro validated engineering mechanics model. *Cement and Concrete Research*, 103:77–94, 2018. doi: 10.1016/j.cemconres.2017.10.002.

[89] S. H. Kosmatka, W. C. Panarese, and B. Kerkhoff. *Design and Control of Concrete Mixtures*. Portland Cement Association, Skokie, IL, 14th edition, 2002. ISBN 978-0-89312-217-4.

[90] P. Lade and R. de Boer. The concept of effective stress for soil, concrete and rock. *Géotechnique*, 47(1):61–78, 1997. doi: 10.1680/geot.1997.47.1.61.

[91] H. P. Langtangen and A. Tveito. *Advanced Topics in Computational Partial Differential Equations: Numerical Methods and Diffpack Programming*, volume 33. Springer Science & Business Media, Berlin, Heidelberg, 2012. ISBN 978-3642566489.

[92] R. W. Lewis and B. A. Schrefler. *The Finite Element Method in the Static and Dynamic Deformation and Consolidation of Porous Media*. John Wiley & Sons, New York, 2 edition, 2000.

[93] K. Li and Z. Wang. Characterizing pore structure of cement blend pastes using water vapor sorption analysis. *Materials Characterization*, 95:72–84, 2014. doi: 10.1016/j.matchar.2014.06.010.

[94] M. Liang, Z. Chang, H. Y. Shan, Y. G. Chen, E. Schlangen, and B. Šavija. Predicting early-age stress evolution in restrained concrete by thermo-chemo-mechanical model and active ensemble learning. *Computer-Aided Civil and Infrastructure Engineering*, 37(14):1809–1833, 2022. doi: 10.1111/mice.12915.

[95] O. Linderoth, P. Johansson, and L. Wadsö. Development of pore structure, moisture sorption and transport properties in fly ash blended cement-based materials. *Construction and Building Materials*, 261:120007, 2020. doi: 10.1016/j.conbuildmat.2020.120007.

[96] Z. Liu and D. Winslow. Sub-distributions of pore size: A new approach to correlate pore structure with permeability. *Cement and Concrete Research*, 25(4):769–778, 1995. doi: 10.1016/0008-8846(95)00067-M.

[97] J. Lubliner, J. Oliver, S. Oller, and E. Onate. A plastic-damage model for concrete. *International Journal of solids and structures*, 25(3):299–326, 1989. doi: 10.1016/0020-7683(89)90050-4.

[98] M. Mainguy, O. Coussy, and V. Baroghel-Bouny. Role of air pressure in drying of weakly permeable materials. *Journal of Engineering Mechanics*, 127(6):582–592, 2001. doi: 10.1061/(ASCE)0733-9399(2001)127:6(582).

[99] L. J. Malvar, J. E. Crawford, J. W. Wesevich, and D. Simons. A plasticity concrete material model for DYNA3D. *International Journal of Impact Engineering*, 19(9–10):847–873, 1997. doi: 10.1016/S0734-743X(97)00023-7.

[100] R. Mandal, S. K. Panda, and S. Nayak. Rheology of concrete: Critical review, recent advancements, and future prospectives. *Construction and Building Materials*, 392:132007, 2023. doi: 10.1016/j.conbuildmat.2023.132007.

[101] B. Markert. Weak or strong: On coupled problems in continuum mechanics. Bericht Nr. II-20, Universität Stuttgart, Institut für Mechanik, Lehrstuhl II, 2010.

[102] G. C. Mays. *Durability of Concrete Structures: Investigation, Repair, Protection*. CRC Press, London, 1991. doi: 10.4324/9780203473474.

[103] P. K. Mehta and P. J. M. Monteiro. *Concrete: Microstructure, Properties, and Materials*. McGraw-Hill Education, New York, 2014. ISBN 9780071797870. doi: 10.1036/0071797875.

[104] L. Miao, M. Wen, C. Jiao, S. He, and X. Guan. Study on desorption characteristics of water vapor in fly ash concrete materials. *Case Studies in Construction Materials*, 20:e03103, 2024. doi: 10.1016/j.cscm.2023.e03103.

[105] R. H. Mills. Factors influencing cessation of hydration in water cured cement pastes. *Highway Research Board Special Report*, (90), 1966.

[106] M. Muskat and M. W. Meres. The flow of heterogeneous fluids through porous media. *Journal of Applied Physics*, 7(9):346–363, 1936. doi: 10.1063/1.1745403.

[107] J. Nocedal and S. J. Wright. *Numerical Optimization*. Springer, New York, 1999. ISBN 978-0-387-98793-4. doi: 10.1007/b98874.

[108] W. Noll. On the continuity of the solid and fluid states. *Indiana University Mathematics Journal*, 4(1):3–81, 1955. doi: 10.1512/iumj.1955.4.54001.

[109] W. Noll. A mathematical theory of the mechanical behavior of continuous media. *Archive for Rational Mechanics and Analysis*, 2(1):197–226, 1958. doi: 10.1007/BF00277929.

[110] F. Pesavento. Nonlinear modelling of concrete as a multiphase material in high temperature conditions. Bericht, Università degli Studi di Padova, 2000.

[111] B. Pichler, C. Hellmich, J. Eberhardsteiner, J. Wasserbauer, P. Termkhajornkit, R. Barbarulo, and G. Chanvillard. Effect of gel–space ratio and microstructure on strength of hydrating cementitious materials: An engineering micromechanics approach. *Cement and Concrete Research*, 45:55–68, 2013. doi: 10.1016/j.cemconres.2012.10.019.

[112] C. Pohl. Numerical modelling of moisture transport in concrete under high temperatures. Phd thesis, Czech Technical University, 2022.

[113] C. Pohl, V. Šmilauer, and J. F. Unger. A three-phase transport model for high-temperature concrete simulations validated with X-Ray CT data. *Materials*, 14(17):5047, 2021.

[114] T. C. Powers and T. L. Brownyard. Studies of the physical properties of hardened portland cement paste. *Bulletin 22, Research Laboratory, Portland Cement Association*, 43(9):101–132, 1946. doi: 10.14359/15301.

[115] T. C. Powers and T. L. Brownyard. Studies of the physical properties of hardened Portland cement paste. *Journal Proceedings*, 43(9):549–602, 1947.

[116] Zeng Q. and S. Xu. A two-parameter stretched exponential function for dynamic water vapor sorption of cement-based porous materials. *Materials and Structures*, 50:1–13, 2017.

[117] E. Reyhanian, B. Dorschner, and I. V. Karlin. Thermokinetic model of compressible multiphase flows. *arXiv preprint:2002.09217*, 2020. doi: 10.48550/arXiv.2002.09217.

[118] T. Ricken and J. Bluhm. Remodeling and growth of living tissue: A multiphase theory. *Archive of Applied Mechanics 2009 80:5*, 80:453–465, 11 . ISSN 1432-0681. doi: 10.1007/S00419-009-0383-1.

[119] N. Roussel. Rheology of fresh concrete: From measurements to predictions of casting processes. *Materials and Structures*, 40(10):1001–1012, 2007. doi: 10.1617/s11527-007-9313-2.

[120] M. Saeidpour and L. Wadsö. Evidence for anomalous water vapor sorption kinetics in cement-based materials. *Cement and Concrete Research*, 70:60–66, 2015.

[121] A. E. Scheidegger. *The Physics of Flow Through Porous Media*. University of Toronto Press, Toronto, 1957. doi: 10.3138/9781487583750.

[122] M. Schenke. Parallel simulation of volume-coupled multi-field problems with special application to soil dynamics. Bericht Nr. II-32, Universität Stuttgart, Institut für Mechanik, Lehrstuhl II, 2017.

[123] U. Schneider and H. J. Herbst. Permeabilität und Porosität von Beton bei hohen Temperaturen. *Deutscher Ausschuß für Stahlbeton (DAfStb) Heft 403*, pages 23–52, 1989.

[124] B. A. Schrefler. Computer modelling in environmental geomechanics. *Computers and Structures*, 79(22-25):2209–2223, 2001. doi: 10.1016/S0045-7949(01)00104-2.

[125] B. A. Schrefler. Mechanics and thermodynamics of saturated/unsaturated porous materials and quantitative solutions. *Applied Mechanics Reviews*, 55(4):351–388, 2002. doi: 10.1115/1.1484107.

[126] B. A. Schrefler and D. Gawin. The effective stress principle: Incremental or finite form? *International Journal for Numerical and Analytical Methods in Geomechanics*, 20(11):785–814, 1996. doi: 10.1002/(SICI)1096-9853(199611)20:11<785::AID-NAG846>3.0.CO;2-6.

[127] B. A. Schrefler and R. Scotta. A fully coupled model for two-phase flow in deformable porous media. *Computer Methods in Applied Mechanics and Engineering*, 190(28):3223–3246, 2001. doi: 10.1016/S0045-7825(00)00334-4.

[128] B. A. Schrefler, L. Sanavia, and C. Majorana. A multiphase media model for localization and post-localization simulation in geomaterials. *Mechanics of Cohesive-frictional Materials*, 1(1):95–114, 1996. doi: 10.1002/(SICI)1099-1484(199601)1:1<95::AID-CFM8>3.0.CO;2-7.

[129] SciPy Developers. Scipy optimization documentation, 2024. Accessed: 2024-06-01.

[130] G. Sciumè, M. H. Moreira, and S. Dal Pont. Thermo-hygro-chemical model of concrete: From curing to high temperature behavior. *Materials and Structures*, 57 (8):186, 2024. doi: 10.1617/s11527-024-02454-3.

[131] S. P. Shah, S. E. Swartz, and C. Ouyang. *Fracture Mechanics of Concrete: Applications of Fracture Mechanics to Concrete, Rock and Other Quasi-Brittle Materials*. John Wiley & Sons, New York, 1995.

[132] D. Snoeck, L. F. Velasco, A. Mignon, S. van Vlierberghe, P. Dubruel, P. Lodewyckx, and N. de Belie. The influence of different drying techniques on the water sorption properties of cement-based materials. *Cement and Concrete Research*, 64:54–62, 2014.

[133] A. H. Stroud. Approximate calculation of multiple integrals. prentice-hall series in automatic computation. *Prentice-Hall series in automatic computation*, 1, 1971.

[134] A. Tarantola. *Inverse Problem Theory and Methods for Model Parameter Estimation*. SIAM, Philadelphia, PA, 2005. ISBN 978-0-89871-572-9. doi: 10.1137/1.9780898717921.

[135] C. Taylor and P. Hood. A numerical solution of the Navier-Stokes equations using the finite element technique. *Computers & Fluids*, 1(1):73–100, 1973. doi: 10.1016/0045-7930(73)90027-3.

[136] H. R. Thomas and M. R. Sansom. *Fully Coupled Analysis of Heat, Moisture, and Air Transfer in Unsaturated Soil*. University of Wales, Cardiff (Report), Cardiff, UK, 1995. Research Report.

[137] C. Truesdell. A new definition of a fluid. Technical Report I, Naval Research Laboratory, 1949.

[138] C. Truesdell. Historical introit: The origins of rational thermodynamics. In *Rational Thermodynamics (2nd Ed.)*, pages 1–48. Springer, New York, NY, 1984. doi: 10.1007/978-1-4612-5206-1_1.

[139] F. Ulm and O. Coussy. Modeling of thermo-chemo-mechanical couplings of concrete at early ages. *Journal of Engineering Mechanics*, 121(7):785–794, 1995. doi: 10.1061/(ASCE)0733-9399(1995)121:7(785).

[140] F. Ulm and O. Coussy. Strength growth as chemo-plastic hardening in early age concrete. *Journal of Engineering Mechanics*, 122(12):1123–1132, 1996. doi: 10.1061/(ASCE)0733-9399(1996)122:12(1123).

[141] M. van Genuchten. A closed-form equation for predicting the hydraulic conductivity of unsaturated soils. *Soil Science Society of America Journal*, 44(5):892–898, 1980. doi: 10.2136/sssaj1980.03615995004400050002x.

[142] D. E. A. van Odyck, J. B. Bell, F. Monmont, and N. Nikiforakis. The mathematical structure of multiphase thermal models of flow in porous media. *Proceedings of the Royal Society A: Mathematical, Physical and Engineering Sciences*, 465(2102): 523–549, 2008. doi: 10.1098/rspa.2008.0268.

[143] L. Wadsö and M. Saeidpour. Moisture equilibrium of cement based materials containing slag or silica fume and exposed to repeated sorption cycles. *Cement and Concrete Research*, 69:88–95, 2015.

[144] Z. Wang and K. Li. Understanding water vapor sorption hysteresis and scanning behaviors of hardened cement pastes: Experiments and modeling. *Cement and Concrete Research*, 177:107435, 2024. doi: 10.1016/j.cemconres.2024.107435.

[145] M. Wu, B. Johannesson, and M. Geiker. A study of the water vapor sorption isotherms of hardened cement pastes: Possible pore structure changes at low relative humidity and the impact of temperature on isotherms. *Cement and Concrete Research*, 56:97–105, 2014. doi: 10.1016/j.cemconres.2013.11.008.

[146] A. Yahia, S. Mantellato, and R. J. Flatt. Concrete rheology: A basis for understanding chemical admixtures. In Pierre-Claude Aïtcin and Robert J. Flatt, editors, *Science and Technology of Concrete Admixtures*, pages 97–127. Woodhead Publishing, Cambridge, UK, 2016. doi: 10.1016/B978-0-08-100693-1.00007-2.

[147] W. You, F. Zhang, Y. Huang, M. Gao, C. Wen, and G. Yang. A coupled hygro-thermo-mechanical model for the evolution of saturation in early-age concrete. *International Journal of Heat and Mass Transfer*, 156:119817, 2020. doi: 10.1016/j.ijheatmasstransfer.2020.119817.

[148] W. You, X. Liu, H. Shang, and G. Yang. Evolution of temperature, humidity and deformation in early-age cement-based materials based on a multi-field model. *Construction and Building Materials*, 290:123277, 2021. doi: 10.1016/j.conbuildmat.2021.123277.

[149] O. C. Zienkiewicz and R. L. Taylor. *The Finite Element Method for Solid and Structural Mechanics*. Elsevier Butterworth-Heinemann, Oxford, UK, 6 edition, 2005. ISBN 9780750663212. doi: 10.1016/B978-0-08-045558-7.X5000-3.

Monographic Series TU Graz
Computation in Engineering and Science

Vol. 1 Steffen Alvermann
Effective Viscoelastic Behavior of Cellular Auxetic Materials
2008
ISBN 978-3-902465-92-4

Vol. 2 Sendy Fransiscus Tantono
The Mechanical Behaviour of a Soilbag under Vertical Compression
2008
ISBN 978-3-902465-97-9

Vol. 3 Thomas Rüberg
Non-conforming FEM/BEM Coupling in Time Domain
2008
ISBN 978-3-902465-98-6

Vol. 4 Dimitrios E. Kiousis
Biomechanical and Computational Modeling of Atherosclerotic Arteries
2008
ISBN 978-3-85125-023-7

Vol. 5 Lars Kielhorn
A Time-Domain Symmetric Galerkin BEM for Viscoelastodynamics
2009
ISBN 978-3-85125-042-8

Monographic Series TU Graz
Computation in Engineering and Science

Vol. 6 Gerhard Unger
Analysis of Boundary Element Methods for Laplacian Eigenvalue Problems
2009
ISBN 978-3-85125-081-7

Vol. 7 Gerhard Sommer
Mechanical Properties of Healthy and Diseased Human Arteries
2010
ISBN 978-3-85125-111-1

Vol. 8 Mathias Nenning
Infinite Elements for Elasto- and Poroelastodynamics
2010
ISBN 978-3-85125-130-2

Vol. 9 Thanh Xuan Phan
Boundary Element Methods for Boundary Control Problems
2011
ISBN 978-3-85125-149-4

Vol. 10 Loris Nagler
Simulation of Sound Transmission through Poroelastic Plate-like Structures
2011
ISBN 978-3-85125-153-1

Monographic Series TU Graz
Computation in Engineering and Science

Vol. 11 Markus Windisch
Boundary Element Tearing and Interconnecting Methods for Acoustic and Electromagnetic Scattering
2011
ISBN 978-3-85125-152-4

Vol. 12 Christian Walchshofer
Analysis of the Dynamics at the Base of a Lifted Strongly Buoyant Jet Flame Using Direct Numerical Simulation
2011
ISBN 978-3-85125-185-2

Vol. 13 Matthias Messner
Fast Boundary Element Methods in Acoustics
2012
ISBN 978-3-85125-202-6

Vol. 14 Peter Urthaler
Analysis of Boundary Element Methods for Wave Propagation in Porous Media
2012
ISBN 978-3-85125-216-3

Vol. 15 Peng Li
Boundary Element Method for Wave Propagation in Partially Saturated Poroelastic Continua
2012
ISBN 978-3-85125-236-1

Monographic Series TU Graz
Computation in Engineering and Science

Vol. 16 Andreas Jörg Schriefl
Quantification of Collagen Fiber Morphologies in Human Arterial Walls
2013
ISBN 978-3-85125-238-5

Vol. 17 Thomas S. E. Eriksson
Cardiovascular Mechanics
2013
ISBN 978-3-85125-277-4

Vol. 18 Jianhua Tong
Biomechanics of Abdominal Aortic Aneurysms
2013
ISBN 978-3-85125-279-8

Vol. 19 Jonathan Rohleder
Titchmarsh–Weyl Theory and Inverse Problems for Elliptic Differential Operators
2013
ISBN 978-3-85125-283-5

Vol. 20 Martin Neumüller
Space-Time Methods
2013
ISBN 978-3-85125-290-3

Monographic Series TU Graz
Computation in Engineering and Science

Vol. 21 Michael J. Unterberger
Microstructurally-Motivated Constitutive Modeling of Cross-Linked Filamentous Actin Networks
2013
ISBN 978-3-85125-303-0

Vol. 22 Vladimir Lotoreichik
Singular Values and Trace Formulae for Resolvent Power Differences of Self-Adjoint Elliptic Operators
2013
ISBN 978-3-85125-304-7

Vol. 23 Michael Meßner
A Fast Multipole Galerkin Boundary Element Method for the Transient Heat Equation
2014
ISBN 978-3-85125-350-4

Vol. 24 Lorenz Johannes John
Optimal Boundary Control in Energy Spaces
2014
ISBN 978-3-85125-373-3

Vol. 25 Hannah Weisbecker
Softening and Damage Behavior of Human Arteries
2014
ISBN 978-3-85125-370-2

Monographic Series TU Graz
Computation in Engineering and Science

Vol. 26 Bernhard Kager
Efficient Convolution Quadrature based Boundary Element Formulation for Time-Domain Elastodynamics
2015
ISBN 978-3-85125-382-5

Vol. 27 Christoph M. Augustin
Classical and All-floating FETI Methods with Applications to Biomechanical Models
2015
ISBN 978-3-85125-418-1

Vol. 28 Elias Karabelas
Space-Time Discontinuous Galerkin Methods for Cardiac Electromechanics
2016
ISBN 978-3-85125-461-7

Vol. 29 Thomas Traub
A Kernel Interpolation Based Fast Multipole Method for Elastodynamic Problems
2016
ISBN 978-3-85125-465-5

Vol. 30 Matthias Gsell
Mortar Domain Decomposition Methods for Quasilinear Problems and Applications
2017
ISBN 978-3-85125-522-5

Monographic Series TU Graz
Computation in Engineering and Science

Vol. 31 Christian Kühn
Schrödinger operators and singular infinite rank perturbations
2017
ISBN 978-3-85125-551-5

Vol. 32 Michael H. Gfrerer
Vibro-Acoustic Simulation of Poroelastic Shell Structures
2018
ISBN 978-3-85125-573-7

Vol. 33 Markus Holzmann
Spectral Analysis of Transmission and Boundary Value Problems for Dirac Operators
2018
ISBN 978-3-85125-642-0

Vol. 34 Osman Gültekin
Computational Inelasticity of Fibrous Biological Tissues with a Focus on Viscoelasticity, Damage and Rupture
2019
ISBN 978-3-85125-655-0

Vol. 35 Justyna Anna Niestrawska
Experimental and Computational Analyses of Pathological Soft Tissues – Towards a Better Understanding of the Pathogenesis of AAA
2019
ISBN 978-3-85125-678-9

Monographic Series TU Graz
Computation in Engineering and Science

Vol. 36 Marco Zank
Inf-Sup Stable Space-Time Methods for Time-Dependent Partial Differential Equations
2020
ISBN 978-3-85125-721-2

Vol. 37 Christoph Irrenfried
Convective turbulent near wall heat transfer at high Prandtl numbers
2020
ISBN 978-3-85125-724-3

Vol. 38 Christopher Albert
Hamiltonian Theory of Resonant Transport Regimes in Tokamaks with Perturbed Axisymmetry
2020
ISBN 978-3-85125-746-5

Vol. 39 Daniel Christopher Haspinger
Material Modeling and Simulation of Phenomena at the Nano, Micro and Macro Levels in Fibrous Soft Tissues of the Cardiovascular System
2021
ISBN 978-3-85125-802-8

Vol. 40 Markus Alfons Geith
Percutaneous Coronary Intervention
2021
ISBN 978-3-85125-801-1

Monographic Series TU Graz
Computation in Engineering and Science

Vol. 41 Dominik Pölz
Space-Time Boundary Elements for Retarded Potential Integral Equations
2021
ISBN 978-3-85125-811-0

Vol. 42 Douglas Ramalho Queiroz Pacheco
Stable and stabilised finite element methods for incompressible flows of generalised Newtonian fluids
2021
ISBN 978-3-85125-856-1

Vol. 43 Peter Schlosser
Superoscillations and their Schrödinger time evolution
2022
ISBN 978-3-85125-930-8

Vol. 44 Raphael Watschinger
Fast space-time boundary element methods for the heat equation
2023
ISBN 978-3-85125-949-0

Vol. 45 Ishan Gupta
Modelling Growth and Formation of Thrombus: A Multiphasic Approach
2023
ISBN 978-3-85125-964-3

Monographic Series TU Graz
Computation in Engineering and Science

Vol. 46 Mario Gobrial
Space-time Finite Element Methods
for the Eddy Current Problem and Applications
2025
ISBN 978-3-99161-048-9

Vol. 47 Christian Stelzer-Landauer
Approximation of Dirac Operators with
Delta-Shell Potentials in the Norm Resolvent Sense
2025
ISBN 978-3-99161-052-6

Vol. 48 Christian Köthe
Adaptive least-squares
space-time finite element methods
2025
ISBN 978-3-99161-060-1

Vol. 49 Silvio Prskalo
Coupled thermo-hygral and mechanical behavior in
fresh concrete: a multiphase material model approach
2026
ISBN 978-3-99161-067-0

Coupled thermo-hygral and mechanical behavior in fresh concrete: a multiphase material model approach

This thesis presents a multiphase continuum-mechanical model for simulating the early-age behavior of concrete, governed by coupled moisture transport, temperature evolution and mechanical property development. A key innovation is the explicit inclusion of evaporation exchange in the mass balance, enabling direct coupling between evaporation and hydration—an interaction often neglected in porous media models. The evaporation process is calibrated using Dynamic Vapor Sorption (DVS) experiments.

The work also reassesses the commonly assumed linear relation between porosity and hydration degree. Allowing nonlinear dependencies, the model captures more complex interactions arising from varying microstructure and boundary conditions. Building on the framework of Gawin et al. (2006), a multiscale formulation links hydration to the time-dependent evolution of stiffness and strength.

The fully coupled finite element implementation accounts for nonlinear heat, moisture and mechanical interactions. Numerical validation across different concrete mixes shows very good agreement with experiments, confirming the model's accuracy and broad applicability for predicting early-age concrete behavior.

MONOGRAPHIC SERIES TU GRAZ
COMPUTATION IN ENGINEERING AND SCIENCE

Verlag der Technischen Universität Graz
www.tugraz-verlag.at

ISBN 978-3-99161-067-0
ISSN 1990-357X

9 783991 610670